FLUID DYNAMICS IN CHARGE STABILIZED COLLOIDAL SUSPENSIONS

Dirk O. Riese

FLUID DYNAMICS IN CHARGE STABILIZED COLLOIDAL SUSPENSIONS

ACADEMISCH PROEFSCHRIFT

ter verkrijging van de graad van doctor
aan de Universiteit van Amsterdam
op gezag van de Rector Magnificus
prof. dr. J. J. M. Franse
ten overstaan van een door het college voor promoties
ingestelde commissie, in het openbaar te verdedigen
in de Aula der Universiteit
op maandag 4 december 2000, te 12:00 uur

door

Dirk Oliver Riese

geboren te Neustadt an der Weinstrasse, Duitsland

Promotor:	Prof. Dr. A. Lagendijk
Co-Promotor:	Dr. G. H. Wegdam

Commissie:	Prof. Dr. D. Frenkel
	Dr. G. Grübel
	Prof. Dr. Ir. W. H. de Jeu
	Prof. Dr. Ir. W. van Saarloos
	Dr. W. L. Vos

Faculteit der Natuurwetenschappen, Wiskunde en Informatica

The work described in this thesis has been supported by the
"Stichting voor Fundamenteel Onderzoek der Materie (FOM)",
which is financially supported by the
"Nederlandse Organisatie voor Wetenschappelijk Onderzoek (NWO)"
and was carried out at the

Van der Waals-Zeeman Instituut
Universiteit van Amsterdam
Valckenierstraat 65
1018 XE Amsterdam
The Netherlands

"Wir fühlen, dass selbst, wenn alle möglichen
wissenschaftlichen Fragen beantwortet sind,
unsere Lebensprobleme noch gar nicht berührt sind."

Ludwig Wittgenstein;
Tractatus Logico Philosophicus, v. 6.52

Contents

1

Introduction

One of the most fascinating aspects of physics is its ability to describe phenomena on vastly different length scales, from the microscopic world of atomic nuclei (10^{-15} m) to the dynamics of the universe as a whole (10^{26} m). In general, different physical descriptions are associated with these distinct ranges of length scales, since varying facets of nature's behavior become dominant depending on the size of a system. For instance, the quantum mechanical character of matter becomes noticeable only on an atomic length scale, while the intriguing properties of curved space-time manifest themselves on a cosmological level.

According to the extraordinary importance of length scales for the physical behavior of matter, one distinguishes between microscopic, macroscopic and mesoscopic systems. The microscopic world comprises molecules and atoms, whereas the macroscopic world ranges from objects accessible to our every-day experience to cosmological distances. Mesoscopic systems bridge the span between microscopic and macroscopic length scales, and they are thus located in the region where microscopic behavior gradually changes into macroscopic one or vice versa. The scientific interest in mesoscopic phenomena stems from this exceptional role.

A particular kind of mesoscopic systems is the subject of this thesis: colloidal suspensions [1]. Colloidal suspensions are composite systems consisting of a molecular fluid and particles of much larger size that are dispersed in it. The size of the larger, colloidal particles is typically in the range between 1 nm and 1 μm. The lower size limit stems from the requirement that the colloids be significantly larger than the solvent molecules, and the upper limit

ensures that the Brownian motion of the colloidal particles is not dominated by external effects such as sedimentation under gravity. Owing to their mesoscopic character and their complex composition, colloidal suspensions exhibit intriguing static and dynamic properties. There are striking similarities between the static behavior of colloidal dispersions and molecular systems. For instance, they both show phase transitions between liquid and solid phases, and their structural properties may be described basically within the same framework. On the other hand, there are of course many important effects that are unique to colloidal suspensions and that make them a particularly interesting field of study. The interaction potential between colloidal particles, for example, depends strongly on the surface chemistry of the interface between the disperse phase and the dispersion medium and on the properties of the suspending liquid; it can, therefore, be tuned by chemical means. If the interaction potential is attractive, phenomena such as aggregation and clustering occur, giving rise to the development of fractal structures. (It is interesting to note that these processes bear some similarity with phenomena on the other end of the length scale range, e.g. the clustering of galaxies.) Another significant dissimilarity between colloidal suspensions and molecular fluids stems from the important role of the suspending medium. As the colloidal particles diffuse through the liquid, they create a velocity field, giving rise to a hydrodynamic interaction between them.

Apart from their fundamental interest, colloidal suspensions are of great biological and technological importance [2]. For instance, such diverse systems as paint, blood and mayonnaise all belong to the class of colloidal dispersions. As a result, colloids have been the subject of intense research efforts ever since the discovery of the irregular motion of pollen grains in water by Robert Brown in 1828. In the past three decades or so, progress in colloid chemistry has made well-defined model systems available, such as monodisperse silica or latex spheres, leading to an enhanced interest in this field [3]. For technological applications, the macroscopic flow properties of complex fluids are of particular importance, which depend sensitively on the forces acting on the mesoscopic, colloidal level. The availability of model systems has made the detailed study of these interactions possible.

In this thesis, we will be concerned with dynamical phenomena associated with the suspending liquid, and with their coupling to the static properties of the suspensions.

1.1 Silica suspensions

As a model system, we will use suspensions of colloidal silicon dioxide (silica) spheres. Spherical colloidal silica particles can be prepared with low polydispersity, with typical relative size variations below 5 % [4]. If dispersed in a polar liquid, silica colloids acquire a surface charge due to the dissociation of surface groups. The resulting electrostatic repulsion between the particles is screened by counterions and excess salt in the suspending liquid. If the salt concentration is low enough, the screened Coulomb interaction stabilizes the suspension against aggregation. We use silica particles here for three reasons. First, they are charge stabilized and thus allow to manipulate the direct interaction between the particles by controlling the salt content of the suspending fluid. Secondly, their refractive index is relatively low (around 1.45) and it is thus possible to match the refractive index of the suspending fluid to that of the particles, if desired. Thirdly, their density and sound velocity differs substantially from that of molecular fluids, such that silica suspensions are acoustically strongly inhomogeneous on the length scale of the particle radius; this point will be important in chapter 5.

1.2 Dynamic light- and x-ray scattering

Dynamic light scattering (DLS) is the most important experimental technique with which to study the dynamics of colloidal suspensions. It relies on the fact that if coherent radiation impinges on a colloidal fluid, the scattered intensity in the far field exhibits a fluctuating interference pattern. DLS measures the time dependent intensity correlation function at a given spatial position, which reflects the dynamics of the system. From the temporal decay of the intensity correlation function, the collective diffusion coefficient of the colloids can be obtained. However, this is only true as long as the light is not multiply scattered within the sample, which restricts the applicability of DLS to either index matched or very dilute systems [5]. As a consequence of these limitations, experimental results on the dynamics of charge stabilized colloids at high colloid concentrations are very scarce. At high volume fractions of colloids multiple scattering of light becomes important, requiring the refractive index of the suspending fluid to be matched to that of the particles. Index matching is, however, a rather unsatisfactory option, for several reasons. First, the direct electrostatic interaction between the particles depends

on the properties of the suspending fluid. In order to manipulate the direct interaction one would, therefore, like to be able to select the fluid freely, without being restricted by the requirement of index matching. Secondly, in a DLS setup light does not only scatter from the colloidal particles, but unfortunately also from sample cells, pinholes, lenses etc.. As a result, the desired signal inevitably competes with all sorts of stray light; index matching of the suspending fluid to the colloids, thereby reducing the signal, seems rather disadvantageous under these circumstances. Thirdly, for many systems index matching is simply not possible, such as for instance suspensions of polystyrene latex spheres (refractive index ≈ 1.6). For these reasons, we investigate in chapter 3 the potential and reliability of two new experimental techniques that are free from multiple scattering: dynamic x-ray scattering (DXS) and cross-correlated dynamic light scattering with a single laser beam (CCDLS). In recent years, advances in the technical development of third-generation synchrotron sources have made it possible to measure intensity correlation functions with coherent x rays instead of visible light [6]. For x rays, multiple scattering is absent. We will first examine the ability of DXS to probe the dynamics of dense colloidal suspensions. Then, we will use dynamic x-ray scattering as a reference to assess the performance of CCDLS. Combining these techniques with small-angle x-ray scattering provides us with a powerful tool for obtaining both static and dynamic information on optically opaque samples.

1.3 Hydrodynamic interactions

Apart from the direct interactions between the colloidal particles, the presence of the suspending medium leads to a hydrodynamic interaction [3]. A diffusing particle will create a velocity field in the fluid due to the coupling of the fluid velocity and the velocity of the colloids at the particle surface. In other words, the fluid velocity field has to satisfy the hydrodynamic equations subject to the appropriate boundary conditions at the surface of the colloidal spheres. The resulting hydrodynamic coupling of the colloidal particles plays an important role in e.g. sedimentation [7], aggregation and gel formation [8]. In hard-sphere suspensions, the hydrodynamic interaction between the particles slows down their diffusional motion, that is, it acts as an additional friction. However, in recent years it has been recognized that the behavior of the hydrodynamic interaction in charged suspensions can be quite different:

in highly charged suspensions at low colloid concentrations, the hydrodynamic interaction may even enhance diffusion [9]. Thus, there is a subtle interplay between direct and hydrodynamic interactions. An open question is how this interplay influences the dynamics of charged, strongly interacting particles at high densities; this regime is most difficult to access theoretically as well as experimentally. The experimental difficulties have been discussed above. It is the aim of this thesis to overcome the experimental obstacles and provide reliable experimental data on dense, charge stabilized suspensions. Using the new techniques introduced in chapter 3, we are able to study the coupling of direct and hydrodynamic interactions in detail. We find that if the direct interaction is strong and long-ranged, the effective hydrodynamic interaction in concentrated suspensions exhibits an apparent hydrodynamic screening, phenomenologically similar to e.g. porous media or polyelectrolyte solutions. These experiments are reported in chapter 4.

1.4 Waves in complex media

The hydrodynamic interaction between colloidal particles may be viewed as an instance of the phenomenon of wave propagation in complex media: a diffusing colloidal particle excites a hydrodynamic disturbance in the suspending fluid which is multiply scattered by the other particles. Consequently, the hydrodynamic velocity field in a colloidal suspension may be described as arising from a series of scattering events. The propagation and scattering of classical waves in complex media has received much attention in recent years. For instance, strongly scattering colloidal suspensions [10] and macroporous sponges [11] are studied in the context of light localization and photonic band gaps. In a related development, the propagation of acoustic waves in inhomogeneous media is studied [12]. In a colloidal suspension, the phenomenon of acoustic wave propagation and scattering in an acoustically inhomogeneous medium is present in a natural way: as a result of the compressibility of the suspending fluid, thermally excited density fluctuations occur that can relax as a propagating longitudinal sound mode. Since the acoustic properties of the colloidal particles are in general different from those of the surrounding liquid, the acoustic waves are scattered. Colloidal suspensions are attractive candidates for studying the scattering of sound waves, as they allow to vary the important parameters (such as acoustic contrast and viscosity) and length scales (such as particle radius and interparticle distance) rela-

tively easily. Experiments on suspensions of PMMA particles in the strongly scattering regime revealed intriguing behavior: two propagating longitudinal sound modes were observed (in contrast to a pure fluid), as well as gaps in the dispersion relation [13]. In chapter 5 we study the propagation of acoustic waves in colloidal silica suspensions by means of Brillouin spectroscopy. The characteristics of acoustic wave propagation in these silica systems are found to be quite different from the PMMA particles, which are acoustically much softer. Only one longitudinal sound mode is observed. The phase velocity of this mode is reduced with respect to the pure fluid, similar to the behavior of porous media. The sound attenuation shows evidence for a coupling of neighboring scatterers by viscous forces.

2

Experimental techniques

2.1 Dynamic structure factor

In this thesis, we will be concerned with measurements of the dynamic structure factor of colloidal suspensions by means of light- and x-ray scattering techniques. The dynamic structure factor in the time domain, $S(q,t)$, describes the temporal decay of density fluctuations $\delta n(\mathbf{q},t)$. It is defined by the autocorrelation function

$$S(q,t) = \langle \delta n(-\mathbf{q},0)\delta n(\mathbf{q},t)\rangle, \tag{2.1}$$

, where $\mathbf{q}$ is the wave vector of the fluctuation, t denotes time and the brackets indicate an equilibrium ensemble average. In the frequency domain, the dynamic structure factor is given by

$$S(q,\omega) = \frac{1}{2\pi}\int_{-\infty}^{\infty} e^{-i\omega t}\langle \delta n(-\mathbf{q},0)\delta n(\mathbf{q},t)\rangle dt. \tag{2.2}$$

Two kinds of density fluctuations are of interest here: fluctuations in the number density of the colloidal particles and density fluctuations in the suspending fluid. The latter remain as the volume fraction of colloids approaches zero. Both kinds of density fluctuations cause spatial inhomogeneities in the refractive index $m(\mathbf{r},t)$. If light impinges on a colloidal suspension at a specific time t, it is scattered by these spatial inhomogeneities in the refractive index. By investigating the time evolution or the frequency components

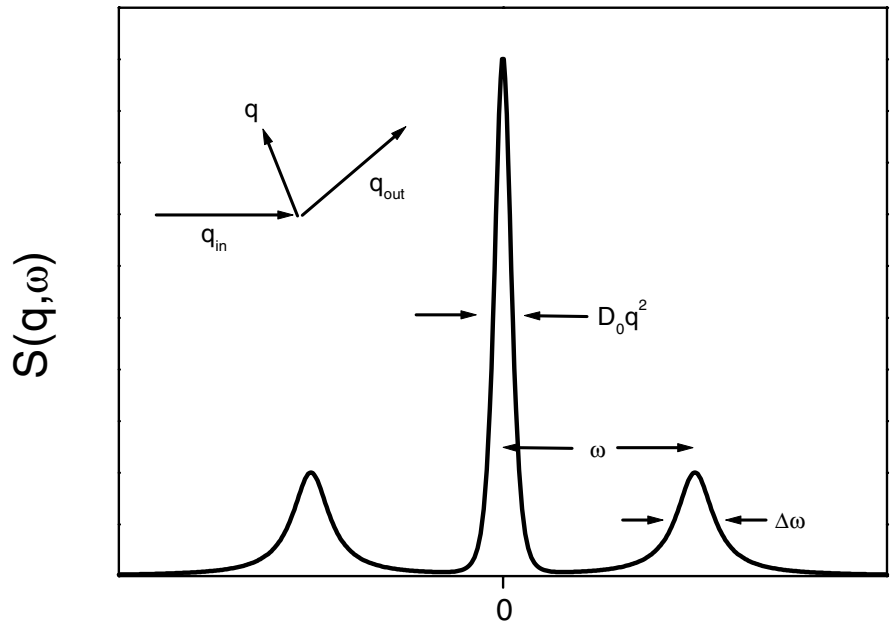

Figure 2.1: *Schematic drawing of the dynamic structure factor in the case of colloidal suspensions. The width of the central peak is determined by the colloidal diffusion coefficient D_0. The Brillouin peaks are shifted by a frequency difference $\pm\omega$ with respect to the central peak and their width is $\Delta\omega$. $\mathbf{q}_{in}$ and $\mathbf{q}_{out}$ are the wave vector of the incoming and scattered light, respectively.*

of the scattered light intensity it is, therefore, possible to obtain information on the relaxation of density fluctuations in the system.

In a colloidal fluid, fluctuations in the number density of colloids relax by diffusion, and light is therefore scattered quasi-elastically from these fluctuations. In chapters 3 and 4, we will employ two experimental techniques that are sensitive to this quasi- elastically scattered light: dynamic x-ray scattering (DXS) and dynamic light scattering (DLS). These scattering techniques measure the dynamic structure factor in the time domain. There is, however, also a small contribution of light that is inelastically scattered, i.e., whose frequency is shifted with respect to the incoming light. This frequency shift arises from the interaction of light with propagating density fluctuations, or

longitudinal sound modes [14]. Investigation of these sound modes by means of inelastic light scattering is called Brillouin spectroscopy, and we will apply this technique to suspensions of colloidal silica spheres in chapter 5. Brillouin spectroscopy yields the dynamic structure factor in the frequency domain.

Schematically, $S(q, \omega)$ will look as depicted in fig. 2.1. The central peak around $\omega = 0$ arises from the quasi-elastic scattering by the colloidal particles. In a dilute system, where the diffusion coefficient of the colloids does not depend on frequency, the width of the central peak is determined by the diffusion coefficient D_0 of the colloidal particles. This width is so small that it is hard to investigate in the frequency domain. Besides the (very strong) central peak, there are two peaks shifted with respect to the incoming frequency: the Brillouin doublet. The Brillouin scattering from sound modes is several orders of magnitude smaller than the quasi-elastic scattering from the colloids, even if the mean refractive index of the fluid approximately matches that of the colloidal particles. Because of the dominant role of the quasi-elastically scattered intensity, measuring the Brillouin doublet in a colloidal suspension is a challenging task, requiring an experimental technique that can separate the frequency components of the scattered light very sharply.

In a pure fluid, the dynamic structure factor looks qualitatively similar to fig. 2.1, but the central peak is then much smaller. The central peak in a pure fluid arises from temperature fluctuations (the density depends on temperature). The temperature fluctuations relax diffusively, and the width of the central peak is therefore given by the thermal diffusivity in this case.

In this chapter, we will give an overview of the experimental techniques used in this thesis to measure the dynamic structure factor.

2.2 Dynamic light- and x-ray scattering

2.2.1 Theory

Electromagnetic radiation impinging on a sample with a spatially inhomogeneous refractive index or electron density, such as a random assembly of colloidal particles suspended in a fluid, is scattered by these inhomogeneities. The electric field amplitudes scattered by different regions in the sample interfere and thus create an intensity distribution of dark and bright regions in the far field, called a speckle pattern. The speckle pattern reflects the instantaneous configuration of the scatterers. If the scatterers move, for instance

as a result of Brownian motion, the speckle pattern will change in time such that initially dark regions become bright and vice versa. Thus, if one places a detector of the size of a typical speckle spot at a particular point in the far field, the intensity measured at this point will fluctuate in time according to the movement of the scatterers. At times short compared to the typical time scale of configurational changes of the assembly of scatterers, the intensity at a given point in space will be correlated with the initial intensity. By contrast, at large times the speckle pattern will bear no relation with the initial pattern and the intensity correlation will thus be lost. This property is quantified by the intensity autocorrelation function

$$\overline{I(q,t)I(q,0)} = \lim_{T\to\infty} \frac{1}{T} \int_0^T I(q,\tau)I(q,\tau+t)d\tau, \tag{2.3}$$

where $I(q,t)$ is the scattered intensity. For an ergodic system, the time average implied by the bar is equivalent to an ensemble average. In a photon correlation spectroscopy experiment, a fluctuating signal proportional to $I(q,t)$ is fed into a computer that calculates the normalized intensity correlation function

$$g(q,t) = \frac{\langle I(q,t)I(q,0)\rangle}{\langle I(q)\rangle^2}. \tag{2.4}$$

Under the condition that the electric field amplitude $E(q,t)$ is a zero-mean complex Gaussian variable, $g(q,t)$ is given by

$$g(q,t) = 1 + \beta^2 \frac{\langle E^*(q,t)E(q,0)\rangle^2}{\langle I(q)\rangle^2} = 1 + \beta^2 |f(q,t)|^2, \tag{2.5}$$

where $f(q,t)$ is the normalized intermediate scattering function. The contrast $\beta^2 = g(q,0) - 1$ depends on the coherence of the beam, the coherence preserving properties of the optical elements in the setup and the number of coherence areas observed at the detector. For incoherent radiation, $\beta^2 = 0$ and $g(q,t) = 1$. Similarly, if the detector area is much larger than the speckle size the measured intensity will always be identical to the average intensity and thus $g(q,t) = 1$. In dynamic x-ray scattering experiments, optimizing the trade-off between the coherence and the available photon flux results in a contrast of typically 5 - 10 % [15, 16], whereas β^2 is usually close to the ideal value of 1 in a DLS experiment.

In the case of *single* scattering by an arrangement of N identical particles, the scattered field amplitude in the far field is (apart from unimportant

factors that are omitted) given by

$$E(q,t) \propto b(q) \sum_{j=1}^{N} e^{i\mathbf{q}\cdot\mathbf{r}_j(t)}, \tag{2.6}$$

where $\mathbf{r}_j(t)$ is the position vector of particle j. The scattering amplitude $b(q)$ is basically the Fourier transform of the refractive index profile $m_1(r)$ of a scatterer,

$$b(q) \propto 4\pi \int_0^\infty [m_1(r) - m_0] \frac{\sin qr}{qr} r^2 dr, \tag{2.7}$$

where m_0 is the refractive index of the surrounding medium. The mean intensity is related to the static structure factor $S(q)$:

$$\langle I(q) \rangle \propto b(q)^2 \sum_{j=1}^{N} \sum_{k=1}^{N} \langle e^{i\mathbf{q}\cdot[\mathbf{r}_j(0) - \mathbf{r}_k(0)]} \rangle \propto N b(q)^2 S(q). \tag{2.8}$$

It follows from eqs. 2.5, 2.6 and 2.8 that for identical particles the normalized intermediate scattering function is given by

$$f(q,t) = \frac{1}{S(q)} \frac{1}{N} \sum_{j=1}^{N} \sum_{k=1}^{N} \langle e^{i\mathbf{q}\cdot[\mathbf{r}_j(0) - \mathbf{r}_k(t)]} \rangle = \frac{S(q,t)}{S(q)}, \tag{2.9}$$

that is, $f(q,t)$ is directly related to the dynamic structure factor in the time domain. As is clear from eq. 2.9, the normalized intermediate scattering function contains correlations between the positions of different particles and thus depends on the interparticle interactions (see chapter 4).

For concentrated suspensions, where the decay of the dynamic structure factor is generally non-exponential, $f(q,t)$ is usually analyzed in terms of a cumulant expansion:

$$f(q,t) = e^{\Gamma_1(q)t + \Gamma_2(q)t^2 + \cdots}. \tag{2.10}$$

Here, $\Gamma_1(q)$ is the first cumulant [3]. In a dynamic light scattering experiment, one is interested in the wave vector dependent decay of the normalized intermediate scattering function. In particular, the initial decay of $f(q,t)$ gives the collective short time diffusion coefficient $D(q)$ of the colloidal suspension [3], according to

$$\lim_{t \to 0} \frac{d \ln f(q,t)}{dt} = \Gamma_1(q) = -D(q)q^2. \tag{2.11}$$

In a dilute system, the diffusion coefficient does not depend on q and the normalized intermediate scattering function becomes single exponential,

$$f(q,t) = e^{-D_0 q^2 t}, \tag{2.12}$$

where D_0 is the diffusion coefficient at infinite dilution.

In general, the mean intensity in eq. 2.8 may be written as

$$\langle I(q) \rangle \propto N b(0)^2 P(q) S(q), \tag{2.13}$$

where $P(q) = b(q)^2/b(0)^2$ is the particle form factor. In the case of spherical particles, the form factor is given by [3]

$$P(q) = \frac{9}{(qa)^6}[\sin(qa) - qa\cos(qa)]^2. \tag{2.14}$$

The relation 2.13 allows to obtain information on the static structure of the suspension from the time-averaged intensity. The form factor can be obtained from a dilute suspension, where $S(q) = 1$. In the case of x-rays, eq. 2.13 must be modified to [17]

$$\langle I(q) \rangle \propto N V^2 \Delta\rho_e^2 P(q) S(q), \tag{2.15}$$

where V is the particle volume and $\Delta\rho_e$ the difference in electron density between the colloids and their surroundings.

2.2.2 Multiple light scattering

Expressions 2.9, 2.11 and 2.13 only hold for single scattering of light. This means that if one wants to measure the collective diffusion coefficient $D(q)$ or the static structure factor by light scattering, it has to be assured that the measurements are performed in the single scattering limit. The single scattering limit is characterized by the condition

$$l_s \gg L, \tag{2.16}$$

where l_s is the mean distance between two scattering events (or scattering mean free path) and L the sample size.

In the dilute limit, the scattering mean free path is given by

$$l_s = \frac{1}{n_{coll}\sigma}, \tag{2.17}$$

where n_{coll} is the number density of colloids and σ the scattering cross section. Under the condition that the refractive index contrast is small, $|m_1/m_0-1| \ll 1$, and the "phase shifts" are small, $4\pi m_0 a|m_1/m_0 - 1|/\lambda \ll 1$, we have [18]

$$\sigma \propto \pi a^2 |m_1/m_0 - 1|^2. \tag{2.18}$$

In these expressions, a is the radius of the scatterers, m_1 their refractive index and λ the wavelength of the scattered light in vacuo. The conditions for the validity of eq. 2.18, which is known as the Rayleigh-Gans approximation, are always fulfilled for the systems considered here. It is seen from eqs. 2.16, 2.17 and 2.18 that the single scattering limit can be achieved by letting either $n_{coll} \to 0$ or $m_1/m_0 \to 1$ (or both), i.e., the sample has to be dilute or the refractive index of the scatterers has to be nearly matched to that of the surrounding medium. These requirements put severe limitations on the applicability of the dynamic light scattering technique: in the interesting case of high particle concentrations, where interparticle interactions become important, the necessity to match the refractive indices of the particles and the suspending fluid restricts the possibility to vary the direct interaction between the particles. The direct interaction depends sensitively on the properties of the suspending fluid and one would therefore like to have complete freedom of choice.

The opposite to condition 2.16, i.e. $l_s \ll L$, gives rise to multiple scattering, since then light is scattered many times on its path through the sample. In the case of strong multiple scattering, the transport of light intensity in the system can be modeled as a random walk between scatterers and is thus diffusive. The direction of light propagation will be randomized after only a few scattering events for diffusive light transport. The scattered intensity observed at any given point in space will then originate from a distribution of light paths in the sample. In other words, the light rays finally traveling in the direction of detection, $\mathbf{q}_{out}$, have originally been scattered in all possible directions and one therefore effectively observes an average over all possible scattering vectors $\mathbf{q}$. The essential wave-vector information is lost. The intensity correlation function decays much faster in the multiple scattering regime than in the single scattering limit, which is easily seen as follows. The phase difference between waves scattered by a particular scatterer at times t and $t + \Delta t$ is proportional to the distance the scatterer moves in the time interval Δt. If the light is multiply scattered by a large number of different scatterers, the phase differences accumulate and the time correlation will thus be lost quickly. In the limiting case of diffusive light transport, it is

nevertheless possible to extract useful information from intensity correlation functions, such as the size of the particles. Photon correlation spectroscopy in this limit is known as diffusing wave spectroscopy (DWS) [5].

2.2.3 Cross-correlated dynamic light scattering

The (strong) multiple scattering regime is characterized by the fact that the fraction of singly scattered light reaching the point of observation is small compared to the fraction of multiply scattered light. In this case, one cannot obtain q dependent information from dynamic light scattering. However, there will always be a certain fraction of singly scattered light leaving the sample. In this section, we describe the technique of cross-correlated dynamic light scattering with a single laser beam (CCDLS), with which it is possible to selectively detect the singly scattered component of the total scattered intensity and thus obtain the q dependent collective diffusion coefficient. The technique is applicable in cases where ordinary DLS has become unreliable due to multiple scattering, but the limit of diffusive light transport has not yet been reached. CCDLS has first been demonstrated experimentally by Meyer *et al.* [19]. Figure 2.2 shows the basic scattering geometry for CCDLS, as employed by these authors. A laser beam is focused into a sample cell, which is contained in a cylindrical index matching vat. The scattered light is coupled into two optical fibers that are separated vertically by a small distance Y. In terms of scattering vectors, the vertical distance between the fibers is $\Delta q = (4\pi m/\lambda)\sin(\Delta\varphi/2)$, where m is the refractive index of the suspension and $\Delta\varphi$ the angular distance between the fibers. The signal from the two fibers is fed into two detectors whose outputs are cross-correlated.

A theoretical treatment of CCDLS has been given by Lock [20]. This author calculated approximately the contributions of single and double scattering to the time dependent intensity cross-correlation function for the geometry shown in fig. 2.2, assuming a cylindrical scattering volume. We will not repeat the rather cumbersome (but straightforward) calculations here, but give a graphical representation of the main outcome instead. Figure 2.3 shows Locks result for the field correlation functions at $t = 0$ as a function of the fiber separation Δq. Figure 2.3(a) shows field correlation functions for singly and doubly scattered light, fig. 2.3(b) the ratio of the double scattering contribution to the intensity correlation function to the single scattering contribution. The calculations have been done for $m_1 = 1.465$, $m_0 = 1.400$, $a = 55$ nm, $\lambda = 532$ nm, $L = 2$ mm, $R_{foc} = 100$ μm, $R_{ave} = 2$ mm and

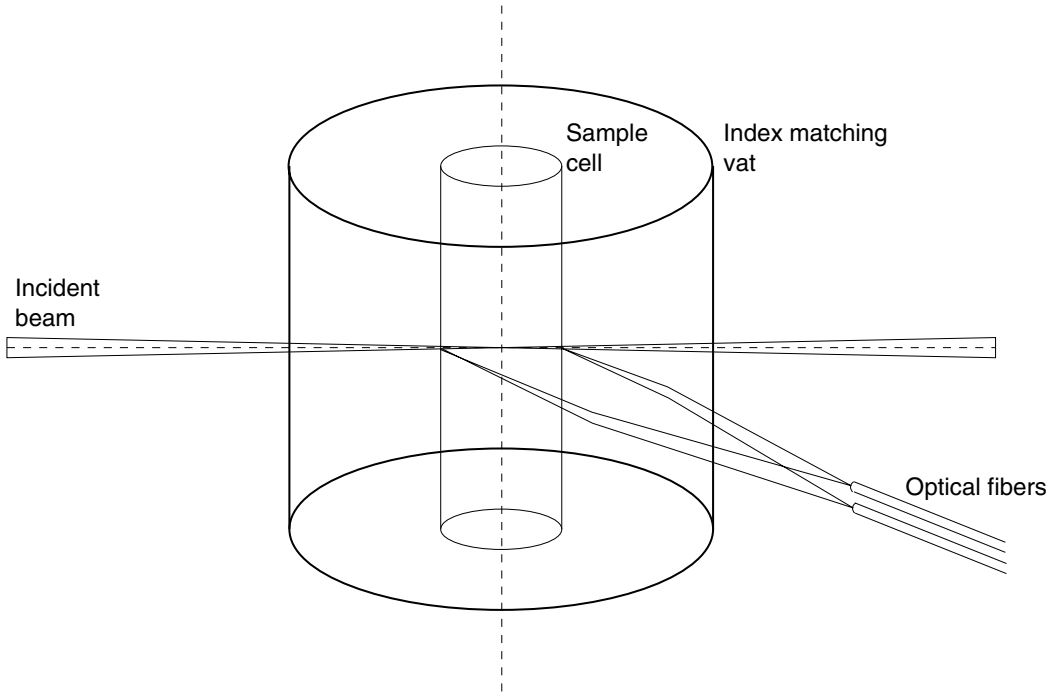

Figure 2.2: *Scattering geometry for cross-correlated dynamic light scattering with a single laser beam.*

$\phi = 0.1$. Here, R_{ave} is the radius out to which each particle is surrounded by an isotropic environment of other particles (which is comparable to the radius of the sample cell [20]), R_{foc} is the beam waist in the focus and ϕ is the volume fraction of particles. The correlation functions shown are

$$C_{1,2}(\Delta q) = \frac{\langle E^*_{1,2}(\mathbf{q} - \Delta\mathbf{q}/2, 0) E_{1,2}(\mathbf{q} + \Delta\mathbf{q}/2, 0)\rangle}{\langle E^*_1(\mathbf{q}, 0) E_1(\mathbf{q}, 0)\rangle}, \tag{2.19}$$

where the subscripts 1 and 2 refer to single and double scattering, respectively. It is seen from fig. 2.3(a) that for $\Delta q = 0$, i.e. autocorrelation, C_2 is by almost a factor 4 larger than C_1 for this particular example, meaning that double scattering contributes much more to the total field autocorrelation function than single scattering. However, as the fiber separation Δq is increased, C_2 decays much faster than C_1, such that the single scattering contribution becomes dominant at large fiber separation. From fig. 2.3(b) it is seen that the ratio of the double scattering contribution to the intensity

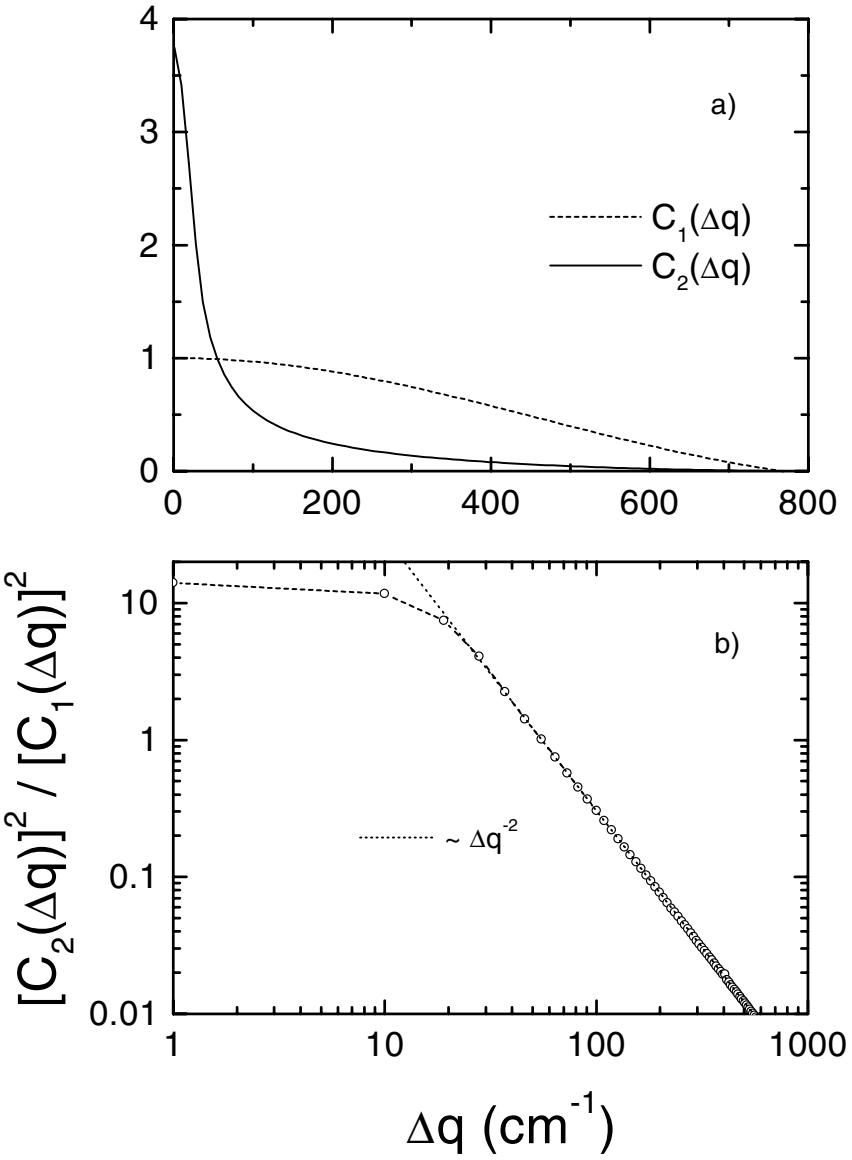

Figure 2.3: *(a) Electric field cross-correlation function for single scattering (C_1) and double scattering (C_2) at time $t = 0$ as a function of fiber distance. The correlation functions are normalized to C_1 at zero fiber distance. The system parameters are given in the text. (b) Ratio of the square of the correlation functions shown in (a), C_2^2/C_1^2, as a function of fiber separation.*

correlation function to the single scattering contribution, C_2^2/C_1^2, decreases as Δq^{-2} at larger fiber separations. For $\Delta q = 600$ cm^{-1}, the double scattering contribution is less than 1 % of the single scattering contribution in this particular case. The fiber separation at which this suppression of doubly scattered light is achieved is much smaller than the wave vectors q typically probed by dynamic light scattering, $\Delta q/q \approx 10^{-2}$; this ensures that the uncertainty in q introduced by CCDLS is negligible.

The theoretical analysis given by Lock demonstrates that CCDLS is in principle capable of separating singly from multiply scattered light. However, an experimental verification of the method as well as an investigation of its range of applicability in terms of l_s/L is highly desirable, if this technique is to be used for studying the dynamics of dense colloidal suspensions. Meyer *et al.* [19] measured the diffusion coefficient of polystyrene latex spheres suspended in water in a range of concentrations. The diffusion coefficient measured in cross-correlation was almost independent of concentration, whereas the one extracted from autocorrelation functions changed dramatically as the concentration of particles was increased. Furthermore, the cross-correlation functions were single exponential. From these observations they inferred that the cross-correlation functions were unaffected by multiple scattering. However, this is an indirect proof that relies on the assumption that the true diffusion coefficient is independent of concentration and the single-scattering correlation function is single exponential, which is only valid in the dilute limit. An independent test of the reliability of CCDLS has so far not been presented. In chapter 3, we will give the first *direct* and *independent* proof of the feasibility and reliability of CCDLS by directly comparing this new technique with dynamic x-ray scattering, where multiple scattering does not play a role.

Another cross-correlation dynamic light scattering technique is the so-called two-color dynamic light scattering method (TCDLS) [21, 22, 23]. In this technique, *two* laser beams with different colors are incident on the sample and the scattered light is detected by two spatially separated detectors. Each detector is sensitive to only one of the two colors. The relative positions of the detectors and the incoming beams are aligned such that both detectors probe the same scattering vector q for single scattering. For higher order scattering, light arriving at the detectors has initially been scattered in random directions and thus originates from different scattering vectors. As a result, the intensity cross-correlation of the detector outputs is much smaller for multiply scattered light than for singly scattered light and multi-

ple scattering detection is thus greatly suppressed, in a similar fashion as for the two-fiber CCDLS setup considered in this chapter. The main drawback of the TCDLS method is the tedious alignment procedure resulting from the fact that basically two complete DLS setups are used simultaneously, under the condition that both of these setups probe the same scattering volume and wave vector. Probably due to this difficult alignment, TCDLS has not been used extensively in practice. By contrast, the two-fiber CCDLS technique presented here is as easily to align and use as ordinary DLS and should therefore be suited for routine work. This simplification of the experimental setup is achieved by relaxing the requirement that both detectors probe *exactly* the same q for single scattering; instead, one allows a small separation in q space also for single scattering. The feasibility of TCDLS has been investigated by measuring concentration dependent correlation functions and diffusion coefficients on dilute systems similar to the experiments by Meyer *et al.* [19]. ¿From the fact that for cross-correlation the diffusion coefficient remained independent of concentration and the intensity correlation functions were single exponential, it was concluded that TCDLS effectively suppresses the detection of multiply scattered light [21]. We emphasize again that such an indirect way of demonstrating the potential of cross-correlation techniques fails for interacting particles, where the diffusion coefficient is intrinsically concentration dependent and the correlation functions non- exponential. Also for TCDLS, there is no independent, direct experimental verification. Therefore, since all cross-correlation dynamic light scattering techniques basically rely on the same physical principles, we believe that the results presented in this thesis are of general importance.

2.2.4 CCDLS setup

In the CCDLS setup (fig. 2.4), a diode pumped, frequency-doubled Nd:YAG laser (Coherent DPSS 532, $\lambda = 532$ nm) served as the light source. The beam was focused in the sample to a beam waist of about $R_{foc} = 100$ μm. The scattered light was collected by a lens with focal length 20 mm at a distance of $R_1 = 145$ mm from the sample and focused on a pinhole with a diameter of 100 μm. The pinhole served to eliminate stray light. The optical fibers were located at a distance of 395 mm from the sample. A slit in front of the fibers served to further reduce background light and to define the effective detector size in the horizontal direction. The fibers were mounted on a vertical slit whose size could be varied by means of a micrometer screw;

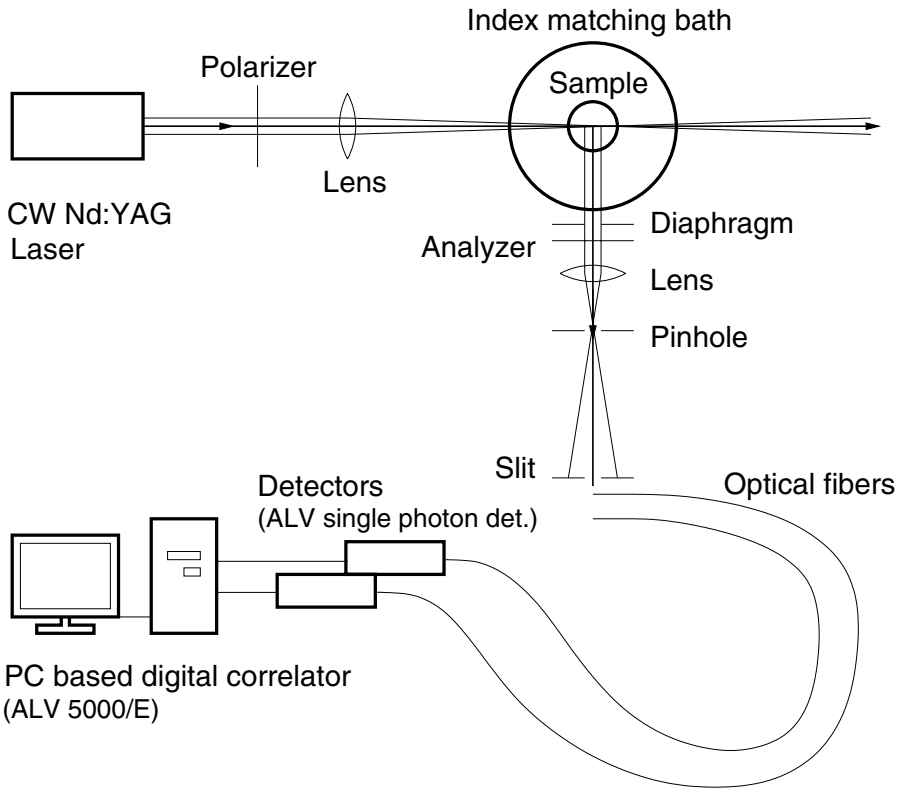

Figure 2.4: *Basic configuration of the cross-correlation dynamic light scattering setup.*

this allowed to vary the core-core fiber distance between 2.4 and 6.0 mm. The vertical extent of the single-scattering speckle at the position of the collecting lens should be of the order of $(\lambda/R_{foc})R_1 \approx 0.8$ mm. The collection optics leads to a magnification of the vertical speckle size by about a factor 10, i.e., the vertical extent of the speckle is about 8 mm at the position of the fibers. Therefore, singly scattered light is expected to be correlated within the range of fiber distances available. The apparatus was designed such that it could house the same sample cells as used for dynamic x-ray scattering, enabling us to perform both CCDLS and DXS on exactly the same samples. The sample cells were suspended in a bath of Toluene (Acros, 99 %, refractive index $m = 1.4965$) to reduce stray-light scattering from the cell walls. The temperature of the toluene bath was actively stabilized at 30 °C, using a feed-back mechanism (Malvern instruments temperature controller

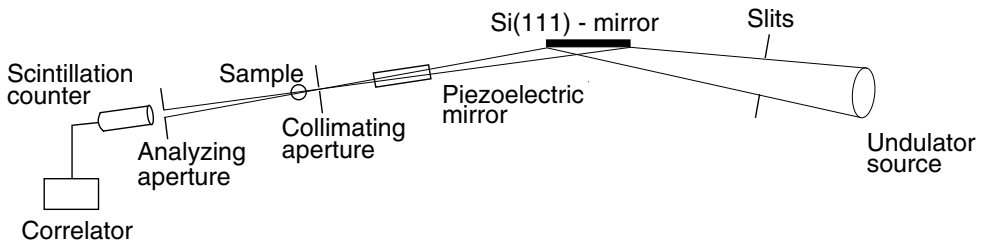

Figure 2.5: *Schematic diagram of the configuration of beamline ID10A at the European Synchrotron Radiation Facility.*

RR 56), to avoid a temperature difference between the CCDLS and the DXS measurements. Two multimode optical fibers (ALV, core diameter 300 μm) were used to couple the scattered light into two photomultipliers (ALV single photon detectors) whose outputs were cross-correlated. Correlation functions were calculated with a digital ALV5000/E correlator. A linear polarizer in the incoming beam and an analyzer in front of the collecting lens ensured that only the VV component of the scattered light was detected. The detectors were mounted on a rotation stage to vary the scattering angle.

In order to compare dynamic x-ray scattering with dynamic light scattering in the case of optically index matched samples, we employed a slightly different DLS setup with a single photomultiplier (Malvern instruments). This setup had been used extensively in previous experiments and has been described in detail in [24].

2.2.5 DXS setup

Dynamic x-ray scattering was performed at beamline ID10A of the European Synchrotron Radiation Facility in Grenoble [16]. Figure 2.5 shows a schematic drawing of the setup. The sample was illuminated with radiation of 8.2 keV energy (wavelength $\lambda = 1.51$ $\mathring{A}$), supplied by a single bounce Si(111) monochromator. A vertically focusing Rh-coated Si mirror was set to a critical energy just above 8.2 keV for harmonics rejection. Photon correlation spectroscopy requires the sample to be illuminated with coherent radiation. More specifically, the maximum path length difference in the sample has to be comparable to the longitudinal coherence length ξ_l and the lateral size of the scattering volume has to be comparable to the transverse coherence length ξ_t. The coherence length is the distance over which the phases of the beam re-

main correlated, either along the propagation direction (ξ_l) or perpendicular to it (ξ_t). Along the propagation direction, the phases become uncorrelated if the beam is not perfectly monochromatic[1]. Accordingly, the longitudinal coherence length is determined by the bandwidth $\Delta\lambda/\lambda$ of the x-ray source, $\xi_l \approx \lambda(\lambda/\Delta\lambda) = 1$ μm. The transverse coherence length is determined by the source size[2] S and the distance from the source R_s, $\xi_t \approx \lambda R_s/2S$. The maximum path length difference is $PLD = L[1 - \cos(\Theta)] + h\sin(\Theta)$, where L is the sample thickness, h the diameter of the scattering volume and Θ the scattering angle. The condition $PLD < \xi_l$ was fulfilled for $q < 0.96$ nm^{-1}, which was sufficient for the present experiments. The transverse coherence length was set by primary slits to 144 μm vertically and 14 μm horizontally at a distance $R_s = 44$ m from the source. A collimating pinhole aperture with a diameter of 20 μm was inserted 0.13 m upstream from the sample to select a partially coherent beam. We chose this configuration to optimize the trade-off between the degree of coherence on one hand and intensity- and stability requirements on the other. A guard slit was positioned right in front of the sample capillaries to eliminate parasitic scattering from the collimating aperture. In order to detect intensity fluctuations the detector aperture has to be comparable to the angular size λ/h of the intensity speckles. Therefore, an analyzing aperture of 30 μm size was placed in front of a scintillation counter at a distance of $R_2 = 2.3$ m from the sample. The speckle size at this position is approximately $R_2\lambda/h = 17$ μm. The sample cells were placed in an evacuated chamber which was heated to 30 °C with a Peltier element. Intensity correlation functions were recorded with digital ALV5000/E correlators. A reference correlation function was obtained from the air scattering just in front of the sample to record intensity fluctuations in the incoming beam. The time averaged signal from the scintillation counter was used for small-angle x-ray scattering measurements, keeping the experimental conditions unchanged with respect to the dynamic measurements.

[1]The phase difference in time t is $\Delta\omega t$, where $\Delta\omega$ is the frequency spread. We define the coherence time t_c by $\Delta\omega t_c = 2\pi$. The longitudinal coherence length then follows from $\xi_t = c_0 t_c$ and $\Delta\omega = c_0\Delta\lambda/\lambda^2$, where c_0 is the speed of light.

[2]Rays that are emitted at different points in an extended source have a phase difference if observed at a point transverse to the beam. This phase difference affects the visibility of interference fringes. One can define the transverse coherence length as the distance beyond which the visibility has reduced to less than 50 % [6].

2.3 Brillouin spectroscopy

2.3.1 Theory

In this section, we briefly summarize the theory underlying the Brillouin doublet shown schematically in fig 2.1. For a detailed description, we refer to [14].

The intensity of light scattered from a pure fluid is, to a good approximation, proportional to the dynamic structure factor, as given by eq. 2.2. Thus

$$I(q,\omega) = (\mathbf{e}_{in}\cdot\mathbf{e}_{out})^2\Big(\frac{\partial\varepsilon}{\partial n}\Big)^2_T S(q,\omega), \tag{2.20}$$

where $\mathbf{e}_{in}$ and $\mathbf{e}_{out}$ are the polarization vectors of the incoming and scattered light, respectively, ε the dielectric function and T the temperature[3]. This relation between the scattered intensity and the dynamic structure factor allows to measure $S(q,\omega)$ by Rayleigh-Brillouin scattering.

The dynamics of fluctuations in a pure fluid is governed by the continuity equation, the equation of motion, and the energy conservation equation. If the fluctuations are small, these equations may be linearized and then read [14, 25]

$$\begin{aligned} \frac{\partial\delta n}{\partial t} + n_0\nabla\cdot\mathbf{u} &= 0 \\ M n_0\frac{\partial\mathbf{u}}{\partial t} &= -\nabla\delta p + \eta\nabla^2\mathbf{u} + \Big(\eta_b + \frac{1}{3}\eta\Big)\nabla(\nabla\cdot\mathbf{u}) \\ \frac{\partial\delta e}{\partial t} + (e_0+p_0)\nabla\cdot\mathbf{u} &= \Lambda\nabla^2\delta T. \end{aligned} \tag{2.21}$$

Here, $\mathbf{u}$ is the fluid velocity field, M the molecular mass, p the pressure field, η the shear viscosity, η_b the bulk viscosity, e the density of internal energy and Λ the thermal conductivity. The space- and time dependence of all quantities appearing under the derivatives has been omitted for clarity. The subscript 0 denotes equilibrium values. The fluctuations in eqs. 2.21 are not all independent, but are related by the local equilibrium thermodynamic equations of state; this allows to eliminate two of the fluctuations and thus close the set of equations. The equations may then be solved by Laplace

[3]Equation 2.20 is only approximately correct since it neglects the dependence of the dielectric function on temperature (at constant density), which for most liquids is however small.

transform, which is a lengthy but straightforward procedure. We only give the final result for the dynamic structure factor here, which we are interested in:

$$\begin{aligned} S(q,\omega) &= \frac{1}{\pi}S(0)\Big\{(1-\frac{1}{\gamma})\frac{D_T q^2}{\omega^2+[D_T q^2]^2} \\ &+ \frac{1}{\gamma}(\frac{\Gamma_B q^2}{[\omega-\omega(q)]^2+[\Gamma_B q^2]^2}+\frac{\Gamma_B q^2}{[\omega+\omega(q)]^2+[\Gamma_B q^2]^2}) \\ &+ \frac{1}{\gamma}q\frac{3\Gamma_B - D_v}{\gamma c}(\frac{\omega+\omega(q)}{[\omega+\omega(q)]^2+[\Gamma_B q^2]^2}-\frac{\omega-\omega(q)}{[\omega-\omega(q)]^2+[\Gamma_B q^2]^2})\Big\}. \end{aligned} \tag{2.22}$$

Here, $S(0)$ is the static structure factor at $q=0$, $\gamma = C_p/C_v$ is the specific heat ratio, c the adiabatic sound velocity, $D_T = \Lambda/Mn_0C_p$ the thermal diffusivity, $D_v = \frac{\eta_b+\frac{4}{3}\eta}{Mn_0}$ the longitudinal kinematic viscosity and Γ_B the sound damping coefficient. The first term on the right hand side of eq. 2.22 represents the central peak (Rayleigh peak) of a *pure fluid*, whose width is given by the thermal diffusivity. The next two terms represent the Brillouin doublet. The Brillouin peaks have a Lorentzian line shape and are shifted by a frequency

$$\pm\omega(q) = \pm cq \tag{2.23}$$

with respect to the central peak. The full width at half maximum of the Brillouin peaks is given by

$$\Delta\omega = \Gamma_B q^2 = \Big(D_v + D_T(\gamma-1)\Big)q^2. \tag{2.24}$$

The last two terms in eq. 2.22 are usually negligible.

It is seen from the above equations that the sound velocity c can be obtained from the position of the Brillouin peaks and the sound damping from their width. In a colloidal suspension, the sound waves propagating in the fluid will be scattered by the colloidal particles. The scattering will add to the sound attenuation 2.24, which is the subject of chapter 5.

2.3.2 Brillouin setup

The setup used for Brillouin spectroscopy is shown schematically in fig. 2.6. Green light from an argon-ion laser (Coherent Innova 100) at a wavelength of 514.5 nm is split by a beam splitter cube. 99 % of the incoming light intensity is focused, via a movable arm, into the sample cell; the remaining 1

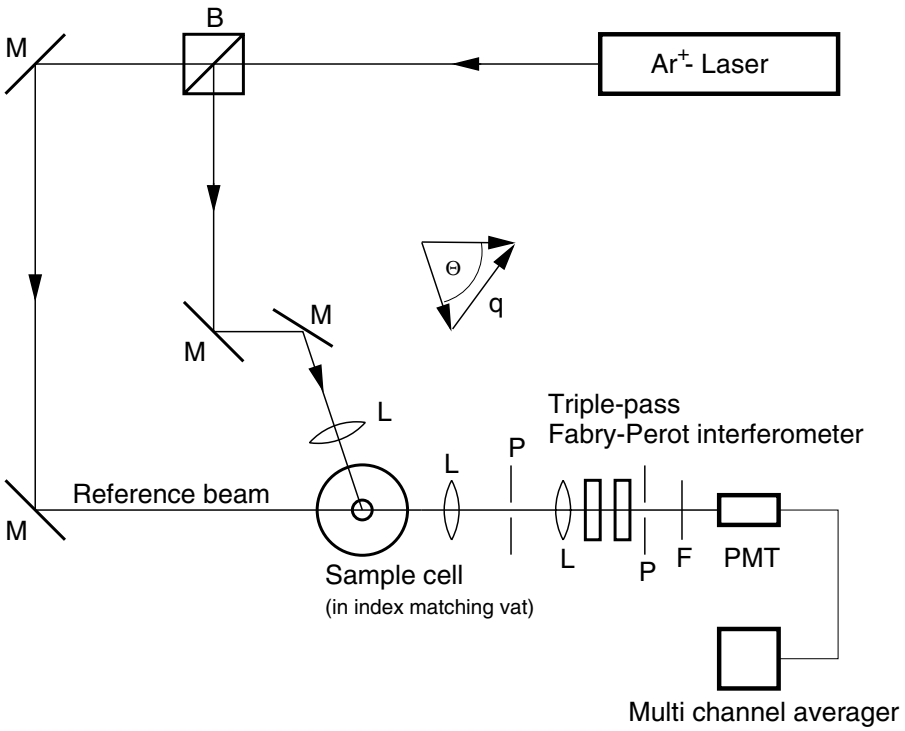

Figure 2.6: *Schematic drawing of the Brillouin setup. The meaning of the abbreviations is as follows: beam splitter (B), mirror (M), lens (L), pinhole (P), filter (F) and photomultiplier tube (PMT).*

% are used as a reference beam for alignment and stabilization. The sample cell is located in an index matching bath of glycerol ($m = 1.474$) to reduce stray light scattering from the cell walls. The scattered light is collected by a lens and focused onto a pinhole, defining the outgoing wave vector. The magnitude of the scattering vector $\mathbf{q}$ is related to the scattering angle Θ by[4] [14]

$$q = \frac{4\pi m}{\lambda} \sin(\Theta/2), \tag{2.25}$$

where m is the index of refraction of the suspension. The scattered light is then collimated into a triple-pass Fabry-Perot (FP) interferometer (Burleigh instruments) and detected at the exit of the interferometer by a photomulti-

[4]Equation 2.25, which is strictly valid only for elastic scattering, holds to a very good approximation since the Brillouin shift is very small.

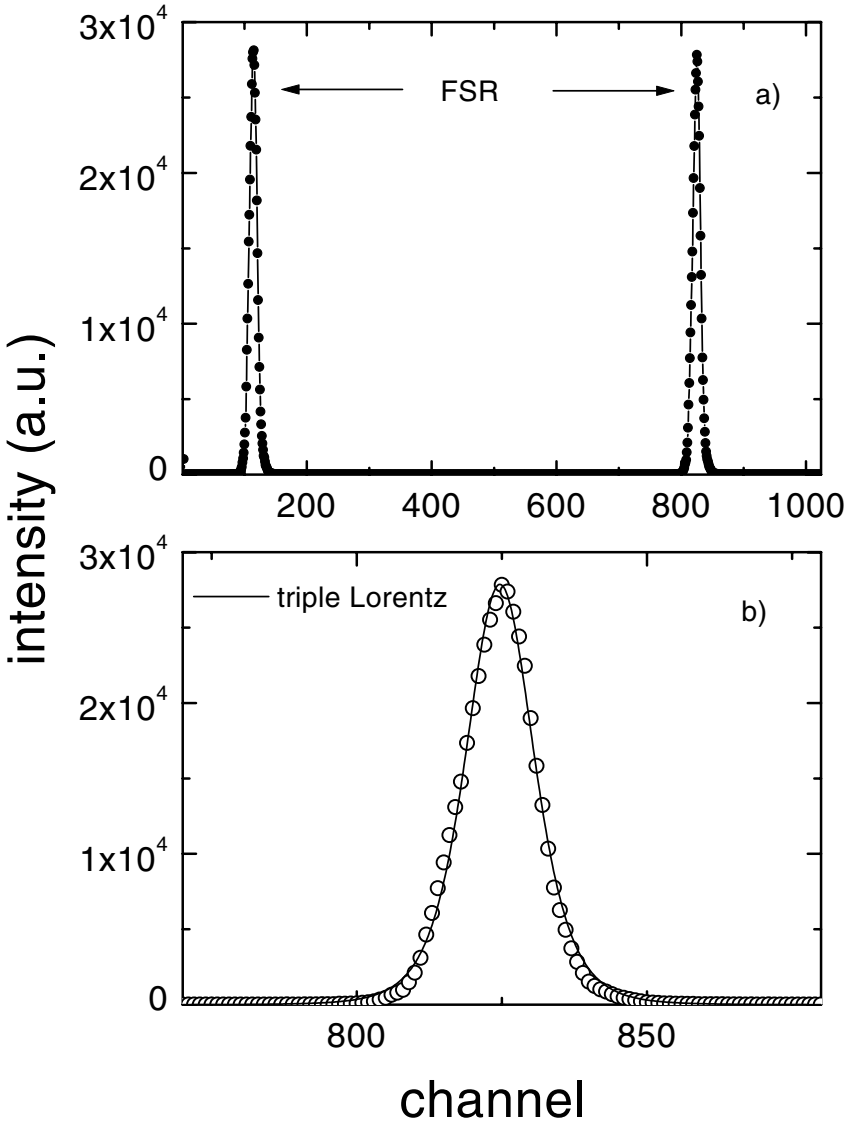

Figure 2.7: *Transmission of the triple-pass Fabry-Perot interferometer as a function of averager channel. The distance between two consecutive orders defines the free spectral range (FSR). The solid line in (b) represents a fit to the transmission peak with the third power of a Lorentzian curve.*

plier tube (PMT, Products for Research inc.). The interferometer is operated in triple-pass configuration to achieve a high contrast; this is necessitated by the fact that the intensity of the central Rayleigh peak for colloidal suspensions is several orders of magnitude larger than that of the Brillouin peaks, even if the average refractive indices of the colloids and the suspending fluid closely match. An additional interference filter for 514.5 nm in front of the PMT serves to further reduce background light. The distance between the mirrors of the FP is scanned piezoelectrically, using a programmable ramp generator (Burleigh RC 43). The signal from the PMT is fed into a multichannel averager (EG & G 4202), triggered by the ramp generator. The FP is placed in a temperature stabilized container to minimize thermal drift. The remaining thermal drift is actively compensated by applying a compensation voltage to the piezoelectric crystals on the FP mirrors. The compensation voltage is controlled by a feedback mechanism that keeps a reference signal, either the reference beam or the strong central Rayleigh peak, within a given time window for each scan (Burleigh DAS-10 FP stabilization system). The PMT is cooled to 0 °C to reduce dark counts.

Figure 2.7 shows the transmission of the Fabry-Perot interferometer as a function of the averager channel, which is proportional to the mirror distance. The measurement was obtained with the reference beam. Figure 2.7(a) shows a scan over one free spectral range (FSR), fig. 2.7 focuses on one of the transmission peaks. Light is transmitted through the FP whenever the mirror distance is a multiple of half the light wavelength, since then light waves, that are multiply reflected between the mirrors, interfere constructively at the exit of the FP. The transmission peaks are broadened mainly as a result of the finite mirror reflectivity and deviations from perfect parallelism of the mirrors. Figure 2.7(b) shows the line shape of a transmission peak. For a triple-pass FP, the instrumental line shape $T(\omega)$ may be approximated by a triple Lorentzian [26]:

$$T(\omega) \approx \frac{A}{[1 + k^2(\omega - \omega_0)^2]^3}, \tag{2.26}$$

where A is the amplitude, ω_0 the central frequency, and the full width at half maximum is given by $1.02/k$. The line in fig. 2.7(b) represents a fit to the transmission peak with eq. 2.26. It is seen that the line shape is represented reasonably well by a triple Lorentzian, although deviations are apparent in the wings. From the ratio of the amplitude to the background,

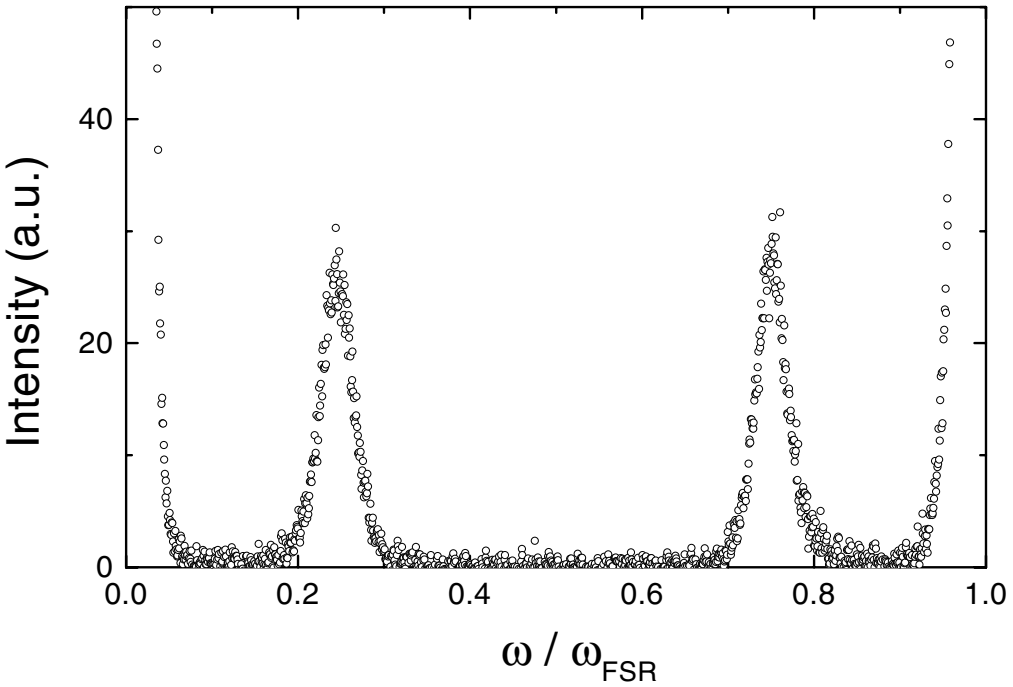

Figure 2.8: *Brillouin spectrum of pure ethanol. The scattering angle* $\Theta = 90°$*. The strong transmission peaks at* $\omega/\omega_{FSR} = 0, 1$ *(off scale) are due to the reference beam, which has been admitted for stabilization.*

which is hardly visible on this scale, we obtain a contrast of 10^5. The finesse (the ratio of the FSR to the peak width) is 52.

Calibration of the setup To calibrate the FSR of the interferometer, we measured a series of Brillouin spectra in pure ethanol. Figure 2.8 depicts a Brillouin spectrum of pure ethanol at a scattering angle of $\Theta = 90°$, obtained from an average over about 10^3 sweeps. The two Brillouin peaks are clearly visible on this scale. To stabilize the FP, part of the reference beam has been admitted, which gives the strong peaks at $\omega/\omega_{FSR} = 0, 1$. From a Lorentzian fit to the Brillouin peaks we find that the Brillouin shifts of the two orders agree to within 1 % and the widths to within 4 %; this indicates a good linearity of the scan and reasonable stability of the setup.

Figure 2.9 shows the position of the Brillouin peaks as a function of the

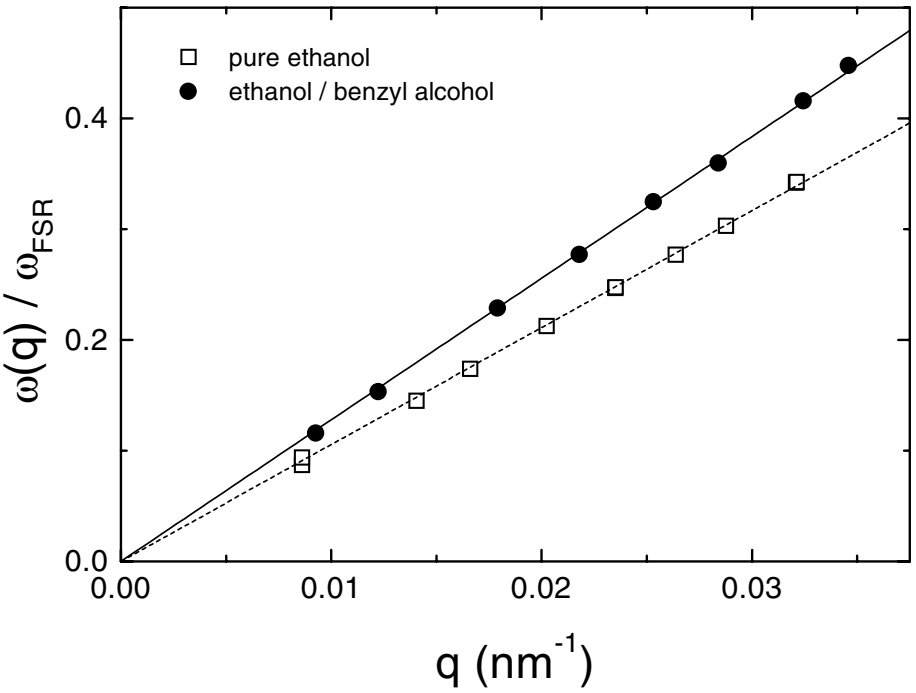

Figure 2.9: *Position of the Brillouin peaks for pure ethanol (squares) and a mixture of ethanol and 58 vol% benzyl alcohol (circles) as a function of scattering vector. The straight lines are linear fits to the data.*

scattering vector q. Data are shown for pure ethanol and a mixture of ethanol and 58 vol% benzyl alcohol. This alcohol mixture is used later as index matching solvent for the colloids. It is seen that the peak position depends linearly on the wave vector, as expected for a pure fluid. The straight lines in fig. 2.9 are linear fits to the data. The slope of the lines should be given by the sound velocity (see eq. 2.23), which allows to determine the free spectral range; we find $\nu_{FSR} = 18.19 \pm 0.06$ GHz. Having obtained the FSR from the ethanol measurements, we can determine the sound velocity of the ethanol/ benzyl alcohol mixture to be $c = 1462 \pm 7$ m/s. This result is in good agreement with $\bar{c} = 1400$ m/s, where $\bar{c} = \phi_1 c_1 + \phi_2 c_2$ is the volume average of the sound velocities of the two fluids (with $c_{ethanol} = 1207$ m/s [27] and $c_{benz.al.} = 1540$ m/s [28]).

2.4 Sample preparation and characterization

In all experiments we used colloidal silica spheres (mean radius $a = 54.9 \pm 0.1$ nm, polydispersity $\Delta a/a = 0.042 \pm 0.005$, density $\rho = 1.93 \pm 0.03$ g/cm^3, refractive index $m = 1.465 \pm 0.004$), synthesized following the micro emulsion technique [4]. The particles were suspended in varying fluids (ethanol, benzyl alcohol, ethanol/benzyl alcohol mixtures, or water/glycerol mixtures, depending on the purpose) by centrifuging the initial stock suspension, removing the supernatant, and adding the desired solvent; this procedure was repeated several times for rinsing. The fluids were filtered several times (Millipore filters, pore size 0.45 or 0.2 μm) to remove dust particles. The particle density was determined by drying a concentrated suspension of known volume and weight in a solvent of known density and weighing the residue. The volume fraction of the samples was determined by drying a known volume at 90 °C and weighing the residue; weight concentrations were converted to volume fractions using the measured particle density. The refractive index of the silica particles was determined by measuring the light transmission (at a wavelength of 532 nm) in the forward direction for suspensions in different mixtures of ethanol ($m = 1.359$) and benzyl alcohol ($m = 1.538$), at a constant temperature of 25 °C. The maximum in transmission defined the point of index matching. The refractive indices of the alcohol mixtures were measured with an Abbe refractometer, thermostated at 25 °C [29].

For the Brillouin experiments, the silica particles were suspended in an optically index matching mixture of ethanol and benzyl alcohol, in order to reduce the intensity of the central Rayleigh peak and to avoid multiple light scattering. A sample with a maximum volume fraction of colloids was produced by centrifuging a concentrated suspension at 3000 rpm in the sample cell and removing all of the remaining fluid. The resulting suspension was a highly viscous, transparent sediment. Samples of lower volume fraction were produced by adding known amounts of fluid to the initial suspension. The colloids were resuspended by stirring and with aid of an ultrasonic bath. The sample cell was a cylindrical quartz cuvette with an inner diameter of 8 mm. At each step in the dilution series, the height of the suspension in the cuvette, and thus the total volume, was measured. The volume fraction was determined by drying a known amount of the last suspension in the series, i.e., the most dilute one, and weighing the residue. The volume fractions of the more concentrated samples were then determined relative to the most dilute one, according to the known volumes of these suspensions as measured

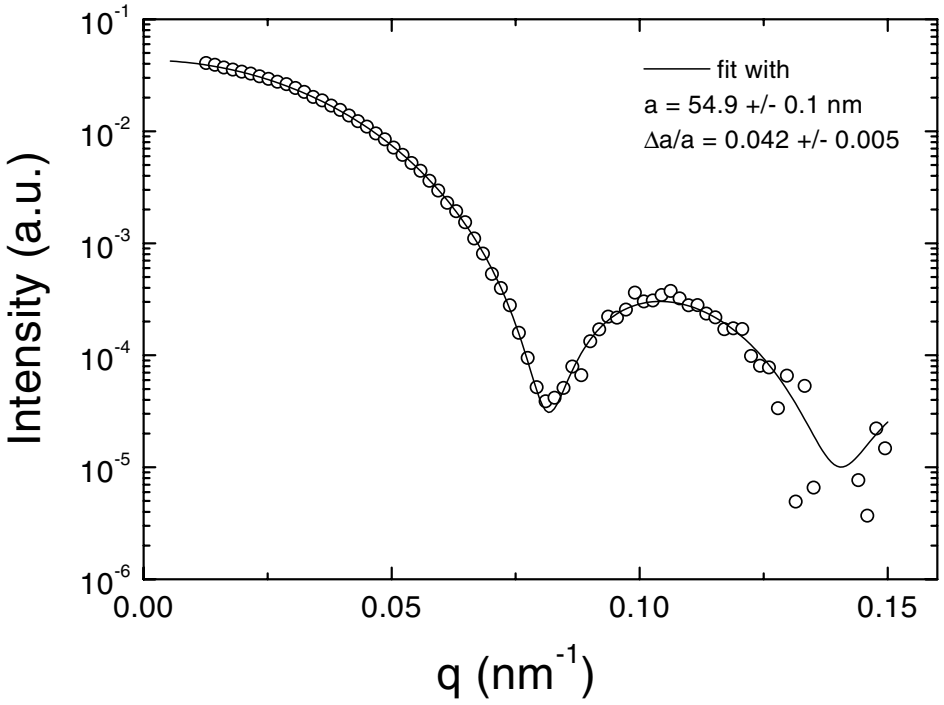

Figure 2.10: *Small angle x-ray scattering intensity for a dilute sample of silica colloids in a mixture of ethanol and benzyl alcohol. The solid line represents a fit to the data with the form factor for spherical particles.*

before. In this way, the range of volume fractions was determined to have been $0.077 \leq \phi \leq 0.63$, i.e., the initial sediment consisted of an almost randomly close packed structure. This finding is in accordance with the results of Ballato *et al.* [30], who investigated the influence of forced sedimentation (centrifugation) on the microstructure of the resulting colloidal sediment. They found, by field emission scanning electron microscopy, that centrifuged silica colloids formed a disordered sediment, whereas an ordered structure was obtained for undisturbed sedimentation.

The size and polydispersity of the particles was determined by measuring the particle form factor with small-angle x-ray scattering (SAXS) at the ESRF (for a drawing of the setup see fig. 2.5). SAXS is an ideal tool for the characterization of colloidal particles due to the fact that multiple scattering is absent for x-rays and, more importantly, it covers a much wider q range

than static light scattering [31]. Figure 2.10 shows the static scattered x-ray intensity for a dilute ($\phi < 0.005$) sample in an index matching mixture of ethanol and benzyl alcohol. The data are fitted to the form factor expression for spherical particles (eq. 2.14), with an additional prefactor to adjust the absolute value. Expression 2.14 was convoluted with a Schulz distribution for the particle radius to account for polydispersity [9]. As can be seen from fig. 2.10, an almost perfect fit is obtained with $a = 54.9 \pm 0.1$ nm and $\Delta a/a = 0.042 \pm 0.005$.

3

Photon correlation spectroscopy: x rays versus visible light

We perform a direct comparison of cross-correlated dynamic light scattering (CCDLS) and dynamic x-ray scattering (DXS) for colloidal suspensions that are optically opaque due to multiple light scattering. Then, the dynamics cannot be probed by ordinary photon correlation spectroscopy with visible light. By contrast, multiple scattering is absent for x rays because of the small scattering cross section. Using DXS as a reference, we demonstrate that the detection of multiply scattered light can be suppressed by cross-correlating the signals from two closely spaced detectors. This comparison provides an independent, direct proof of the feasibility of CCDLS in the case of concentrated colloidal dispersions with interparticle interactions.

3.1 Introduction

Photon correlation spectroscopy is one of the most important techniques with which to study dynamical phenomena in soft condensed matter [3, 9]. If a random arrangement of scatterers is illuminated with coherent radiation, the scattered intensity shows a grainy interference pattern that reflects the instantaneous configuration of the scatterers [32]. Movement of the scatterers causes a corresponding movement of this so-called speckle pattern, which thus contains information about the dynamics of the system. Photon correlation spectroscopy measures the time dependent intensity (auto)correlation

function of the speckle pattern at a given spatial position. Correlation spectroscopy with visible light, known as dynamic light scattering (DLS), is a well established and widely used technique [33]. However, DLS suffers from one major drawback that severely restricts its applicability: multiple light scattering. This problem arises in particular for colloidal suspensions, which have been investigated quite extensively with DLS. Since the size of colloidal particles is of the order of the wavelength of visible light, they scatter light very efficiently. As a result, multiple scattering becomes important in dense colloidal systems as soon as the refractive index of the suspending fluid differs significantly from that of the particles. Multiple scattering of light renders the measurement of quantities depending on the scattering vector q difficult, since scattered light observed at a given point in space then originates from a wide range of possible light paths in the sample [5]. In recent years, two new experimental techniques have emerged that overcome the multiple-scattering problem: dynamic x-ray scattering (DXS) [34, 35, 36, 37, 38] and cross-correlated dynamic light scattering (CCDLS and TCDLS) [19, 20, 21, 22, 23, 39, 40, 41]. DXS has the additional advantage of enlarging the wave vector range substantially, giving access to dynamic processes on an atomic length scale. By contrast, DLS cannot probe the dynamics on a length scale smaller than about 200 nm.

These recent exciting experimental developments have, in principle, expanded the potential of correlation spectroscopy enormously. However, up to now only the feasibility of DXS has been demonstrated. These feasibility studies have been performed mainly on systems displaying ultra slow dynamics (i.e. on the second time scale), such as colloidal particles suspended in glycerol [34, 35, 37] and polymer micelle liquids [36]. Faster dynamics has hitherto only been studied in the case of strongly scattering palladium aggregates [38] and in the dilute limit [42]. Examples of optically opaque systems, where the use of DXS would be of great advantage, are abundant, e.g. concentrated colloidal suspensions in aqueous environments and protein solutions. However, the absence of multiple scattering for x rays is payed by the low scattering cross section. Performing photon correlation measurements under these conditions is a challenging task due to intensity limitations, the pulsed nature of synchrotron sources, and the imperfect coherence properties of the x-ray beam. It is essential to investigate, therefore, whether DXS gives accurate and reliable results, and can thus be employed as a substitute for DLS, in systems comparable to those conventionally studied with visible light.

Concerning cross-correlated dynamic light scattering, it is not clear to which extent and under which conditions this technique suppresses the detection of multiply scattered light sufficiently. The reason is that there has been no independent, multiple- scattering free technique with which to compare CCDLS. As a consequence, all indications that CCDLS is indeed capable of suppressing multiple scattering contributions are of an indirect nature and are only conclusive for dilute systems, where interparticle interactions are absent. Going to higher concentrations, one faces the problem that multiple scattering increases and at the same time, interaction effects become important; both have qualitatively similar effects on the correlation functions. It is therefore impossible to separate both effects without prior knowledge of the interparticle interactions, which is however exactly the information one hopes to obtain from DLS experiments.

In this chapter, we report on a direct comparison of DLS, DXS and CCDLS. The goal of this comparison is to establish the potential of DXS and CCDLS as tools for investigating the dynamics of concentrated colloidal suspensions with fast dynamics. To this end, we study the diffusion of colloidal silica particles suspended in different liquids. We first demonstrate by a comparison of the correlation functions obtained with DLS and DXS on optically index matched samples that DXS gives accurate and reliable results. Then, having established the reliability of DXS, we use dynamic x-ray scattering to investigate the feasibility of CCDLS. By a direct comparison of the correlation functions obtained with these two techniques on optically opaque samples we show that the detection of multiply scattered light can effectively be suppressed by cross-correlating the signals from two closely spaced optical fibers. The results reported in this chapter open up the way to a new combination of experimental techniques that enables us to study the dynamics of dense, optically opaque colloidal suspensions over a wide range of scattering vectors: dynamic x-ray scattering, cross-correlated dynamic light scattering and small angle x-ray scattering. This combination overcomes the requirement to match the refractive indices of the colloidal particles and the suspending medium in order to avoid multiple scattering. As a consequence, we have complete freedom to tune the direct interaction between the colloids, allowing us to study the interplay between static and dynamic properties purely experimentally, without taking recourse to any theoretical model beforehand. We will report on these experiments in chapter 4.

3.2 Experimental

To induce multiple scattering of light in a controlled way, samples of varying refractive index contrast were produced by mixing different amounts of suspensions in ethanol (Aldrich, spectrophotometric grade, $m = 1.359$ [27]) and benzyl alcohol (Aldrich, 99.8 %, anhydrous, $m = 1.538$ [27]). The volume fraction of the samples was $\phi = 0.078 \pm 0.002$ and 0.164 ± 0.003. The suspensions were sealed in cylindrical thin-walled glass capillaries (Müller Glas, diameter 2 mm, wall thickness 1/100 mm) that are suited for x-ray spectroscopy. Further details about the sample preparation and characterization are given in section 2.4.

The experimental setups used for cross-correlated dynamic light scattering and dynamic x-ray scattering are described in detail in sections 2.2.4 and 2.2.5.

3.3 Results

3.3.1 Optically index matched sample

In this subsection, we investigate the performance and reliability of the new DXS technique in the case of fast moving colloidal suspensions. To this end, we compare DXS with the well-established DLS technique with a single laser beam and a single detector. To avoid multiple light scattering, we use an optically index matched sample (colloid volume fraction $\phi = 0.164$).

Figure 3.1 shows an example of an intensity autocorrelation function, $g(t)$, obtained with x rays. The pulsed nature of the synchrotron source causes oscillations with a period corresponding to the repeat time of the electron bunches in the storage ring. These oscillations dominate the correlation function at small times [Fig. 3.1(a)]. At larger times (t > 0.03 ms), the correlation function of the sample scattering is seen. For comparison a reference correlation function taken with the incoming beam is shown, which only exhibits the source fluctuation. The correlation times of the sample dynamics are of the order of 100 μs or longer, whereas the period of the source oscillations is about 3 μs. To average out the source fluctuations, the data were rebinned, i.e., the minimum sampling time was effectively increased from 400 ns to 6.4 μs. The correlation function was then divided by the reference signal to eliminate residual correlations in the source, yielding the function shown in

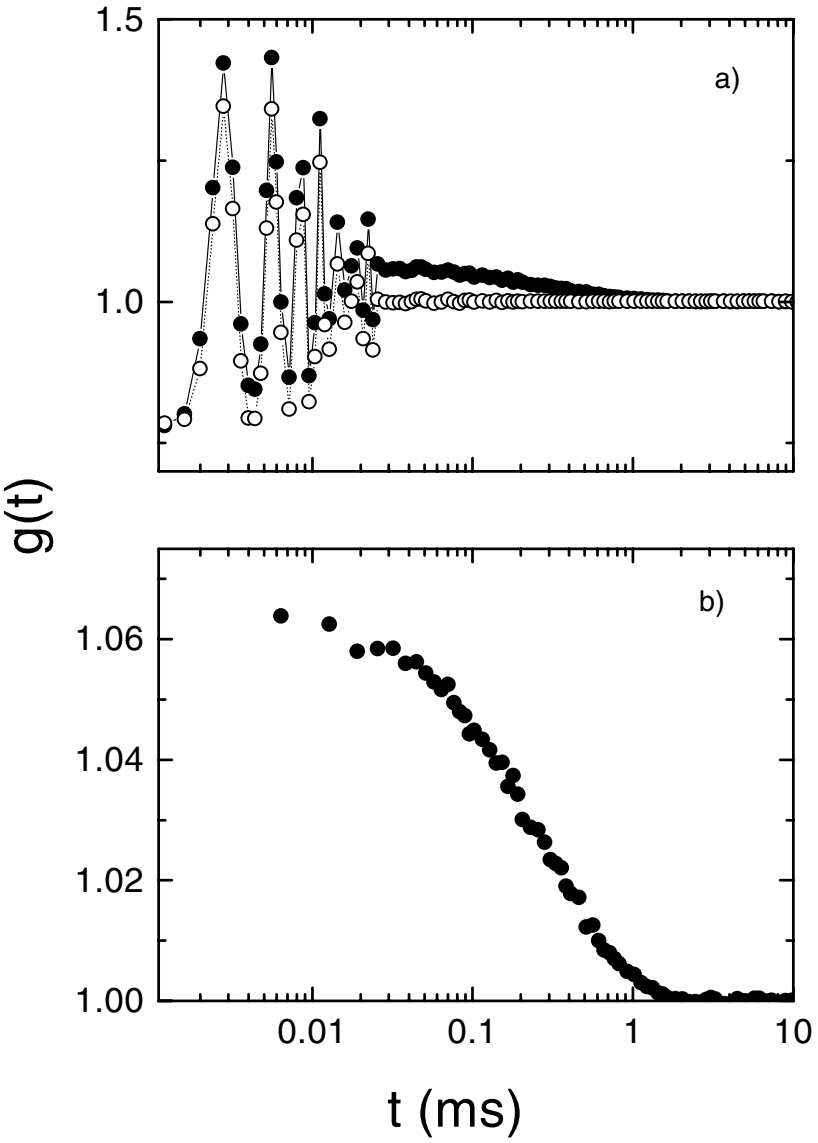

Figure 3.1: *Intensity correlation functions obtained with coherent x rays on a sample of silica colloids in a mixture of ethanol and benzyl alcohol. (a) Raw data (bullets) and reference signal (open circles). (b) Correlation function after rebinning and division by the reference. The scattering vector* $q = 0.0461\ nm^{-1}$.

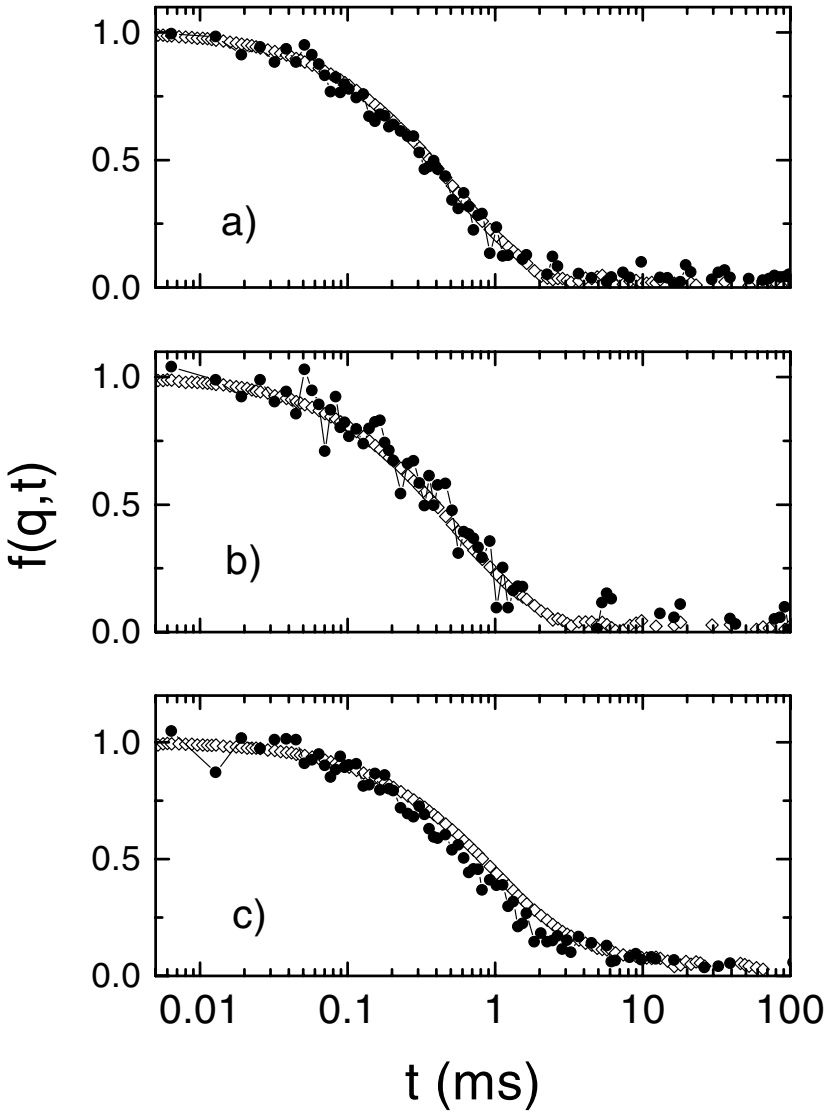

Figure 3.2: *Comparison of intermediate scattering functions obtained with both x rays (bullets) and visible light (diamonds). The comparison is done for an optically transparent sample at different scattering vectors:* $q = 0.0295(0.0297)$ nm^{-1} *(a),* $0.0241(0.0238)$ nm^{-1} *(b) and* $0.0144(0.0149)$ nm^{-1} *(c). The q values in parenthesis refer to x rays.*

Fig. 3.1(b).

In Fig. 3.2, we show intermediate scattering functions obtained with both DLS and DXS at almost identical scattering vectors on the index matched sample. The q vectors in this figure lie at the large q end for light, but at the low q side for x rays; the overlap allows a direct comparison of both techniques. As can be seen from Fig. 3.2, the intermediate scattering functions measured with x rays are in good agreement with those obtained by DLS (the small difference between DLS and DXS for the lowest q is due to the fact that the functions were measured at slightly different scattering vectors). This comparison demonstrates that DXS yields accurate and reliable results for the dynamics of colloidal suspensions. By using a system comparable to those conventionally studied with light, we have shown that DXS can nowadays be used in the same time domain as DLS and should therefore be suitable as a substitute for DLS in cases where DLS fails due to multiple scattering.

3.3.2 Variation of the optical contrast

In the following, we will employ DXS to establish the feasibility of cross-correlated dynamic light scattering. Since multiple scattering is absent for x rays, this is probably the only independent, direct way of assessing the potential of CCDLS. To elucidate the significance of this point, we show a number of calculated intermediate scattering functions, together with a measured correlation function on a dense, index matched sample ($\phi = 0.3$), in fig. 3.3. The calculations have been done for a scattering angle of 90°; the time axis has been normalized by $\tau_0 = 1/D_0q^2$. In a dilute system, the correlation function exhibits a single exponential decay (dashed line). Contributions from double scattering (dotted line, ratio double scattering to single scattering 1/1) lead to a non-exponential decay [20]. Double scattering not only influences the initial decay, which becomes more rapid than in the dilute limit, but also the long-time behavior. The dash-dotted and the dash-double-dotted line represent the diffusing wave limits in the backward- and forward scattering geometries, respectively [5]. The correlation functions in the diffusing limit are strongly non-exponential and deviate enormously from the single-scattering correlation function, indicating that multiple scattering strongly distorts the correlation functions. In fact, multiple scattering spoils the relation between the correlation function and the q dependent diffusion coefficient, $D(q)$, and non-exponentiality factor, $\Delta(q)$ [43] (see chapter 4, eq.

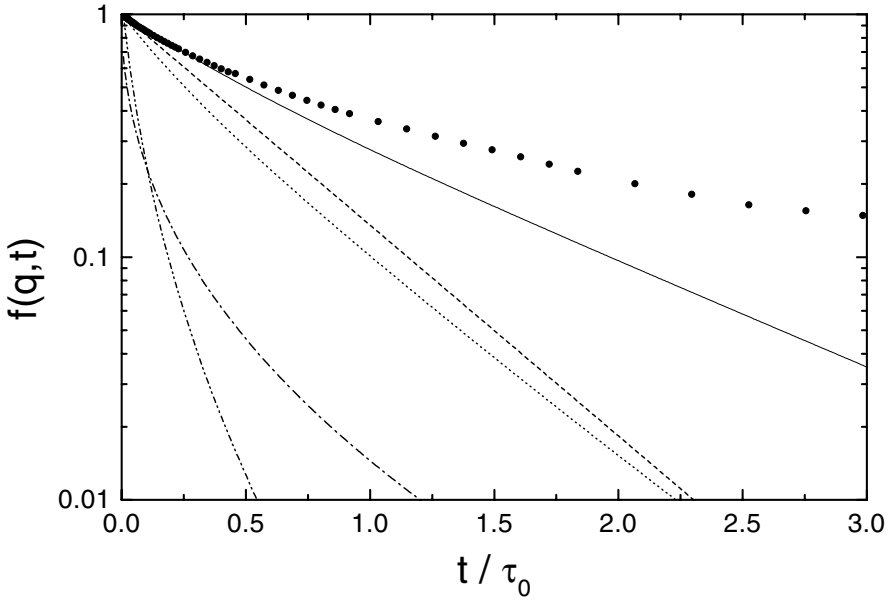

Figure 3.3: *Intermediate scattering functions for: a dilute system in the single scattering limit (dashed line), single scattering and contributions from double scattering (dotted line), the diffuse limit in forward scattering geometry (dash-double-dotted line), the diffuse limit in backward scattering geometry (dash-dotted line), single scattering in the case of heterodyne detection (solid line), and single scattering in a dense system (circles). The time axis is reduced with* $\tau_0 = 1/D_0q^2$. *The scattering angle* $\theta = 90°$.

4.5). In the diffuse limit, however, there is at least a model to interpret the correlation functions in terms of an average diffusion coefficient [5]. By contrast, in the region between single scattering and diffuse limit, an interpretation of the correlation function in terms of quantities related to colloidal dynamics is hardly possible. The solid line in fig. 3.3 shows a single scattering correlation function in the case of heterodyne detection [24], i.e., in the presence of a constant intensity I_c in addition to the fluctuating intensity ($I_c/\langle I\rangle = 0.5$). Heterodyning also leads to a non-exponential correlation function, the initial decay being less rapid than in the homodyne case. The circles show a measured correlation function on a dense system. The correlation function on the dense sample is strongly non-exponential as a result of interparticle interactions. Another effect that leads to non-exponential cor-

relation functions is size polydispersity [9]. We see from this discussion that a number of very different effects have a qualitatively similar influence on the form of the correlation functions, complicating the interpretation of their time dependence. Up to now, the feasibility of cross-correlation dynamic light scattering techniques has been demonstrated on dilute systems indirectly by showing that the correlation functions obtained with these techniques were single exponential [19, 21]. It is clear from fig. 3.3 that in a dense system, where the correlation function is *intrinsically non-exponential*, this kind of indirect proof breaks down. Without prior knowledge of the contributions of heterodyne detection, polydispersity and, above all, interparticle interactions it is impossible to draw conclusions about the importance of multiple scattering from the form of the correlation function in the case of dense systems. Similar arguments hold for schemes for correcting the light scattering data for double scattering, as given for example by Dhont [44]. This author developed an iterative correction scheme and applied it to suspensions of colloidal silica and latex particles. In all cases, a q dependence of the diffusion coefficient remained after the correction for double scattering and was attributed to polydispersity and interparticle interaction effects, which requires *a priori* knowledge of these effects. However, the non-exponentiality and the q dependent relaxation rate associated with the interparticle interactions is exactly the information one wants to obtain from the dynamic light scattering experiments. To resolve this dilemma, comparison with an independent, multiple scattering-free technique is essential.

The reason for introducing CCDLS in addition to DXS here is twofold. First, since DXS operates at the limit of what is possible with modern synchrotron technology, it is certainly not a technique to be used for routine work, such as for example particle sizing. By contrast, a CCDLS setup is compact and easy to use in the laboratory. Secondly, CCDLS can be employed to extend photon correlation measurements to small wave vectors that are not accessible to DXS. In fact, in the following chapter it will become clear that only a combination of CCDLS, DXS and SAXS is powerful enough for the experiments on colloidal dynamics we have in mind.

3.3.2.1 CCDLS correlation functions

Figure 3.4 shows intensity correlation functions obtained with CCDLS at a scattering angle of 30°; since the single-scattering relaxation rate goes to zero as q^2 (see eq. 2.11), whereas the multiple-scattering relaxation rate is in first

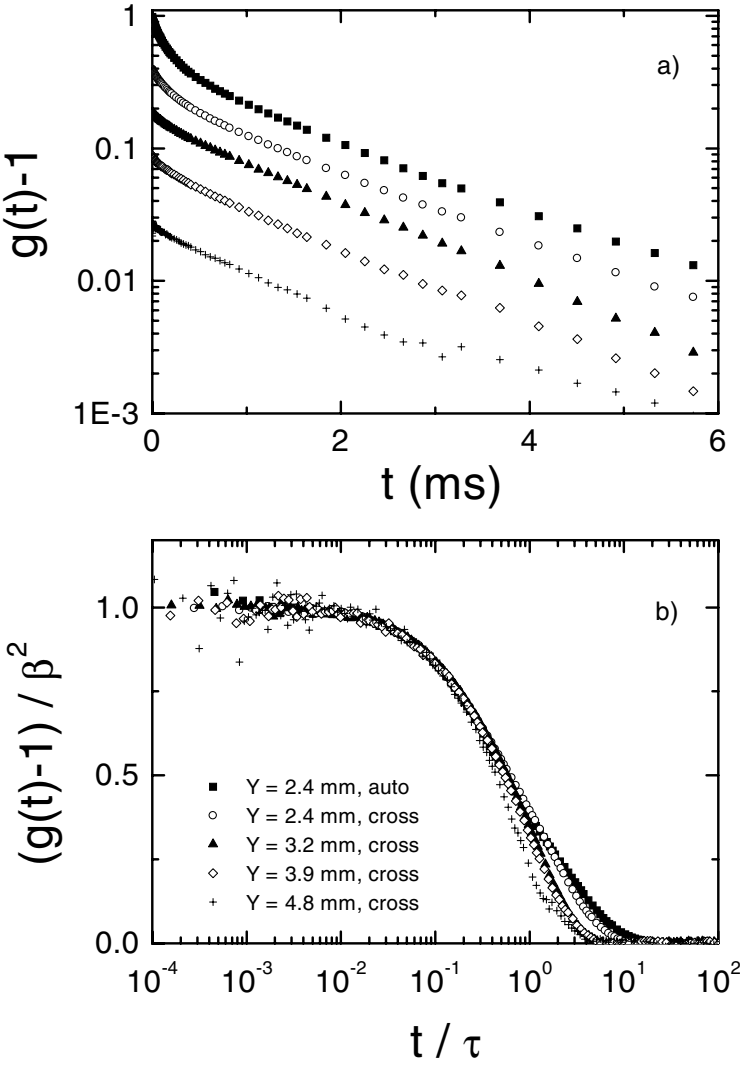

Figure 3.4: *(a) Dynamic light scattering intensity autocorrelation function (squares) and cross-correlation functions (circles, triangles, diamonds and crosses) for silica colloids in a mixture of ethanol and benzyl alcohol. The refractive index contrast is 1.063. The volume fraction of colloids is 0.078. The scattering angle* $\Theta = 30°$*. For the cross- correlation functions, the fiber separation increases from top to bottom. (b) Correlation functions shown in (a) normalized with their zero-time intercept* β^2*. The time axis in (b) is reduced with the initial decay time of the correlation functions.*

approximation independent of q, we expect the largest influence of multiple scattering at small scattering angles. The volume fraction is $\phi = 0.078$ and the refractive index contrast is $m_1/m_0 = 1.063$; this refractive index contrast is the second largest investigated in this study and is substantially larger than for the measurements to be reported in the following chapter. Figure 3.4(a) shows unnormalized correlation functions, fig. 3.4(b) normalized correlation functions. The squares are the autocorrelation function, the other symbols show cross-correlation functions with varying fiber distance as indicated in the figure. Several features are apparent from fig. 3.4(a). First, the amplitude of the autocorrelation function, $\beta^2 = 0.94$, is close to the ideal value of 1 [24], indicating a good performance of the setup. Secondly, the amplitude for cross-correlation is substantially smaller than for autocorrelation and drops strongly with increasing fiber distance; at the largest fiber distance of $Y = 4.8$ mm, $\beta^2 = 0.026$. This behavior is expected on the basis of the theory by Lock (see fig. 2.3). Thirdly, the correlation functions are non-exponential, the non-exponentiality being largest for the autocorrelation function. In cross-correlation, the non-exponentiality first decreases as the fiber distance is increased, but seems to remain almost constant for $Y \geq 3.2$ mm. In particular, the correlation function remains non-exponential even for the largest fiber distance. The non-exponentiality indicates that a distribution of relaxation rates rather than a single relaxation rate is present in the system. As discussed above, it is impossible to decide on the basis of the CCDLS measurements alone whether the remaining non- exponentiality at large fiber distances is due to interparticle interactions, which one is interested in, or due to residual contributions from multiple scattering. Fourthly, the initial decay of the correlation functions is less rapid for cross-correlation than for autocorrelation and the decay rate decreases with increasing fiber distance.

In fig. 3.4(b) we display normalized correlation functions, i.e., the correlation functions shown in fig. 3.4(a) divided by the amplitude. The time axis in fig. 3.4(b) is scaled by the initial decay time τ of the correlation functions, as obtained from the first cumulant [see fig 3.9(a)]. The scaling of the time axis eliminates the differences in the initial decay of the correlation functions, such that differences in the long-time behavior become more apparent. It is evident that multiple scattering contributions affect the long-time behavior as well as the initial decay.

The signal-to-noise ratio clearly becomes worse as the fiber distance is increased, which is a consequence of the dropping amplitude.

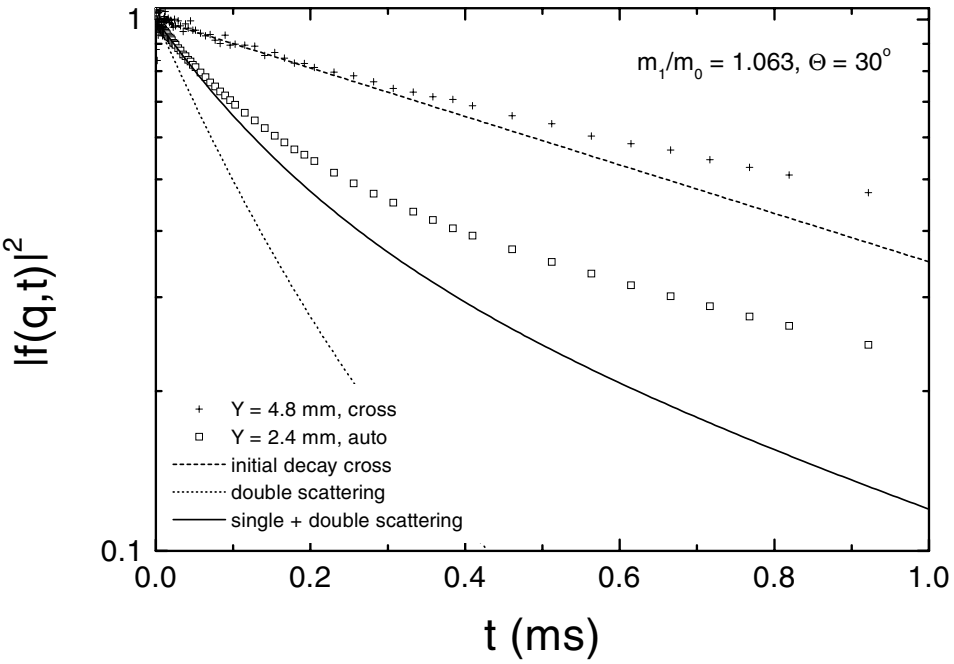

Figure 3.5: *Normalized dynamic light scattering intensity autocorrelation function (squares) and cross-correlation function (crosses) for silica colloids in an alcohol mixture (refractive index contrast 1.063, volume fraction 0.078, scattering angle 30°, fiber separation 4.8 mm for cross correlation). The dashed line represents the initial decay of the cross- correlation function. The dotted line represents the double-scattering intensity correlation function in the dilute limit. The solid line represents a mixture of double- and single scattering functions with a ratio of 1.3:1 at* $t = 0$.

In fig. 3.5 we compare some of the DLS correlation functions to calculations with the (dilute) theory given by Lock [20]. The purpose of this comparison is to estimate the importance of multiple scattering contributions. The squares show the autocorrelation function, the crosses the cross-correlation function at $Y = 4.8$ mm. The dashed line represents an exponential corresponding to the initial decay of the cross-correlation function. The dotted line shows the intensity correlation function for pure double scattering; it decays by a factor of about 7 faster than the cross-correlation function, indicating that multiple scattering has an enormous effect on the decay rate. In order to fit the initial decay of the measured autocorrelation function, we

have mixed double- and single scattering field correlation functions with a ratio of 1.3/1, taking the initial decay of the cross- correlation function as the single scattering limit. The solid line represents the square of the mixed field correlation function. Again it is seen that the correlation function becomes strongly non-exponential as a result of double scattering contributions. The reason is the fact that the decay rate of the double scattering correlation function is composed of contributions from different wave vectors q, leading to a distribution of decay rates in the mixed correlation function. The initial decay of the mixed correlation function is by about a factor of 4 faster than that of the cross-correlation function. It should be noted, however, that a comparison to the calculations by Lock can only give a rough idea about the role of multiple scattering for our systems, since it is a theory for the dilute limit.

3.3.2.2 Comparison with DXS

Figure 3.6 shows a direct comparison of normalized dynamic light scattering and dynamic x-ray scattering intensity correlation functions at identical scattering vectors. The sample is the same as that discussed above. The DXS results are compared to the DLS autocorrelation function and the DLS cross-correlation function at a fiber distance of 3.2 mm. The data are represented by lines instead of points in this figure for clarity. It is evident that the DLS autocorrelation function deviates substantially from the DXS result; the initial decay of the DLS autocorrelation function is more rapid than in the case of DXS. By contrast, the DLS cross-correlation function is practically identical to the correlation function obtained with x rays. This direct comparison demonstrates that the detection of multiply scattered light is indeed suppressed by the CCDLS technique. Note that the DLS cross-correlation function as well as the DXS correlation function are non-exponential. This observation shows that the non-exponentiality remaining as the fiber distance is increased, as discussed above, is not due to residual contributions from multiple scattering or to heterodyne detection, but results from interparticle interactions.

Figure 3.7 shows a direct comparison of normalized dynamic light scattering and dynamic x-ray scattering correlation functions for two other samples, one with a lower refractive index contrast than hitherto discussed [m_1/m_0 = 1.036, fig. 3.7(a)] and one with a larger contrast [m_1/m_0 = 1.077, fig. 3.7(b)]; the volume fraction is 0.078 as before. For the lower contrast, the

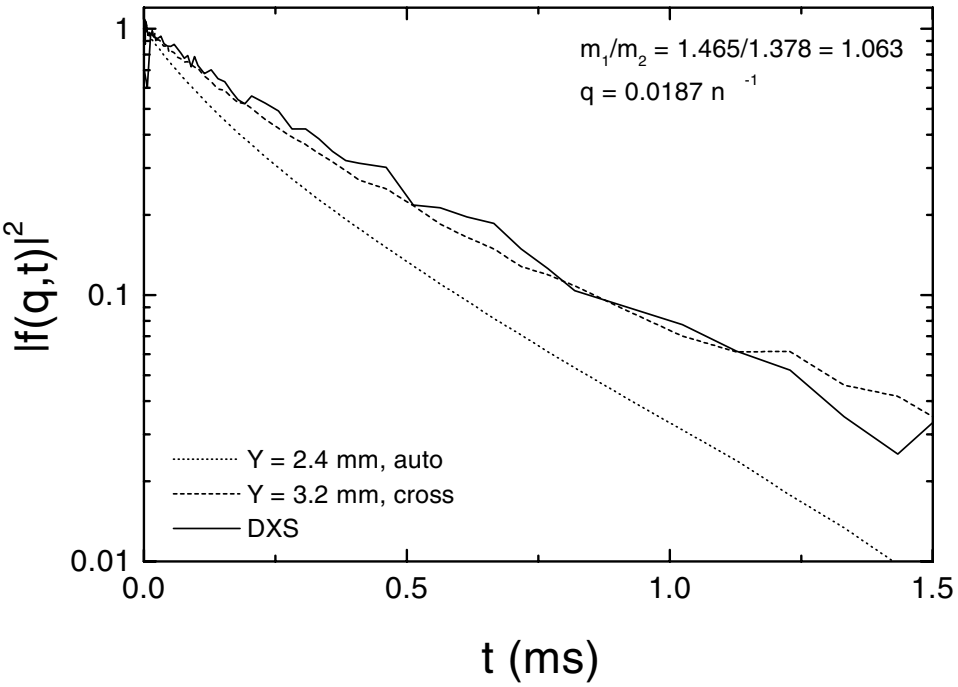

Figure 3.6: *Normalized intensity autocorrelation functions (solid line dynamic x-ray scattering, dotted line dynamic light scattering) and dynamic light scattering intensity cross- correlation function (dashed line) for silica colloids in an alcohol mixture (refractive index contrast 1.063, volume fraction 0.078). The scattering vector* $q = 0.0187\ nm^{-1}$.

DLS cross-correlation function agrees well with the DXS correlation function, whereas the autocorrelation function decays more rapidly. This behavior is expected on the basis of the previous discussion. For the larger refractive index contrast of 1.077, however, neither the DLS autocorrelation function nor the cross- correlation function agree with the DXS result, indicating that the limit of the present setup has been exceeded. The amplitude of the DLS intensity cross-correlation function corresponding to fig. 3.7(b) is only 0.014 at $Y = 4.8$ mm; it might have been possible to further reduce the contribution of multiple scattering to the correlation function by operating at an even larger fiber distance, but only at the cost of a forbiddingly small amplitude. In our setup, the field of view of the two detectors was limited by

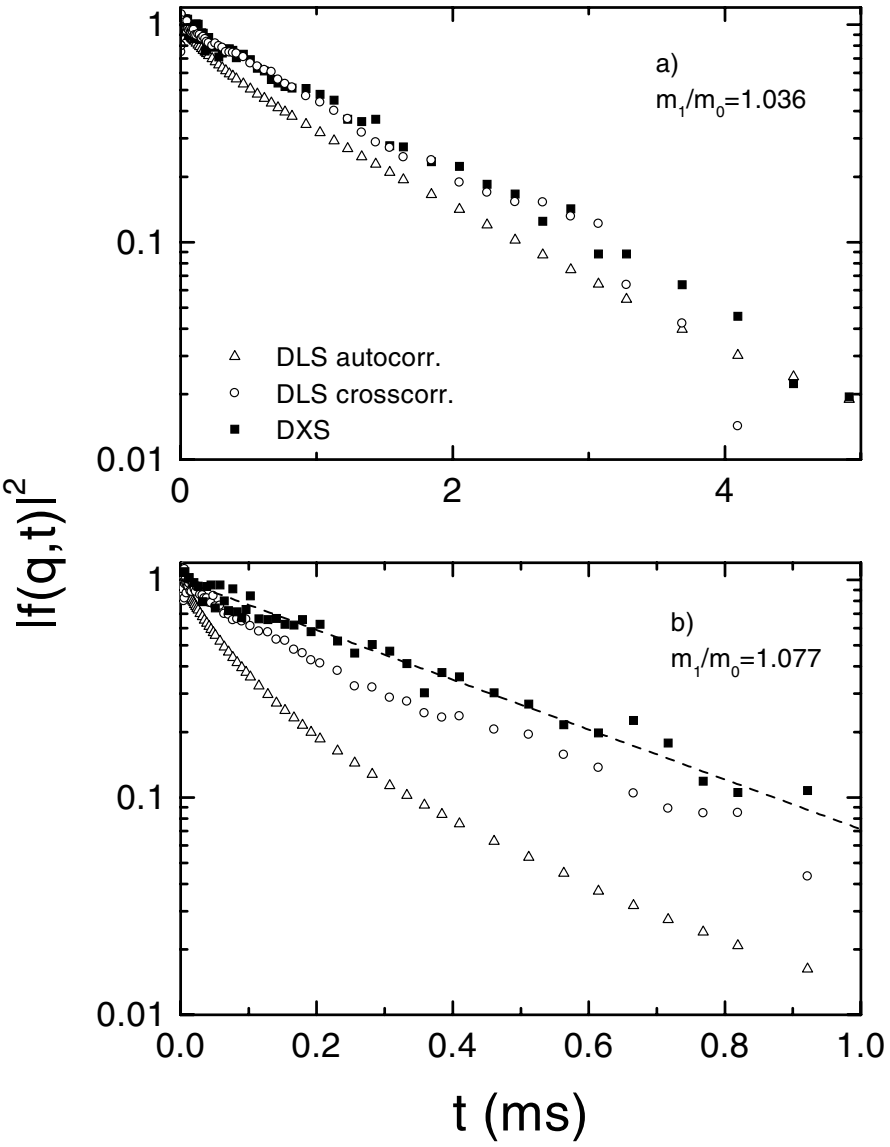

Figure 3.7: *Normalized intensity autocorrelation functions (squares dynamic x-ray scattering, triangles dynamic light scattering) and dynamic light scattering intensity cross- correlation function (circles) for silica colloids in an alcohol mixture (volume fraction 0.078). The refractive index contrasts are 1.036 (a) and 1.077 (b). The scattering vector* $q = 0.0114\ nm^{-1}$ *(a) and* $0.0184\ nm^{-1}$ *(b). The dashed line in (b) is a guide to the eye.*

the collection optics, in contrast to the setup of Meyer *et al.* [19], in order to avoid heterodyne detection; this is essential due to the small sample capillaries used. As the fiber distance increases, the overlap between the field of views of the two detectors will reduce; this effect will lead to a further reduction of the amplitude. It may be possible to reduce this problem by further optimizing the setup. However, for the present setup multiple scattering-free cross-correlation measurements within a reasonable averaging time cannot be performed anymore for this strongly scattering sample, showing the practical limits of the CCDLS technique. A simple calculation according to eq. 2.18 shows that $l_s/L \approx 0.05$ for the sample corresponding to fig. 3.7(b); at this point, it is seems to be necessary to resort to DXS alone to obtain q dependent experimental information with reasonable accuracy.

3.3.2.3 The initial decay

We now discuss the effect of multiple scattering on the initial decay rate of the intermediate scattering function, which we are eventually interested in to obtain the q dependent collective diffusion coefficient. Figures 3.8 and 3.9 display the initial relaxation rates, obtained from an exponential fit to the correlation functions at small times, for DLS autocorrelation, DLS cross-correlation and DXS. The refractive index contrasts corresponding to the data shown in figs. 3.8(a), 3.8(b), 3.9(a) and 3.9(b) are 1.017, 1.036, 1.063 and 1.077, respectively. The volume fraction is 0.078 for all samples. The data are plotted against q^2, since in a dilute sample the diffusion coefficient is independent of scattering vector and thus $\tau^{-1} \propto q^2$ for single scattering. It is seen from fig. 3.8(a) that for the lowest refractive index contrast, the DLS relaxation rates are practically independent of fiber distance and are the same for auto- and cross-correlation. Reasonable agreement with the DXS results is found for all DLS measurements, indicating that multiple scattering does not play an important role for this sample. A calculation shows that $l_s/L = 1$ for this sample, i.e., multiple scattering is indeed expected to be of minor importance. The data do not follow a straight line through the origin, which again indicates that interparticle interactions play a role. Without direct comparison with DXS it would be impossible to unambiguously attribute the apparent deviation of the relaxation rates from a pure q^2 dependence to interparticle interactions; there is thus no intrinsic way of assessing the reliability of the cross-correlation technique.

Figure 3.8(b) shows relaxation rates for a sample with a refractive index

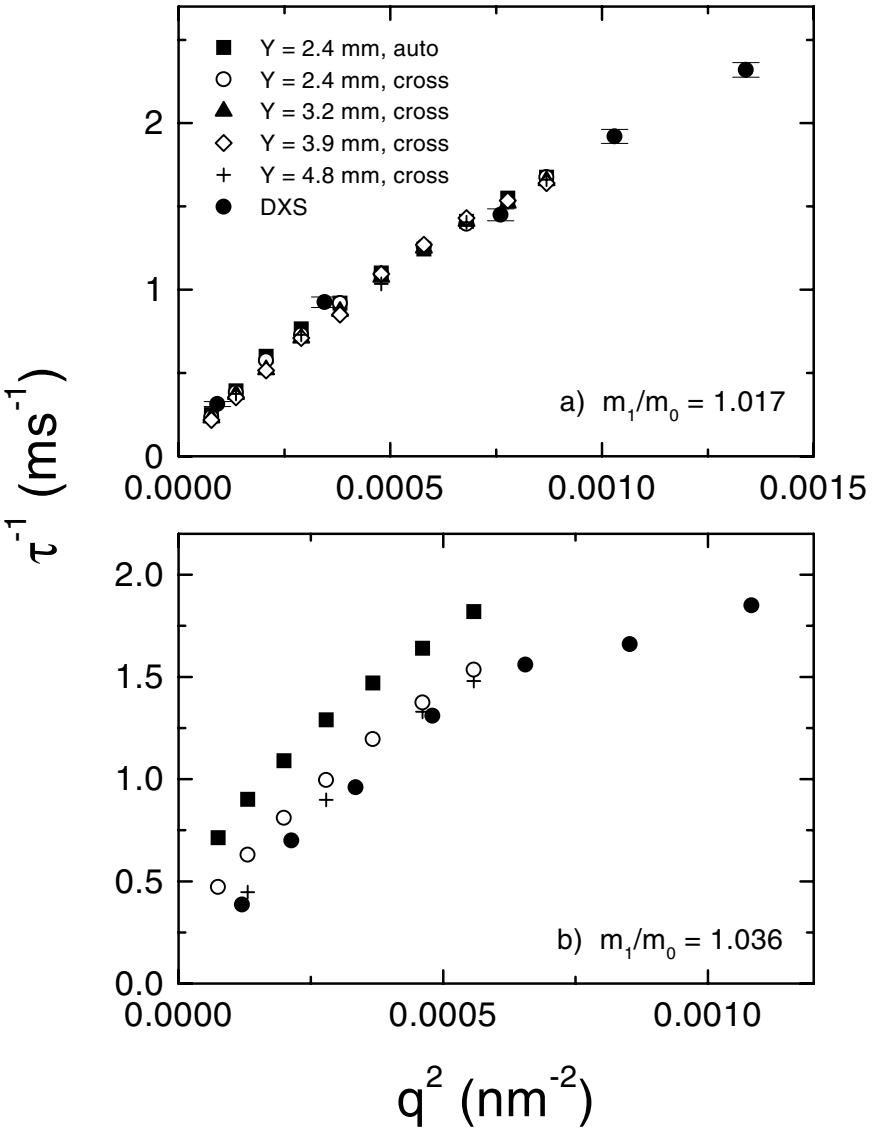

Figure 3.8: *Initial decay rates of intermediate scattering functions for silica colloids in mixtures of ethanol and benzyl alcohol (volume fraction 0.078). The refractive index contrasts are 1.017 (a) and 1.036 (b). The relaxation rates have been obtained from DLS autocorrelation (squares), DXS (bullets) and DLS cross- correlation (circles fiber distance 2.4 mm, triangles 3.2 mm, diamonds 3.9 mm and crosses 4.8 mm).*

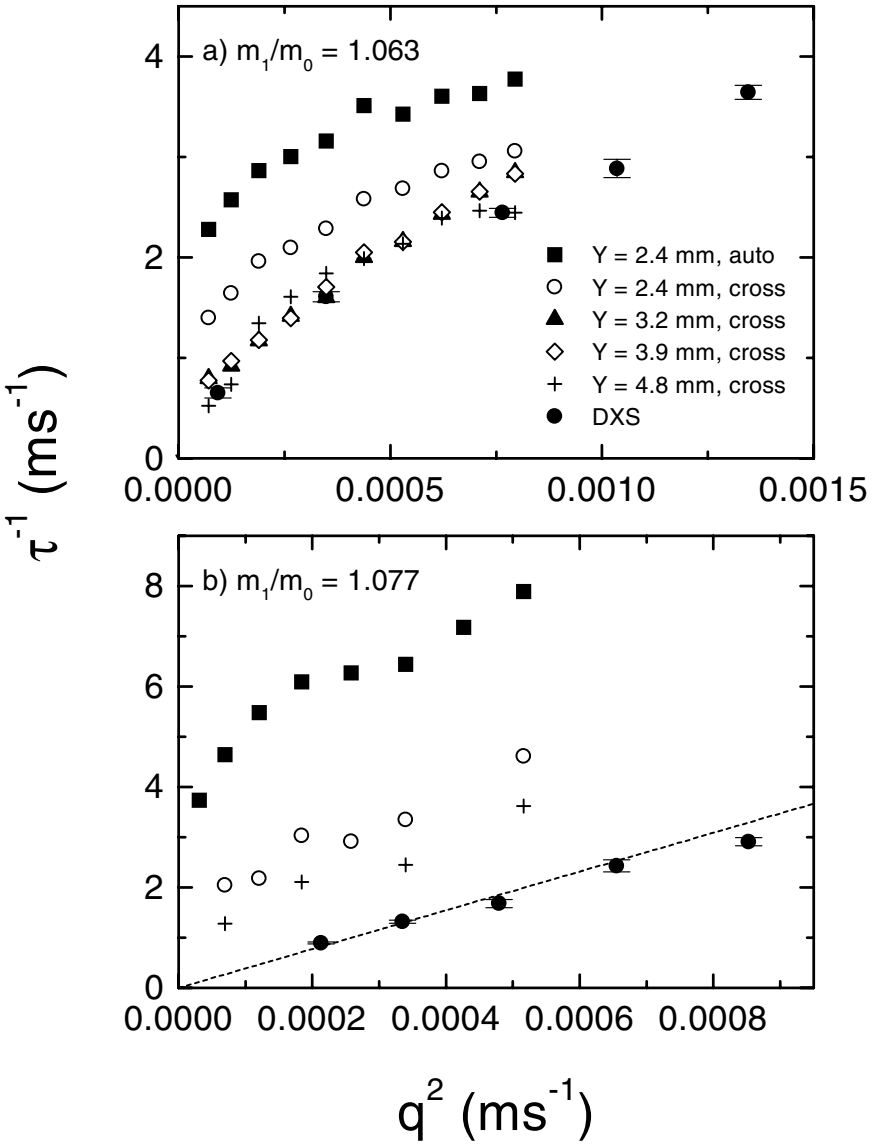

Figure 3.9: *Initial decay rates of intermediate scattering functions for silica colloids in mixtures of ethanol and benzyl alcohol (volume fraction 0.078). The refractive index contrasts are 1.063 (a) and 1.077 (b). The relaxation rates have been obtained from DLS autocorrelation (squares), DXS (bullets) and DLS cross- correlation (circles fiber distance 2.4 mm, triangles 3.2 mm, diamonds 3.9 mm and crosses 4.8 mm). The dashed line in (b) represents the dilute limit,* $1/\tau = D_0 q^2$.

contrast of $m_1/m_0 = 1.036$. The DLS autocorrelation data now deviate appreciably from the DXS results as far as the absolute value is concerned. The curvature of the plot remains similar, i.e., multiple scattering basically leads to an additional offset in the data. This is expected, since the multiple scattering relaxation rate is approximately independent of the scattering angle [45]. We note, however, that because of the appreciable deviation of the data from a pure q^2 dependence, it would be difficult to extrapolate the DLS data to $q = 0$, to obtain the offset, and thus correct the results for multiple scattering. Cross-correlation greatly reduces the discrepancy with the DXS data. At a fiber distance of 4.8 mm, the cross-correlation data agree to within 5 % with the DXS results, demonstrating that the detection of multiply scattered light is suppressed efficiently.

As the refractive index contrast is increased further, the discrepancy between the DLS autocorrelation results and the DXS data becomes larger, as can be seen from fig. 3.9(a) [$m_1/m_0 = 1.063$]. At the smallest scattering angle of 30°, the DLS relaxation rate is larger than the DXS relaxation rate by about a factor 4. Cross-correlation again greatly reduces this discrepancy. For a fiber distance of $Y = 4.8$ mm, the CCDLS data agree reasonably well with the x-ray data in the whole q range. However, the cross-correlation amplitude is typically only 2 % for this sample at the largest fiber distance, requiring averaging times of about 0.5 h to obtain a reasonable signal-to-noise ratio. For this sample, we find $l_s/L \approx 0.08$, which seems to be close to the practical limit of the current setup considering the small cross-correlation amplitudes.

Figure 3.9(b) shows relaxation rates at a refractive index contrast of 1.077. In this case, the silica particles were suspended in pure ethanol (volume fraction 0.078 as before). Since the viscosity of ethanol is well known, we can estimate the diffusion coefficient D_0 in the dilute limit from the Stokes-Einstein relation; the dashed line in fig. 3.9(b) represents the relation $\tau^{-1} = D_0 q^2$. The DXS data are close to the dilute limit for this sample. The DLS autocorrelation relaxation rates, on the other hand, are about one order of magnitude larger than the DXS relaxation rates, indicating that multiple scattering has now become dominant. Although cross-correlation again greatly reduces the discrepancy between DLS and DXS, there remains a large difference even for the largest fiber distance; obviously, the limits of the present CCDLS setup have been exceeded with this sample. To elucidate this point, we show the DLS autocorrelation function at 30° at short times in fig. 3.10. The dashed line represents the dilute single scattering limit. It is evident that

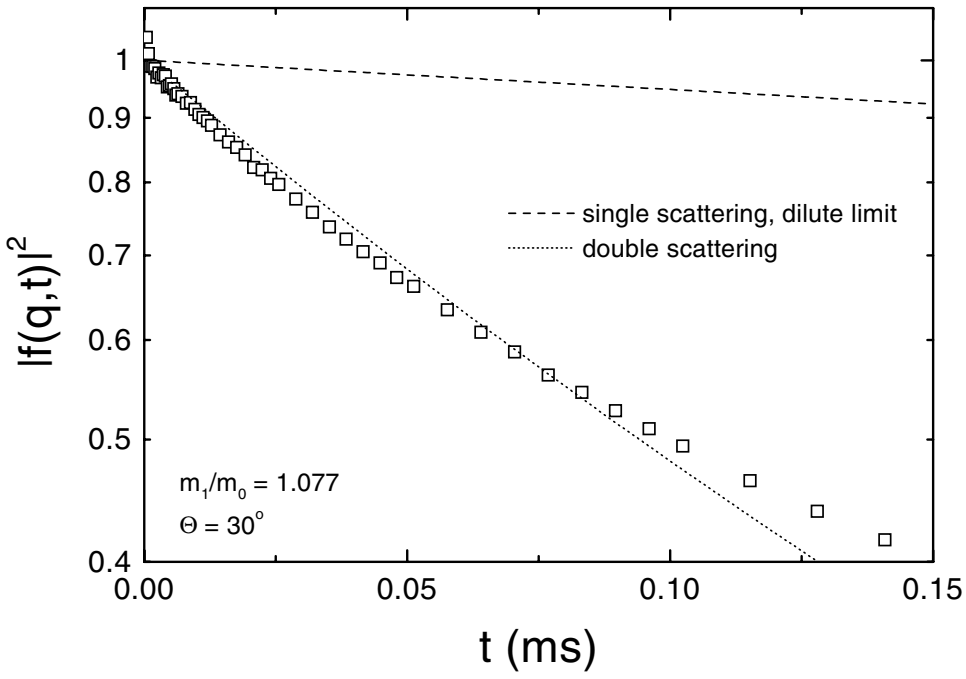

Figure 3.10: *Normalized dynamic light scattering intensity autocorrelation function (squares) for silica colloids in ethanol (refractive index contrast 1.077, volume fraction 0.078, scattering angle 30°). The dashed line represents the single scattering, dilute limit. The dotted line represents the double-scattering intensity correlation function in the dilute limit.*

the autocorrelation function decays much faster than this limit. The dotted line shows the intensity correlation function for pure double scattering in the dilute limit, as calculated according to Lock's theoretical expressions. At very short times, the measured autocorrelation function decays even faster than expected for pure double scattering; this could be due to either particle correlations, which are not included in the theory of Lock, or it may be an indication that higher order scattering has become important. An indication that higher order scattering plays a role also comes from the q dependence of the autocorrelation relaxation rates [fig. 3.9(b)], that differs significantly from the behavior of the samples with smaller refractive index contrasts. It is clear that multiple scattering strongly dominates over single scattering for this sample and, therefore, CCDLS is not capable anymore of sufficiently

suppressing the multiple scattering contributions.

3.4 Conclusions and outlook

In this chapter, we have demonstrated by a direct comparison of cross-correlated dynamic light scattering with DXS that CCDLS suppresses the detection of multiply scattered light. We found our present CCDLS setup to be effective up to a nominal ratio of the scattering mean free path to the sample size of $l_s/L \approx 0.08$. An analysis in terms of the theoretical treatment by Lock [20] shows that at small angles, the ratio of the contribution of doubly scattered light to the electric field correlation function to the contribution of singly scattered light should be about 1/1 in this case. For samples that are even more strongly scattering, CCDLS fails and one has to resort to DXS alone. By using DXS as an independent reference, we have overcome the intrinsic dilemma of previous attempts to suppress multiple scattering detection or to correct correlation functions for multiple scattering: in order to assess the quality of these methods, one needs to have information on interparticle interactions beforehand, which is however precisely the kind of information one would like to obtain from DLS experiments. With the experiments presented in this chapter we have established the potential of a new combination of experimental techniques that is free from multiple scattering effects: CCDLS, DXS and SAXS. In the following chapter, we will apply this combination to investigate the dynamics of charge stabilized colloidal suspensions

4

Dynamics of charged colloids probed by coherent x rays

We investigate the hydrodynamic interaction in suspensions of charged colloidal silica spheres. The volume fraction as well as the range of the electrostatic repulsion (the direct interaction) between the spheres is varied. Using a combination of dynamic x-ray scattering, cross-correlated dynamic light scattering and small- angle x-ray scattering, the hydrodynamic function $H(q)$ is determined experimentally. The effective hydrodynamic interactions appear to be screened, if the range of the direct interaction is relatively long and the static density correlations are strong. The observation of apparent hydrodynamic screening is in marked contrast to hard-sphere-like systems.

4.1 Introduction

Colloidal suspensions have intriguing static and dynamic properties due to their composite nature and the mesoscopic length scales involved [1]. Colloids interact by direct forces, such as electrostatic or hard-sphere repulsions, and hydrodynamic forces mediated by the suspending fluid [3, 9]. Whereas the static properties of colloidal suspensions are strikingly similar to those of molecular fluids, the important role of the suspending medium leads to significant differences in the dynamical behavior. The complex viscoelastic and diffusional properties of colloidal suspensions depend on the interplay between direct and hydrodynamic interactions. This interplay is governed

by the ratio of the different length scales in the system [46], such as particle radius, interparticle distance, and the range of the interactions. Understanding the macroscopic effects of the mesoscopic forces acting on the colloidal level is challenging from a fundamental point of view and allows to tailor the characteristics of colloidal suspensions for technological applications [2]. However, the theoretical treatment of colloidal dynamics has proven to be an exceptionally involved problem. The difficulty arises mainly from the long-range, many-body nature of hydrodynamic interactions: the hydrodynamic interaction between two isolated particles decays with the inverse of the interparticle distance [3, 9]. As a consequence of these long-range, many-body properties, it is impossible to treat hydrodynamic interactions exactly in the case of concentrated suspensions. Instead, one has to resort to approximating the hydrodynamic interactions by some effective pair interaction. For the most simple form of the *direct* interaction, the hard-sphere repulsion, it has been possible to incorporate many-body effects in the effective *hydrodynamic* pair interaction in an approximate way [47]. It was found that hydrodynamic interactions in hard-sphere-like systems always lead to a hindrance of diffusion as compared to dilute systems. This hydrodynamic hindrance of diffusion is due to two physical mechanisms: the cumulative backflow of displaced fluid, hindering the motion of particles in the same direction, and near-field hydrodynamic interactions (so-called lubrication forces) [48, 49, 50].

Many colloidal systems, such as silica or polystyrene particles, do not interact by a simple hard-sphere-like repulsion, but by additional electrostatic interactions. These electrostatic interactions arise from the dissociation of surface groups, leading to a finite charge density on the particle surface [1]. The resulting Coulomb interaction between the particles is screened by counterions and excess salt in the suspending liquid, leading to a Yukawa-like effective interaction. These systems are called "charge stabilized", due to the fact that the electrostatic repulsion between the particles stabilizes the suspension against aggregation. About a decade ago, experiments indicated that the hydrodynamic interaction in charge stabilized colloidal suspensions behaves qualitatively differently from the hard-sphere case: hydrodynamic interactions were found to enhance diffusion at around the peak position of the static structure factor [51]. This finding was confirmed in more recent experiments [52, 53]. As a consequence, attention was drawn to the possible influence of the direct interaction on the hydrodynamic interaction [43, 46].

The above mentioned experiments and our previous results [15] indicate that the qualitative behavior of the hydrodynamic interaction is sensitive to

the direct interaction. An interesting fundamental question in this context is, for instance, whether many-body effects can result in screening of the bare hydrodynamic interaction, leading to an *effective* hydrodynamic pair interaction that is no longer long-range [54]. The concept of hydrodynamic screening occurs in many different contexts. For instance, hydrodynamic screening is vigorously being discussed in connection with sedimentation [7, 55], where it has been invoked to remedy the problem of diverging velocity fluctuations. Screening of the hydrodynamic velocity field also occurs in porous media, where the solid frame remains fixed [56]. A phenomenologically similar effect is known from polymers [57] and polyelectrolyte solutions [58]. Multiple scattering- and effective medium calculations have shown that hydrodynamic screening is present in stationary suspensions of hard spheres, where the velocity of each of the particles vanishes on average [59]. Recently, it has been shown theoretically that hydrodynamic interactions are partially screened for particles on a lattice [60]. A hydrodynamic screening mechanism introduces a well defined length scale for the range of the effective two-particle hydrodynamic interaction, mathematically similar to the electrostatic screening length for the direct interaction.

The most successful theory for the hydrodynamic interactions in dense colloidal suspensions to date, known as the fluctuation expansion, has been developed by Beenakker and Mazur [47]. Their approximate many-body theory does not involve screening. The theory has been confirmed in the case of hard-sphere-like colloids [61, 62, 63] and has also been applied successfully to slightly charged colloids at moderate volume fractions [64]. Later, Nägele and coworkers developed a more simple, pair-wise additive (PA) theory [9], in which hydrodynamic interactions are also unscreened. The PA theory is adequate at low [53] to moderate volume fractions [9]. In the PA theory, an increase of the range of the direct interaction merely leads to an increase of the average interparticle separation, with the consequence that far-field hydrodynamic effects become more important. The work on charged colloidal suspensions has been reviewed by Nägele [9]. As he points out [9, 65], many-body hydrodynamic effects become noticeable at volume fractions above about 10 % and one has to resort to the elaborate fluctuation expansion in this concentration regime. However, the theory of Beenakker and Mazur is a hard-sphere theory and does thus in principle not allow any predictions about the behavior of concentrated charged systems, where the direct interaction plays an important role.

To date, there are very few experimental data on concentrated charged

colloidal suspensions [51], which we address in this thesis. The paucity of experiments is in part due to the problems encountered with conventional light scattering techniques, in particular multiple scattering. In order to avoid multiple light scattering at high volume fractions it is necessary to match the refractive indices of the colloidal particles and the suspending medium. This, however, strongly restricts the freedom to change the direct interaction [15].

In this chapter, we report on a comprehensive study of the effective hydrodynamic interactions in concentrated charge stabilized colloidal suspensions. We perform a combination of dynamic x-ray scattering (DXS), cross-correlated dynamic light scattering (CCDLS) and small angle x-ray scattering (SAXS) measurements on suspensions of colloidal silica spheres. These new experimental techniques are free from multiple scattering, overcoming the restrictions mentioned above. Thus, the collective diffusion coefficient and the structure factor are obtained over a wide range of wave vectors. The range and strength of the electrostatic repulsion between the particles is varied. We observe a strong influence of the structure on the effective hydrodynamic interactions. For samples with relatively short-range direct interactions and weak spatial correlations in the particle density, as quantified by the static structure factor, the data agree reasonably well with the fluctuation expansion [47]. As the range of the direct interaction increases and static density correlations become stronger, however, we find large deviations from this theory. In particular, the wave-vector dependence of the data becomes substantially less pronounced than expected. Phenomenologically, this flattening of the hydrodynamic function can be described as hydrodynamic screening.

4.2 Theory

In this section, we briefly summarize well known theoretical results on the dynamics of colloidal suspensions [9, 43], in order to introduce the quantities we are concerned with in this chapter.

The dynamical properties of colloidal suspensions are characterized by the dynamic structure factor $S(q,t)$ (see chapter 2). For times large compared to the typical relaxation time for the momentum of the colloidal particles, $\tau_B \approx 10^{-8}s$, the dynamics is governed by the generalized Smoluchowski equation

[9], leading to

$$\frac{dS(q,t)}{dt} = -q^2 D(q) S(q,t) + \int_0^t du M(q,t-u) \frac{S(q,u)}{S(q)}. \tag{4.1}$$

Here, $D(q)$ is the effective short-time collective diffusion coefficient, $M(q,t)$ the memory function, and $S(q) = S(q,0)$ the static structure factor. The memory function describes dynamical interaction effects that, on the (slow) time scale of colloidal diffusion, do not act instantaneously. Equation 4.1 may be solved by Laplace transform to give

$$\tilde{S}(q,z) = \frac{S(q)}{z + q^2 \tilde{D}(q,z)}, \tag{4.2}$$

where z is the transform variable. The collective diffusion kernel $\tilde{D}(q,z)$ is given by

$$\tilde{D}(q,z) = D(q) - \frac{\tilde{M}(q,z)}{q^2 S(q)}. \tag{4.3}$$

Equation 4.3 may be cast into the form of a generalized Stockes-Einstein relation, that is,

$$\tilde{D}(q,z) = \frac{k_B T}{S(q)} \frac{1}{\tilde{\xi}(q,z)}, \tag{4.4}$$

where k_B is Boltzmann's constant. The function $\tilde{\xi}(q,z)$ is a wave vector- and frequency dependent friction coefficient. The friction coefficient characterizes the visco-elastic properties of the suspension. In the dilute limit, with no interparticle interactions present, $\tilde{\xi}(q,z)$ reduces to the well-known Stokes-Einstein friction coefficient $\xi_0 = 6\pi\eta a$. Here, η is the viscosity of the suspending fluid and a the particle radius.

It follows from eq. 4.1 that the decay of $S(q,t)$ at short times is approximately exponential, with a decay rate $\Gamma_1(q) = -q^2 D(q)$. Here, the term "short time" refers to the regime $\tau_B \ll t \ll \tau_a$, where $\tau_a \approx 10^{-3} s$ is the structural relaxation time. The short-time regime is characterized by the requirement that the particles do not move appreciably on the length scale of the particle radius. This requirement is fulfilled for $t \ll \tau_a = a^2/D_0$, where $D_0 = k_B T/\xi_0$. At short times, a particle will move within a basically static cage of neighboring particles. For $t > \tau_a$, the cage will break up and a particle will experience the visco-elastic response of the surrounding complex fluid. Memory effects become noticeable at long times, which in the

case of colloidal suspensions generally leads to a slower decay of the dynamic structure factor than at short times. As a result, the overall shape of $S(q,t)$ is non-exponential. The non-exponentiality of the dynamic structure factor may be characterized by the non-exponentiality factor $\Delta(q)$, which is given by [43]

$$\Delta(q) = \frac{\tilde{M}(q,0)}{q^2 D_0 H(q)} = 1 - \frac{\tau(q)}{\bar{\tau}(q)}, \tag{4.5}$$

where $\tau(q) = 1/\Gamma_1(q)$ is the initial decay time and $\bar{\tau}(q)$ the average relaxation time of the dynamic structure factor. The function $H(q)$ represents the hydrodynamic interactions (see below). The average relaxation time involves a time integral over the dynamic structure factor [43]; it is therefore difficult to determine experimentally.

In this thesis, we will concentrate on the short-time dynamics. The reason for this restriction is threefold. First, the relation between the first cumulant of intensity correlation functions and the short-time dynamics is well established theoretically, and the first cumulant can be determined accurately by experiments. Secondly, the short-time behavior must be known and understood for an interpretation of the full shape of the correlation functions [9]. Thirdly and most importantly, the short-time dynamics has hitherto hardly been investigated in the case of dense, charge stabilized suspensions.

The short-time diffusion coefficient depends on the static and hydrodynamic interparticle interactions. It can be shown [3] that $D(q)$ is given by

$$D(q) = D_0 \frac{H(q)}{S(q)}. \tag{4.6}$$

Relatively simple physical interpretations of $D(q)$ are possible in the $q \to 0$ and $q \to \infty$ limits, which is why much theoretical work has concentrated on these regimes. For $q = 0$, all particles move collectively in the same direction. This movement is driven by the osmotic compressibility [$\propto S(0)$] of the system. The hydrodynamic effects on colloidal motion in the $q = 0$ limit are determined by the sedimentation coefficient, which is identical to $H(q = 0)$ [49]. The $q = \infty$ limit of eq. 4.6, on the other hand, gives the short-time self-diffusion coefficient D_s, which characterizes the motion of a single particle. In the case of hard spheres, D_s/D_0 is determined only by the passive hydrodynamic hindrance of neighboring particles [48]. Apart from the $q = 0$ and $q = \infty$ limits, it can be instructive to consider the dynamics at the location of the peak of the static structure factor, $q = q_m$ [66]; q_m obviously

defines a characteristic structural length scale of the system. According to eq. 4.6, $D(q)$ is reduced in the peak of the static structure factor; this expresses the initial "caging" of the particles.

The hydrodynamic function $H(q)$ is connected to the many-body mobility tensors $\mu_{ij}(\mathbf{R}^N)$ by

$$H(q) = \frac{k_B T}{q^2 N D_0} \sum_{i,j=1}^{N} \langle \mathbf{q} \cdot \mu_{ij}(\mathbf{R}^N) \cdot \mathbf{q} e^{i\mathbf{q}\cdot(\mathbf{R}_i - \mathbf{R}_j)} \rangle, \tag{4.7}$$

where $\mathbf{R}^N$ denotes the spatial configuration of N particles. Physically, the mobility tensors relate the velocity $\mathbf{v}_i$ of a particle to the forces $\mathbf{F}_j$ exerted on each of the particles by the surrounding fluid:

$$\mathbf{v}_i = -\sum_{j=1}^{N} \mu_{ij}(\mathbf{R}^N)\mathbf{F}_j. \tag{4.8}$$

In the case of a single particle, eq. 4.8 reduces to the expression for the Stokes friction force, $\mathbf{F}_i = -6\pi\eta a \mathbf{v}_i$. In general, the hydrodynamic function cannot be calculated exactly, since the mobility tensors depend on the configuration of all N particles and, consequently, eq. 4.7 contains many-particle correlations. In order to render the problem tractable, the mobility tensors must be approximated by an effective pair mobility that depends only on the relative distance of two particles.

In the hard-sphere theory of Beenakker and Mazur [47], the effective pair mobility is, to a good approximation, given by

$$\mu_{ij}^{eff} = \mu^* \Big(\mathbf{1}\delta_{ij} + (1-\delta_{ij}) \{ \frac{3}{4}\frac{a}{R} [\mathbf{1} + \frac{\mathbf{RR}}{R^2}] + \frac{1}{2}(\frac{a}{R})^3 [\mathbf{1} - 3\frac{\mathbf{RR}}{R^2}] \} \Big). \tag{4.9}$$

Here, $R = |\mathbf{R}_i - \mathbf{R}_j|$ is the interparticle distance. The second term on the right hand side of eq. 4.9 contains the long-range Oseen tensor ($\propto 1/R$) and the dipole contribution ($\propto 1/R^3$). The Oseen tensor is the Greens function of the stationary, linearized (low Reynolds number) Navier Stokes equation, i.e., it describes the hydrodynamic velocity field arising from a point force in an infinite incompressible fluid medium. It is in that sense analogous to the monopole part of an electrostatic charge distribution. The effective pair mobility 4.9 is *unscreened*, that is, the dominant two-particle term decays as $1/R$, as in the dilute limit. For hard spheres, the prefactor μ^* is equal to $1/6\pi\eta^* a$, where η^* is to linear order in the volume fraction identical to the effective viscosity of the suspension [47].

Equation 4.9 has a simple physical interpretation: particles in a hard-sphere colloidal suspension interact via an *effective* homogeneous medium of viscosity η^*, replacing the pure suspending fluid. The functional dependence of the effective hydrodynamic interaction on the interparticle distance remains unchanged as compared to the dilute case. Naturally, the question arises whether this picture will remain valid if the range and strength of the *direct* interactions differs substantially from the simple hard-sphere repulsion.

4.3 Experimental

Concentrated master suspensions of silica colloids in mixtures of deionized water and 50 wt% glycerol (Aldrich, 99.5+%, spectrophotometric grade) or in an optically index matching mixture of ethanol and benzyl alcohol were produced by centrifugation. Samples of lower concentrations were obtained by dilution with known amounts of fluid; for details concerning the sample preparation and characterization see section 2.4.

Silica suspensions are charge stabilized [3]. The range and strength of the electrostatic repulsion between the particles depends on the concentration of counterions and excess salt in the fluid [1]. We produced three series of samples, one in an index matching mixture of ethanol and benzyl alcohol (volume fraction $0.078 \leq \phi \leq 0.311$), and two series in water/glycerol ($0.03 \leq \phi \leq 0.149$). We also prepared suspensions in ethanol/benzyl alcohol at volume fractions of $\phi = 0.363$ and 0.415 and found these samples to have solidified. The solidification was detected by the appearance of a non-decaying long time tail in the intensity autocorrelation function [67] as well as by the observation of static x-ray speckle in the SAXS experiments. The two series in water/glycerol were prepared using the same master suspension, ensuring that they had exactly the same volume fractions. In one of the water/glycerol series, excess salt was removed by deionizing with ion exchange resin (Bio Rad AG 501-X8) and adding extra exchange resin to the samples, thus increasing the range and strength of the direct interaction. The other series of samples remained non-deionized. Thus it was ensured that the two series in water/glycerol differed only in salt concentration but were otherwise identical; this allowed to selectively study the influence of the direct interaction on the dynamics.

The refractive index of the water-glycerol mixture ($m = 1.396$) differs from that of the colloidal particles, leading to substantial multiple scatter-

ing in the *visible*. Therefore, standard light scattering techniques are not suited to investigate the water/glycerol samples [15]. We overcome this limitation by using a combination of dynamic x-ray scattering, cross-correlated dynamic light scattering, and small-angle x-ray scattering. This is the only combination of experimental techniques that allows us to obtain *static and dynamic* information over a wide q range, free from multiple scattering. The experimental setups used are described in detail in sections 2.2.4 and 2.2.5.

4.4 Results

4.4.1 Structure

We will first discuss the static small angle x-ray scattering results, giving the static structure factor $S(q)$. The structure factor is needed to eventually obtain the hydrodynamic function $H(q)$ (eq. 4.6). $S(q)$ characterizes the degree of static correlations in the particle number density and gives thus information on the direct interaction between the colloids.

Figure 4.1 shows static small angle x-ray scattering measurements on two deionized suspensions ($\phi = 0.050 \pm 0.001$ and 0.149 ± 0.003) and the particle form factor $P(q)$. Typically, the signal from the scintillation counter was averaged over 20 s per point, for 80 points in the interval $0.005 \leq q \leq 0.15$ nm^{-1}. The data are scaled in such a way that all three curves coincide at large wave vectors. The form factor was measured on a dilute non-deionized sample ($\phi \approx 0.005$), as discussed in chapter 2. The form- factor points shown in fig. 4.1 at wave vectors larger than the position of the first minimum were obtained from a fit to the original data (see fig. 2.10). The fitted values of $P(q)$ are used here at large q to increase the accuracy of the structure factors, which are obtained by dividing the scattered intensity by the form factor. Concerning the q dependence of the data, it is seen from fig. 4.1 that the scattered x-ray intensity of the concentrated samples has a pronounced main peak at a well defined wave vector q_m, oscillates around the form factor at $q > q_m$, and eventually coincides with the form factor at large q.

From the data in fig. 4.1 the structure factor is obtained according to eq. 2.13. The scaling of the data ensures that $S(q) = 1$ at large q. This normalization of the structure factor is possible due to the large q range accessible to SAXS. The large q range and the fact that multiple scattering does not play a role for x rays make SAXS an ideal tool for determining

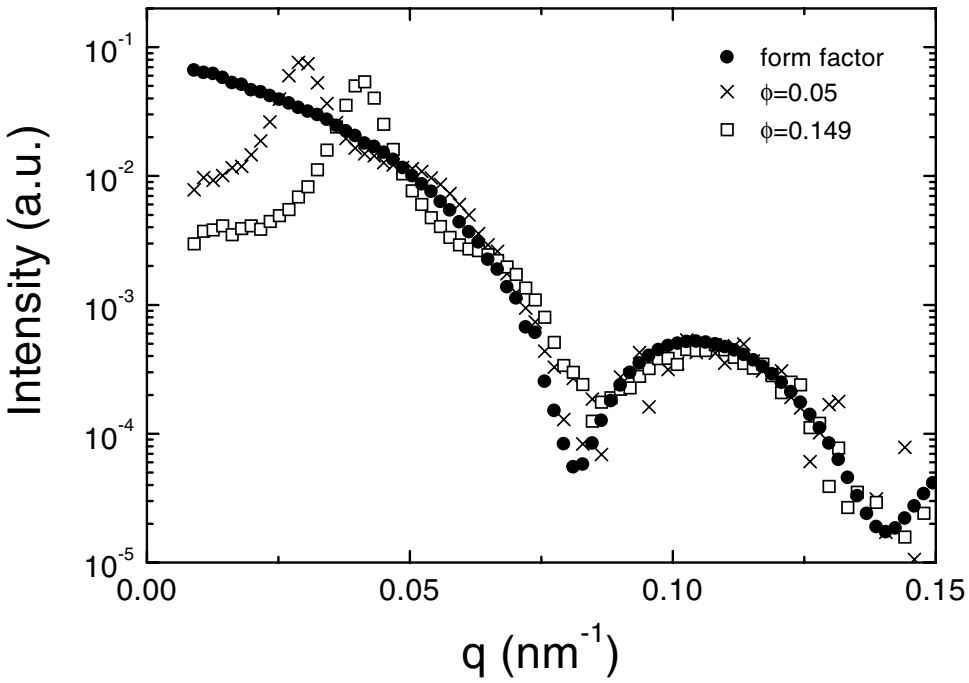

Figure 4.1: *Static scattered x-ray intensity for silica colloids in a deionized mixture of water and glycerol. The volume fractions are 0.05 (crosses) and 0.149 (squares). The form factor (circles) was measured on a dilute non-deionized sample. The curves are scaled to coincide at large wave vectors.*

the structure factors of non-index matched colloidal suspensions and crystals [68].

In fig. 4.2 the structure factor is shown for a non-deionized and a deionized suspension at the same volume fraction of $\phi = 0.05$. It is evident from fig. 4.2 that deionizing the samples leads to an increase of the peak height of $S(q)$, a decrease of the osmotic compressibility [$\chi_T \propto S(q = 0)$], and a shift of the peak to smaller q values. The shift of the peak indicates an increase of the *effective* radius of the particles, which is a measure for the range of the direct interaction [46]. The strong increase of the peak height demonstrates that liquid-like ordering is much more pronounced in the deionized samples [69].

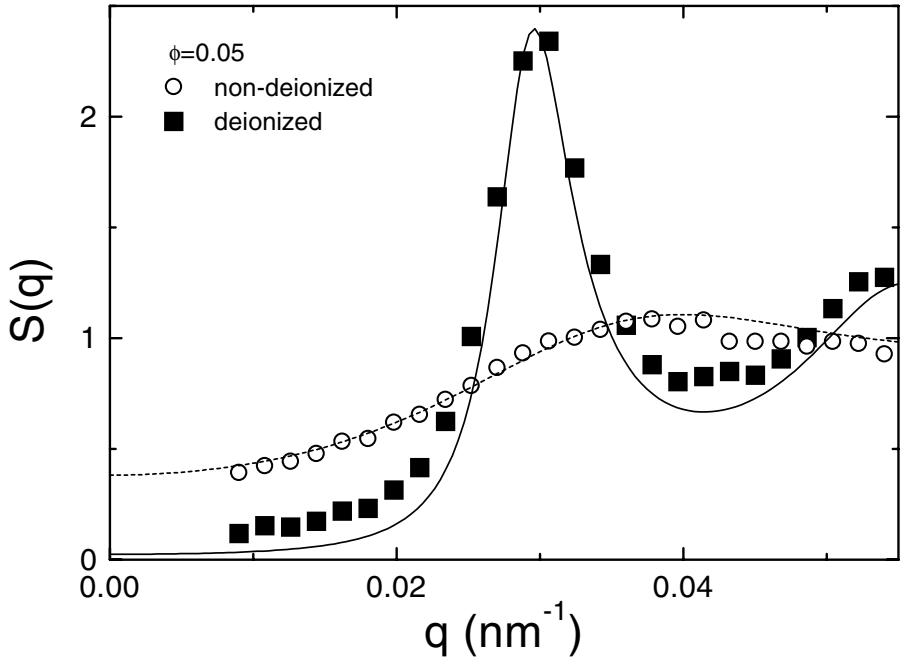

Figure 4.2: *Static structure factors for silica colloids in water/glycerol, deionized (squares) and non-deionized (circles). The volume fraction* $\phi = 0.05$*. The lines through the data represent model calculations with a DLVO potential [eq. 4.10]. The reduced temperature* $T^* = 2 \cdot 10^{-2}$ *(dashed line) and* $4.9 \cdot 10^{-4}$ *(solid line). The electrostatic screening parameter* $\kappa_e d = 12$ *(dashed line) and 6 (solid line).*

4.4.1.1 Osmotic compressibility

The $q = 0$ limit of the structure factor is related to the isothermal osmotic compressibility χ_T by $S(0) = n_{coll} k_B T \chi_T$ [3]. $S(0)$ can be obtained from linearly extrapolating the structure factor to $q = 0$ on a plot against q^2, since it can be shown that $S(q) = S(0) + O(q^2)$ [3]. Figure 4.3(a) displays the structure factors at $\phi = 0.05$ as a function of the square of the wave vector. The straight lines are fits to the data at small q in order to obtain the osmotic compressibility. $S(0)$ is displayed in fig. 4.3(b) for all samples

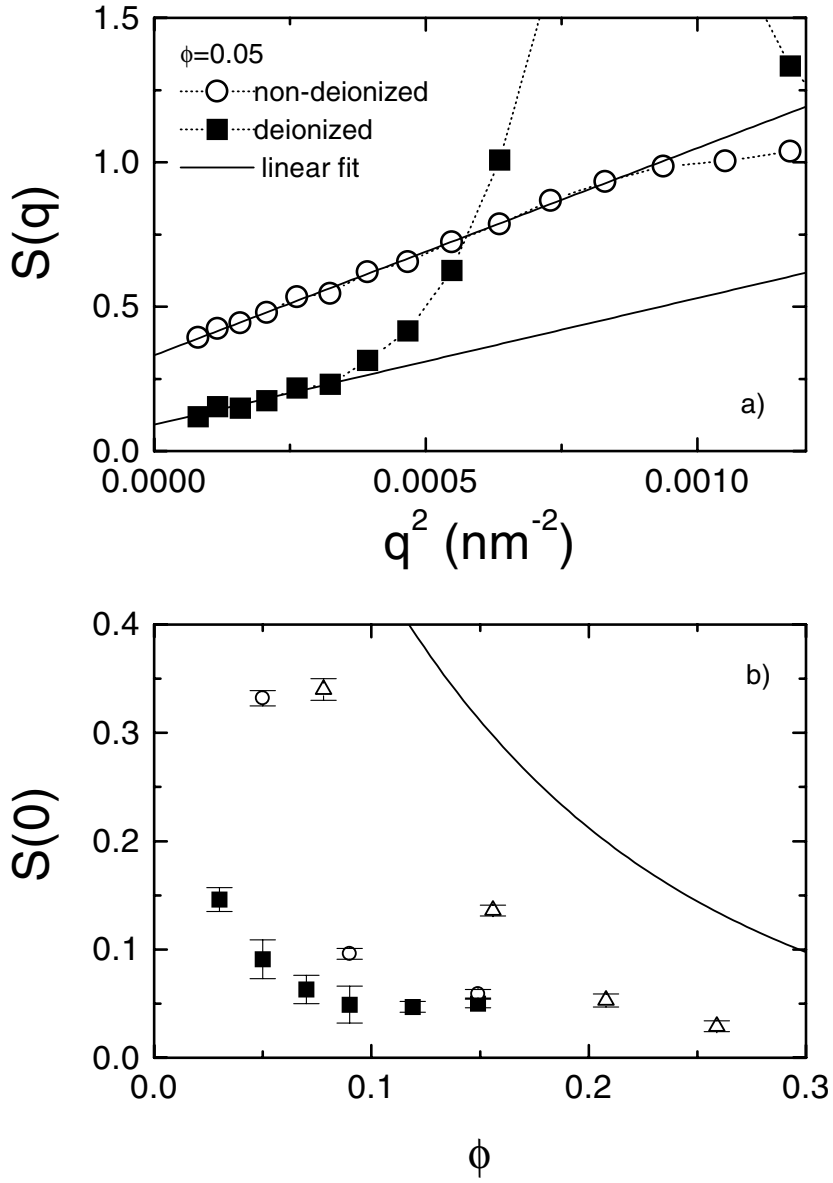

Figure 4.3: *(a): static structure factors for silica colloids in water/glycerol, deionized (squares) and non-deionized (circles). The volume fraction* $\phi = 0.05$*. The data are plotted against* q^2*. The straight lines are linear fits to the data at small* q*. (b): the* $q = 0$ *limit of the structure factors for suspensions of silica colloids in mixtures of ethanol and benzyl alcohol (triangles) or water and glycerol, non-deionized (circles) and deionized (squares). The solid line represents the behavior of hard spheres.*

discussed in this chapter[1]. $S(0)$ decreases with increasing volume fraction for all samples, qualitatively similar to the known behavior of hard spheres [solid line in fig. 4.3(b)]. The hard-sphere values shown in fig. 4.3(b) were obtained from the Carnahan-Starling equation of state [69]. The decrease of the osmotic compressibility with increasing volume fraction is characteristic of systems with repulsive interactions [64]. However, $S(0)$ is substantially smaller than in the hard-spheres case for all samples, indicating that they are effectively more dense than hard spheres at the same volume fraction. For instance, $S(0) \approx 0.05$ for the deionized samples at the highest volume fraction of $\phi = 0.149$; for hard spheres, this value of $S(0)$ corresponds to $\phi \approx 0.38$. The deviation from the hard-sphere result is smallest for the ethanol/benzyl alcohol samples and largest for the deionized samples in water/glycerol. This behavior is expected due to the fact that the range and strength of the electrostatic repulsion between the particles increases as the salt concentration in the liquid decreases [9]. Note also the large difference between the non-deionized samples in water/ glycerol and in ethanol/ benzyl alcohol; this confirms that the direct interaction depends sensitively on the suspending fluid. An important observation is that for all samples, $S(0)$ shows a continuous volume fraction dependence, i.e., no first-order phase transition occurs. A phase transition would be observable by a jump in the osmotic compressibility [70]. We can conclude that the samples remain in the same thermodynamic state at all volume fractions.

4.4.1.2 Mean interparticle spacing

The peak position of the static structure factor is related to the mean interparticle spacing r_m by $r_m \approx 2\pi/q_m$ [3]. In monodisperse suspensions of hard spheres, $r_m = d$ independent of volume fraction, where $d = 2a$ is the particle diameter. In fig. 4.4 we show $2\pi/q_m$ in units of the particle diameter. The mean interparticle spacing is largest for the deionized suspensions in water/glycerol and smallest for the samples in ethanol/benzyl alcohol, again indicating that the range of the electrostatic repulsion is largest for the deionized samples. At small volume fractions, the mean interparticle spacing is about twice the particle diameter in the deionized case. For all samples,

[1]Except for the sample in ethanol/benzyl alcohol with the largest volume fraction of $\phi = 0.311$. For this sample, $S(0)$ could not be determined due to a misalignment of the guard slit, leading to too strong parasitic scattering from the collimating aperture at small q.

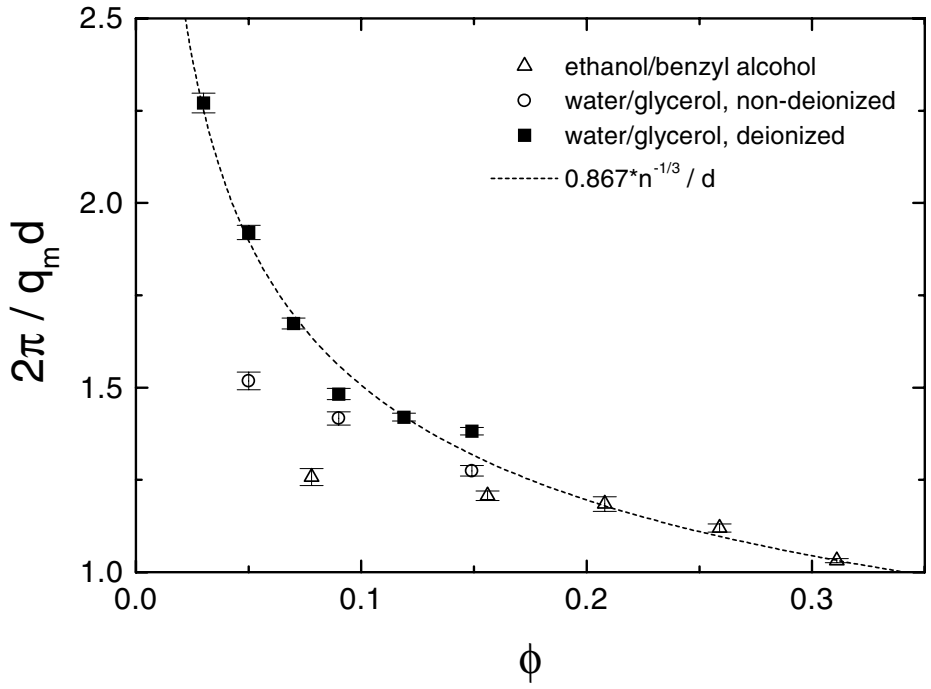

Figure 4.4: *Mean interparticle spacing for suspensions of silica colloids in mixtures of ethanol and benzyl alcohol (triangles) or water and glycerol, non-deionized (circles) and deionized (squares). The mean interparticle spacing is obtained from the peak position q_m of the static structure factor. The dashed line represents a constant times the average geometrical distance $n_{coll}^{-1/3}$.*

$2\pi/q_m d$ decreases with increasing volume fraction. The volume fraction dependence of the mean interparticle spacing can have two possible causes. First, the range of the electrostatic repulsion between the particles depends on the concentration of counterions in the liquid, which is proportional to the number density of colloids [1]. Secondly, an upper limit for the mean interparticle spacing is set by the average geometrical distance between the particles, which is proportional to $n_{coll}^{-1/3}$. If the range of the direct interaction becomes comparable to $n_{coll}^{-1/3}$, the mean interparticle spacing will be given by the geometrical upper limit and we expect $2\pi/q_m d \propto n_{coll}^{-1/3}$. The dashed line in fig. 4.4 represents a constant of order unity times the average geometrical distance. It is seen that the data for the deionized samples are described relatively well by the assumption that the mean interparticle spac-

ing is determined by the geometrical limit. It seems likely, therefore, that the deionized samples form expanded structures where the particles are kept at a maximum distance.

4.4.1.3 Model calculations

In order to quantify the effect of deionization on the static structure factor, we performed calculations with a model potential for the direct interaction between the colloids. In the Derjaguin-Landau-Verwey-Overbeek (DLVO) theory, which is widely used to describe charge stabilized colloidal suspensions, the interparticle potential is approximated by [9]

$$\begin{aligned} u(r) &= \frac{Q_0^2}{\varepsilon}\Big(\frac{Z}{1+\kappa_e a}\Big)^2 \frac{e^{-\kappa_e(r-d)}}{r}, \quad r \geq d \\ &= \infty, \qquad\qquad\qquad\qquad\quad r < d. \end{aligned} \tag{4.10}$$

Here, Q_0 is the elementary charge, ε the dielectric constant of the liquid and Z the effective charge number of the colloidal particles. In this theory, the potential consists of a screened Coulomb interaction and a short-range hard-core repulsion, the latter inhibiting an overlap of the particles. The Coulomb interaction is screened due to counterions, that have dissociated from the surface of the colloids, and excess salt in the fluid. Assuming monovalent ions, the electrostatic screening parameter κ_e is given by

$$\kappa_e^2 = \frac{4\pi Q_0^2}{\varepsilon k_B T}(n_{coll}|Z| + 2n_s), \tag{4.11}$$

where n_s is the number concentration of excess salt. Because of relation 4.11 the range of the direct interaction decreases as the number density of colloids increases.

Taking the DLVO potential as input, we can calculate the structure factor numerically. Details of the integral equations used are given in appendix A.

The dashed line in fig. 4.2 represents a calculation of the structure factor with $T^* = 2 \cdot 10^{-2}$ and $\kappa_e d = 12$, where T^* is the thermal energy reduced with the contact potential, i.e., $T^* = k_B T/u(r = d)$. It is seen that this calculation reproduces the structure factor for the non-deionized sample rather well. As the sample is deionized, the reduced temperature decreases by about a factor 40 to $T^* = 4.9 \cdot 10^{-4}$, and the screening parameter by a factor 2 to $\kappa_e d = 6$ (solid line in fig. 4.2). This behavior indicates a strong increase of the

strength and range of the direct interaction. The reduced temperature would translate to an effective charge number of $Z = 150$ in the non-deionized case and of $Z = 550$ in the deionized case. This apparent increase of the effective charge number is however an artifact, which is seen by fitting structure factors at higher volume fractions. For $\phi = 0.07$, for instance, we find $T^* = 5 \cdot 10^{-8}$ and $\kappa_e d = 20$ in the deionized case, which gives $Z = 1.5 \cdot 10^5$; this effective charge number is unphysical for the kind of slightly charged silica colloids we use here. The apparent strong increase of Z and $\kappa_e d$ with increasing volume fraction shows in fact that the DLVO potential in the simple form of eq. 4.10 is not adequate anymore for these dense, deionized systems, and that the reduced temperature and screening parameter should merely be regarded as fitting parameters. However, the calculations clearly demonstrate that the direct interaction between the particles becomes much stronger as the samples are deionized and the volume fraction increases.

4.4.1.4 Summary

In this section, we have presented a rather simplified discussion of the static properties of the colloidal suspensions studied, since we are mainly interested in the dynamical properties and we will use the static structure factors only as input to determine $H(q)$. We have shown that the direct interaction between the particles becomes much stronger as the suspensions are deionized, and that the particles are most probably kept at a maximum possible distance. It should be noted, however, that the description of the static properties of charge stabilized colloidal suspensions is in itself an interesting and much more complicated subject; it might therefore be worthwhile to perform a more elaborate analysis of the structure factors in the future, e.g. by adapting the model potential.

4.4.2 Dynamics

According to eq. 4.6, the hydrodynamic function $H(q)$ can be determined by a measurement of $S(q)$, D_0, and the short-time collective diffusion coefficient $D(q)$. The latter is obtained from the initial decay of time-dependent intensity correlation functions.

Figures 4.5 and 4.6(a) show typical intermediate scattering functions at $\phi = 0.089$ and 0.149, determined with DXS. Typical accumulation times were 30 - 60 min. Correlation functions at the same wave vector are compared

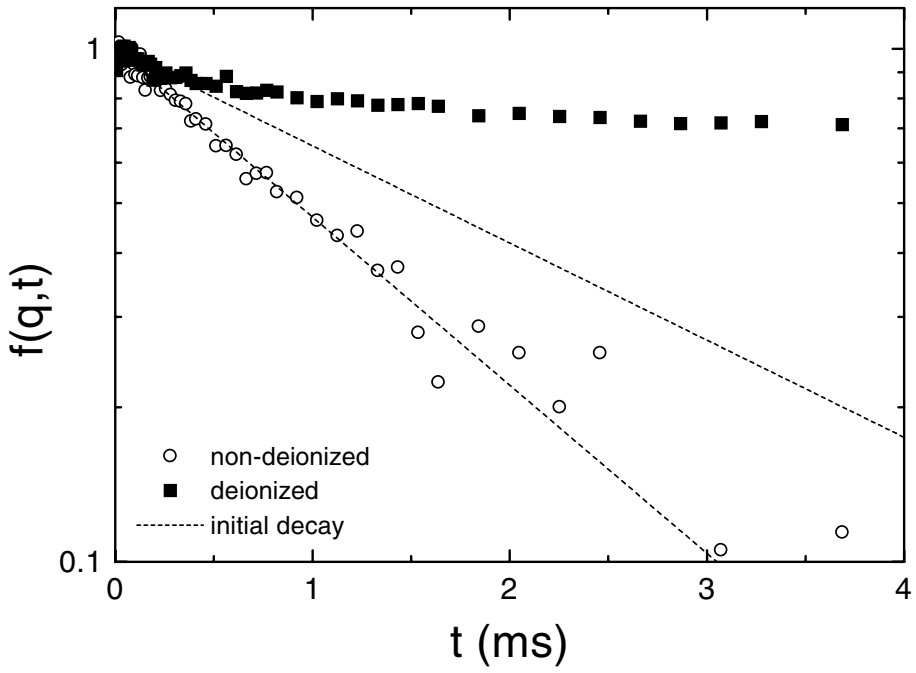

Figure 4.5: *Normalized intermediate scattering function measured with DXS on samples of silica colloids in water/glycerol, non-deionized (circles) and deionized (squares). The volume fraction* $\phi = 0.089$*. The wave vector* $q = 0.0378\ nm^{-1}$*. The straight lines represent the initial decay of the intermediate scattering functions.*

for non-deionized and deionized samples. The correlation functions of the deionized samples are less exponential and their initial decay is slower (at these wave vectors) as compared to the non-deionized samples. This behavior indicates that, although the nominal volume fraction is the same, the system becomes effectively more dense as the range of the direct interaction increases [9].

The deviations from a single exponential decay of $f(q,t)$ result from memory effects (see eq. 4.1) that become dominant at times larger than the structural relaxation time, as discussed in section 4.2. However, in this work we are interested in the short-time behavior, characterized by $t \ll \tau_a$. The short-time behavior is quantified by the first cumulant. ¿From the data shown in figs. 4.5 and 4.6(a), we obtain the first cumulant in the following way. First,

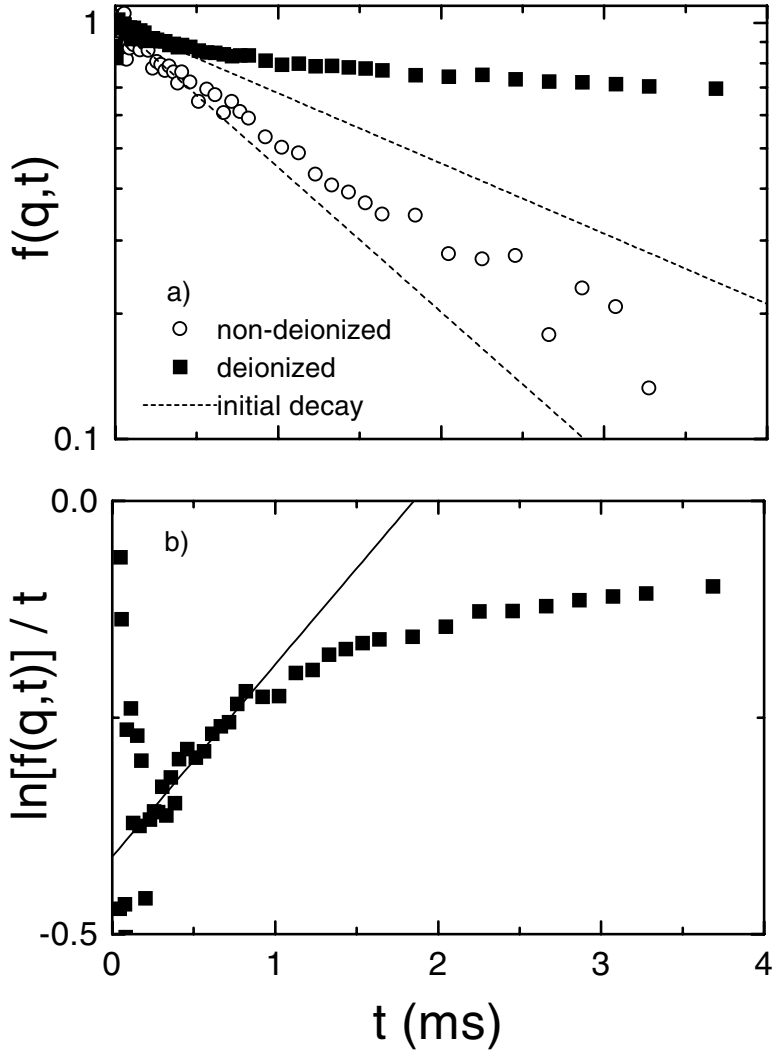

Figure 4.6: *(a): normalized intermediate scattering function measured with DXS on samples of silica colloids in water/glycerol, non-deionized (circles) and deionized (squares). The volume fraction* $\phi = 0.149$*. The wave vector* $q = 0.0414\ nm^{-1}$*. The straight lines represent the initial decay of the intermediate scattering functions. (b): the logarithm of the intermediate scattering function for the deionized sample in (a), divided by the time. The straight line is a linear fit to the data at small times.*

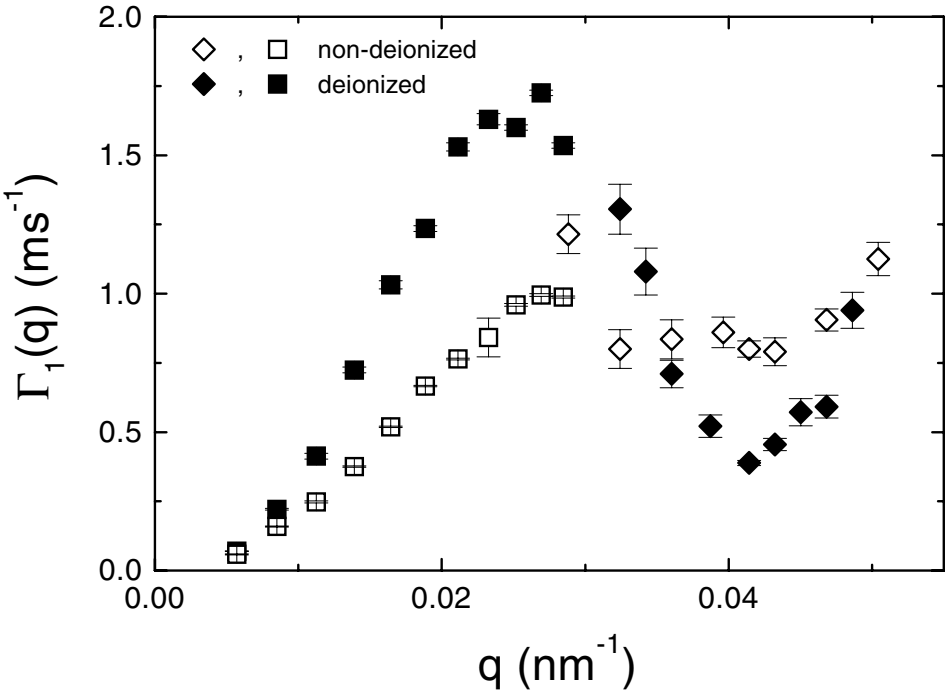

Figure 4.7: *First cumulant of intermediate scattering functions measured with CCDLS (squares) and DXS (diamonds) on samples of silica colloids in water/glycerol. The open symbols show data on a non-deionized sample, the solid symbols on a deionized sample. The volume fraction* $\phi = 0.149$ *in both cases.*

an exponential decay is fitted to the intermediate scattering functions at short times, where deviations from an exponential decay are small (typically $t \leq 0.1\tau_a$). This gives a first estimate for $\Gamma_1(q)$. In order to obtain a more accurate value for the first cumulant the second cumulant, i.e., the deviation from a single exponential decay at small times, has to be taken into account. According to eq. 2.10, the logarithm of the intermediate scattering function behaves as

$$\frac{\ln[f(q,t)]}{t} = \Gamma_1(q) + \Gamma_2(q)t \tag{4.12}$$

at short times. This means that the first cumulant can be determined by a linear fit to $\ln[f(q,t)]/t$ at short times, an example of which is shown in fig. 4.6(b). This procedure typically leads to corrections of about 15-20 % on the

first estimate for $\Gamma_1(q)$ for the most non-exponential correlation functions.

The first cumulant is depicted in fig. 4.7 for samples at a volume fraction of $\phi = 0.149$. It is evident that $\Gamma_1(q)$ exhibits a strong dependence on wave vector, the q dependence being more pronounced for the deionized sample. For both samples, there is a clear local minimum in the first cumulant (or relaxation rate) at about $q = 0.04$ nm^{-1} and a maximum at smaller wave vectors. The figure demonstrates that CCDLS (squares) and DXS (diamonds) can be combined to enlarge the accessible range of wave vectors substantially. We will discuss the q dependence of the relaxation rate in terms of the collective diffusion coefficient in more detail below.

4.4.2.1 Collective diffusion coefficient

The first cumulant gives the collective short-time diffusion coefficient $D(q)$. Figure 4.8 shows the inverse of the short-time diffusion coefficient and the static structure factor for a non-deionized and a deionized suspension (volume fraction $\phi = 0.089 \pm 0.002$). The diffusion coefficient was divided by that for a dilute sample, D_0, measured with dynamic light scattering. Both dynamic x-ray scattering and cross-correlated dynamic light scattering data are shown (diamonds and squares, respectively). The overlap between CCDLS and DXS in fig. 4.8(a) demonstrates that the detection of multiply scattered light is effectively suppressed by the two-fiber cross-correlation technique. The combination of the two methods probes the dynamics over about one decade in scattering vector. Since the structure factor is more strongly peaked for the deionized sample, the available q range for DXS is more restricted than for the non-deionized sample; far away from the structure factor peak, the scattered intensity becomes too low for dynamic x-ray scattering.

Several features are apparent from fig. 4.8. First, the inverse of the diffusion coefficient mimics the q dependence of the static structure factor, as it is expected from eq. 4.6. At small q, diffusion is obviously enhanced with respect to a dilute system, while a strong slow down occurs around the peak position of $S(q)$. This behavior is similar to that of hard spheres [61]. The reduced compressibility as compared to a dilute system leads to a faster relaxation of long-wavelength density fluctuations, whereas the relaxation on length scales of the order $2\pi/q_m$ is slowed down by the hindrance of the motion of particles by neighboring ones (a given particle is trapped in the cage of surrounding other particles). Secondly, $D_0/D(q)$ is larger than $S(q)$ at all wave vectors. This implies $H(q) < 1$ (see eq. 4.6), that is, hydrodynamic

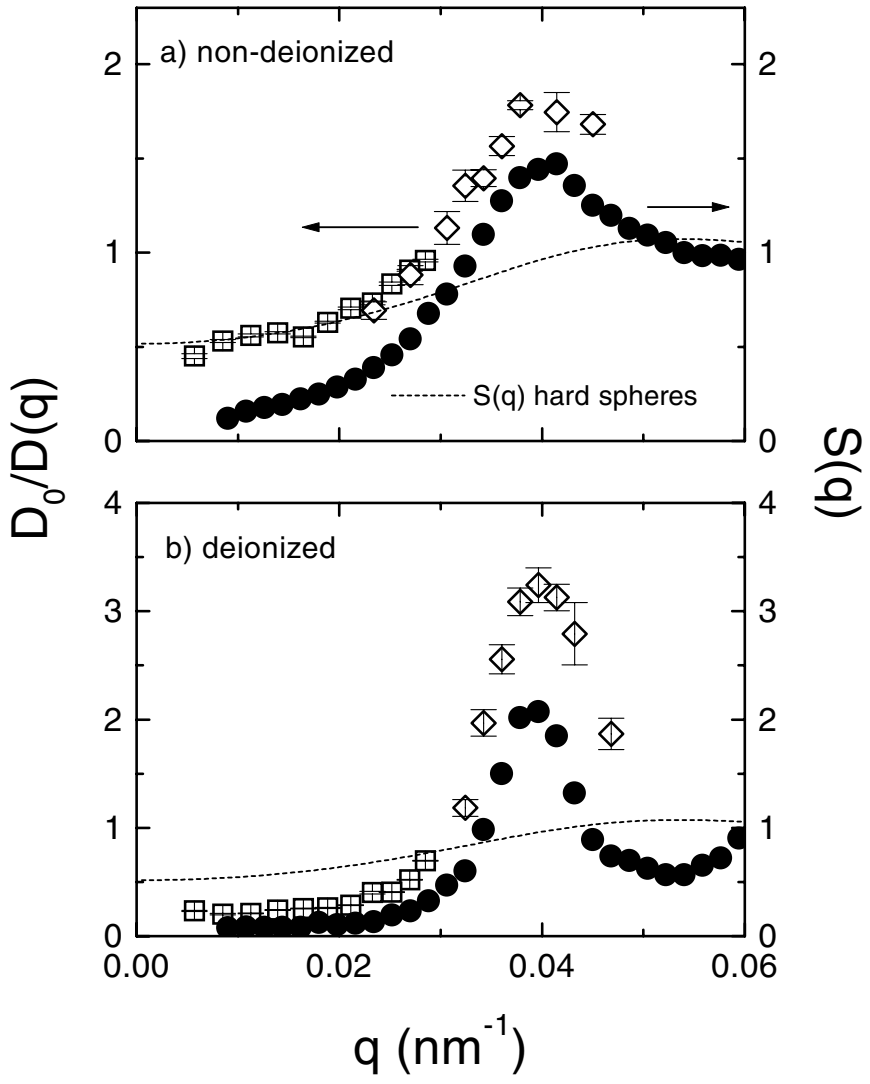

Figure 4.8: *Inverse of the short-time collective diffusion coefficient (squares CCDLS, diamonds DXS) and static structure factor (circles) for (a) non-deionized and (b) deionized silica colloids in water-glycerol. The volume fraction* $\phi = 0.089$*. The diffusion coefficient is scaled by that of a dilute suspension,* D_0*. The dashed lines represent Percus-Yevick hard-sphere calculations for the structure factor.*

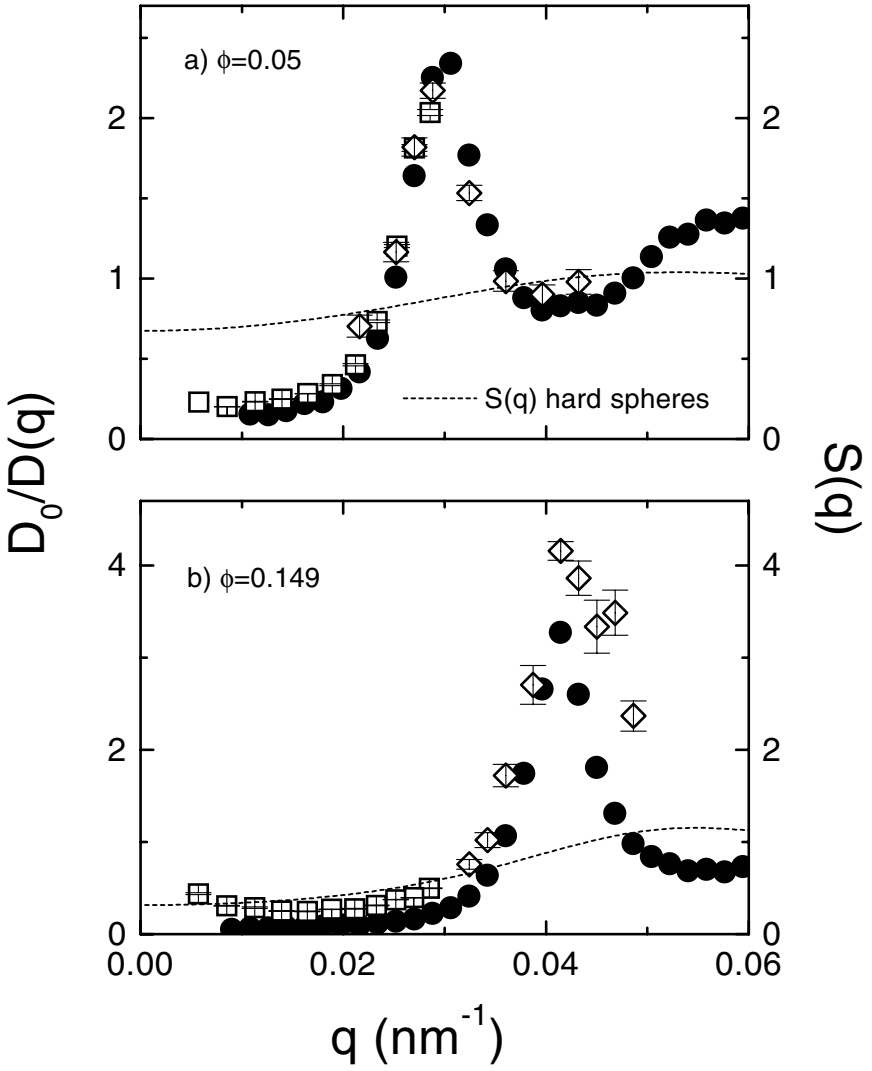

Figure 4.9: *Inverse of the short-time collective diffusion coefficient (squares CCDLS, diamonds DXS) and static structure factor (circles) for deionized silica colloids in water-glycerol. The volume fractions* $\phi = 0.05$ *(a) and 0.149 (b). The diffusion coefficient is scaled by that of a dilute suspension,* D_0*. The dashed lines represent Percus-Yevick hard-sphere calculations for the structure factor.*

interactions slow down diffusion. Thirdly, both the q dependence of the structure factor and the diffusion coefficient become more pronounced at larger volume fraction. Fourthly, the structure factors differ significantly from the hard-sphere structure factor at the same volume fraction, represented by the dashed lines in fig. 4.8. The deviation from the hard-sphere structure factor is substantially more pronounced for the deionized sample, as discussed already in section 4.4.1.

Figure 4.9 shows the inverse of the collective short-time diffusion coefficient for two other (deionized) samples, at volume fractions $\phi = 0.05$ and 0.149. On the whole, the same qualitative features as discussed above are apparent. There are, however, two significant differences to the data shown in the previous figure. First, the peak in the structure factor is somewhat larger than the one in $D_0/D(q)$ for $\phi = 0.05$. This result will be discussed in detail in section 4.4.2.4. Secondly, the height of the structure factor peak for $\phi = 0.149$ is 3.27, which is substantially above the freezing criterion of 2.85 given by Hansen and Verlet [71]. Therefore, this sample probably represents an undercooled liquid.

There are significant quantitative differences between $D_0/D(q)$ and the structure factor, as is evident from figs. 4.8 and 4.9. In the following we will concentrate on these differences, which are quantified by the function $H(q)$ [see eq. 4.6].

4.4.2.2 Hydrodynamic function

Since all relevant quantities have been measured, the hydrodynamic function can be determined purely experimentally, without taking recourse to any theoretical model. The first cumulant, the static structure factor and D_0 give an effective hydrodynamic function according to eq. 4.6. To avoid misunderstanding, we note that in a system with strong direct interactions, this experimentally determined effective hydrodynamic function may actually contain contributions from the direct interaction as well. It is understood that the term "hydrodynamic function" refers to this experimentally obtained effective function in the following.

The central experimental result of this chapter is shown in figs. 4.10, 4.11 and 4.12. These figures show the hydrodynamic function $H(q)$ for silica colloids in water/glycerol at volume fractions $\phi = 0.05$, 0.089 and 0.149, respectively. Figures 4.10(a), 4.11(a) and 4.12(a) show data on non-deionized samples, figs. 4.10(b), 4.11(b) and 4.12(b) on deionized samples. At $\phi =$

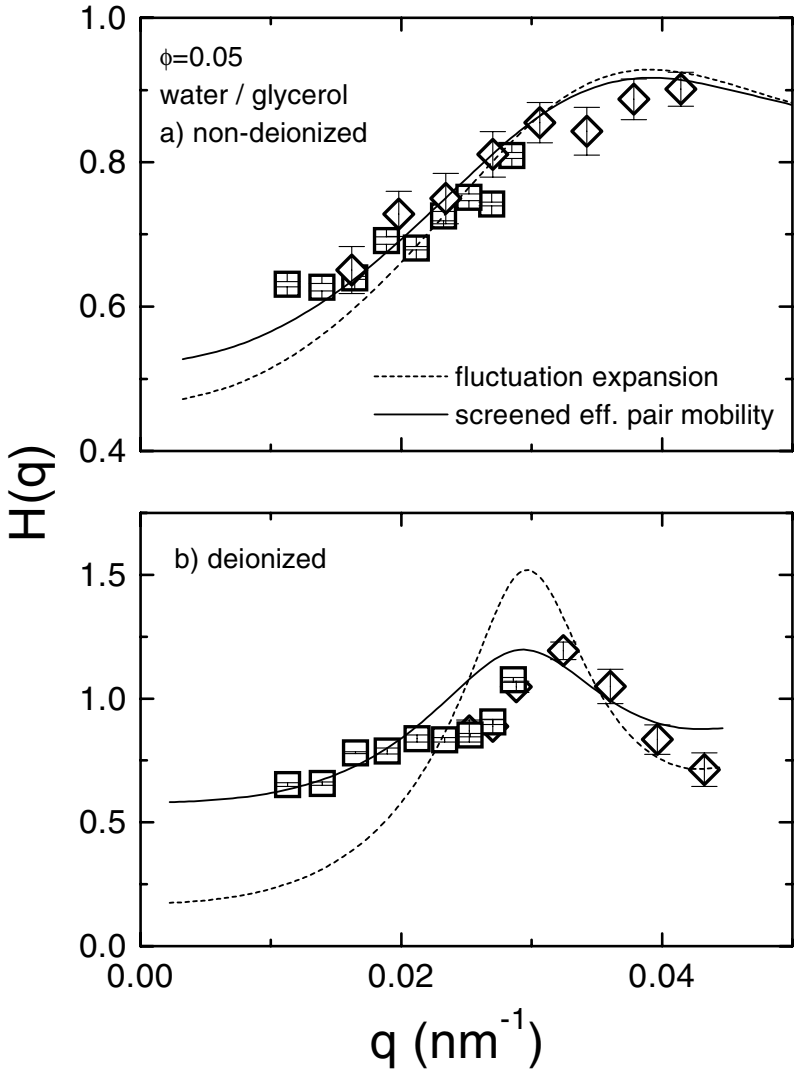

Figure 4.10: *Hydrodynamic function for silica colloids in a mixture of water and glycerol, (a) non-deionized and (b) deionized. The volume fraction* $\phi = 0.05$ *in both cases. CCDLS (squares) and DXS (diamonds) results are shown. The dashed curves represent calculations with the theory by Beenakker and Mazur. The solid lines represent calculations with a screened effective hydrodynamic pair mobility.*

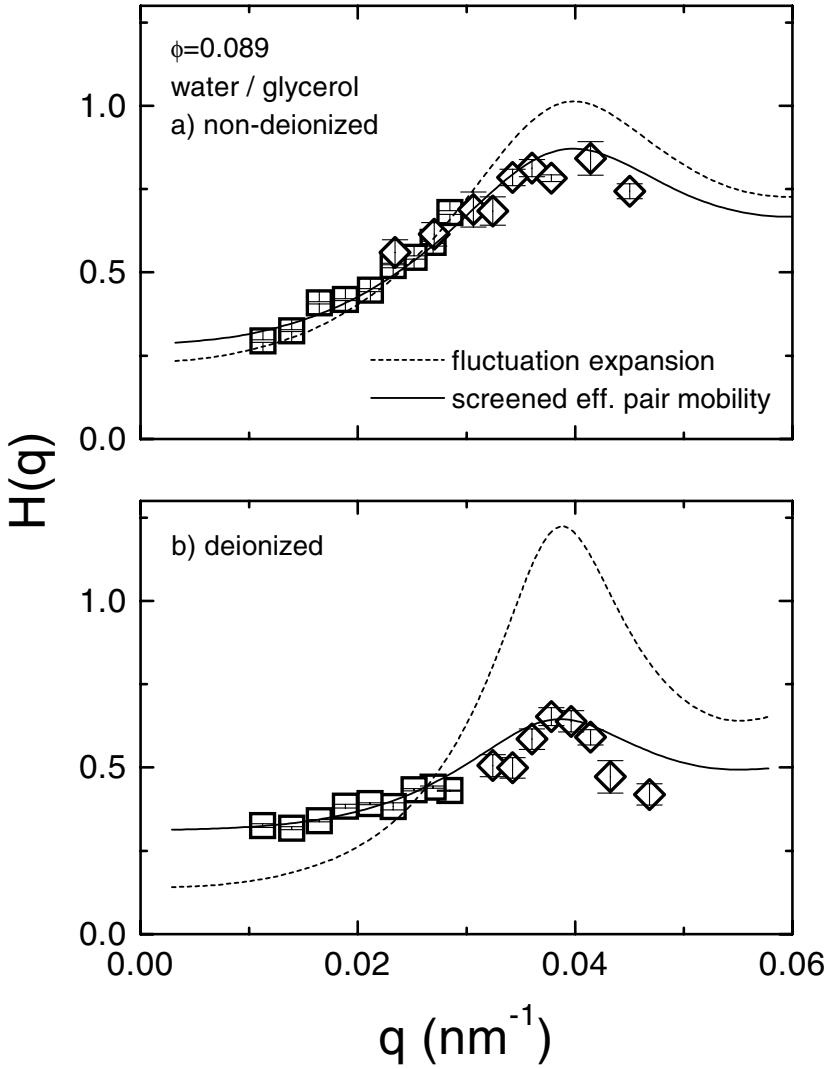

Figure 4.11: *Hydrodynamic function for silica colloids in a mixture of water and glycerol, (a) non-deionized and (b) deionized. The volume fraction* $\phi = 0.089$ *in both cases. CCDLS (squares) and DXS (diamonds) results are shown. The dashed curves represent calculations with the theory by Beenakker and Mazur. The solid lines represent calculations with a screened effective hydrodynamic pair mobility.*

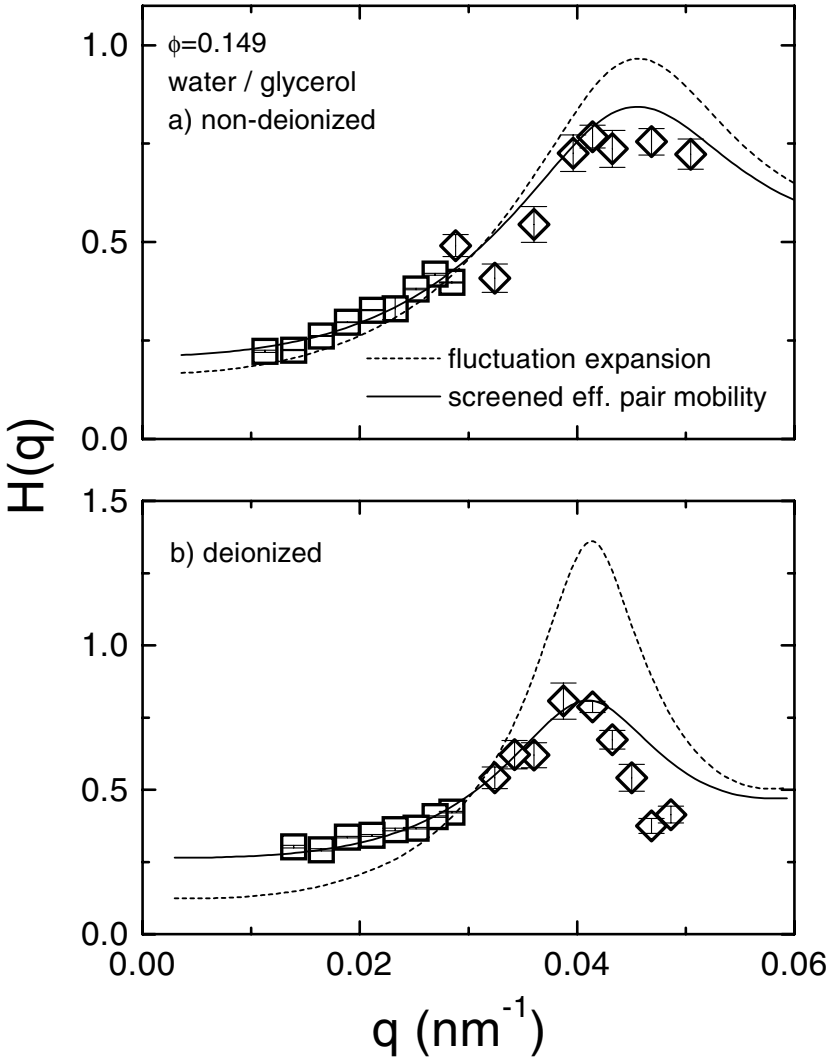

Figure 4.12: *Hydrodynamic function for silica colloids in a mixture of water and glycerol, (a) non-deionized and (b) deionized. The volume fraction* $\phi = 0.149$ *in both cases. CCDLS (squares) and DXS (diamonds) results are shown. The dashed curves represent calculations with the theory by Beenakker and Mazur. The solid lines represent calculations with a screened effective hydrodynamic pair mobility.*

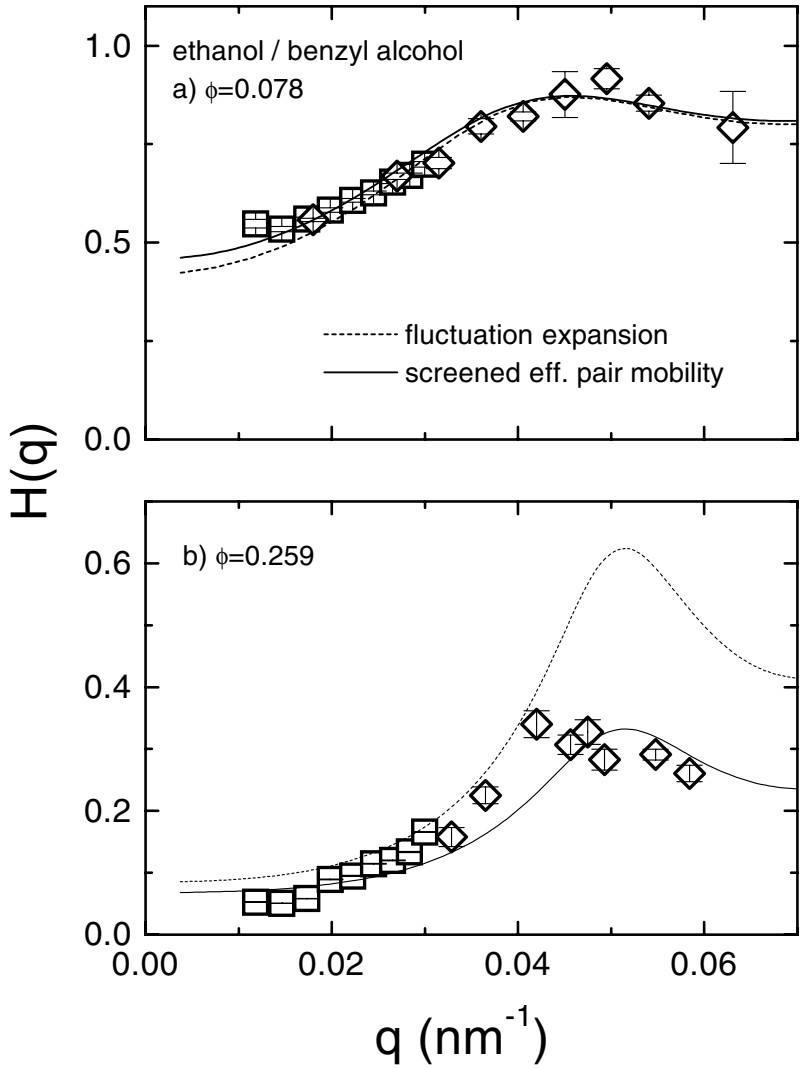

Figure 4.13: *Hydrodynamic function for silica colloids in a mixture of ethanol and benzyl alcohol, (a) $\phi = 0.078$ and (b) $\phi = 0.259$. DLS (squares) and DXS (diamonds) results are shown. The dashed curves represent calculations with the theory by Beenakker and Mazur. The solid lines represent calculations with a screened effective hydrodynamic pair mobility.*

0.089 and 0.149, the hydrodynamic interaction behaves qualitatively similarly to hard-sphere-like systems [61]: $H(q)$ is smaller than 1 for all wave vectors, indicating a hydrodynamic hindrance of diffusion. This effect is largest at small q. For the lower volume fraction of $\phi = 0.05$, the maximum value of $H(q)$ for the deionized case is slightly above 1, in contrast to a hard-sphere system. The experimental curves are compared to the fluctuation expansion [47] (dashed lines), taking the measured structure factor as input for the calculations. For the non-deionized samples, reasonable agreement with the theory is found. However, small systematic deviations are apparent: $H(q)$ shows less structure than expected from the calculation. As the samples are deionized, these deviations become large, revealing two essential differences to the hard-sphere case: the maximum value of $H(q)$ is much smaller and the q dependence substantially less pronounced than theoretically expected [figs. 4.10(b)-4.12(b)]. We will show below that the flattening of $H(q)$ can phenomenologically be described as hydrodynamic screening.

Figure 4.13 shows the hydrodynamic function for two suspensions in an index-matching mixture of ethanol and benzyl alcohol. As has been demonstrated in section 4.4.1, these samples are closest to the hard-sphere case as far as the structure factor is concerned. For relatively low volume fractions [fig. 4.13(a), $\phi = 0.078$)], the data are in good agreement with the hard-sphere theory. At large volume fractions the maximum value of $H(q)$ becomes much smaller than expected from the Beenakker and Mazur theory, similar to the deionized samples [fig. 4.13(b)]. This effect is known from hard-spheres at very large volume fractions of about $\phi \geq 0.35$ [61], where the Beenakker and Mazur theory becomes inadequate to describe the data as far as the absolute value is concerned. The q dependence remains however almost unaltered with respect to the fluctuation expansion theory for the ethanol/benzyl alcohol samples, which is again similar to the behavior of hard spheres at large ϕ [61].

4.4.2.3 Effective hydrodynamic screening

Since the fluctuation expansion theory cannot describe our data sufficiently in the case of deionized suspensions, we now resort to a phenomenological description in terms of a screened effective pair mobility.

The strong q dependence of $H(q)$ in the case of hard spheres (dashed lines in figs. 4.10-4.13) is predominantly due to the Oseen term in the effective hydrodynamic pair mobility (eq. 4.9). To elucidate this point, we show a

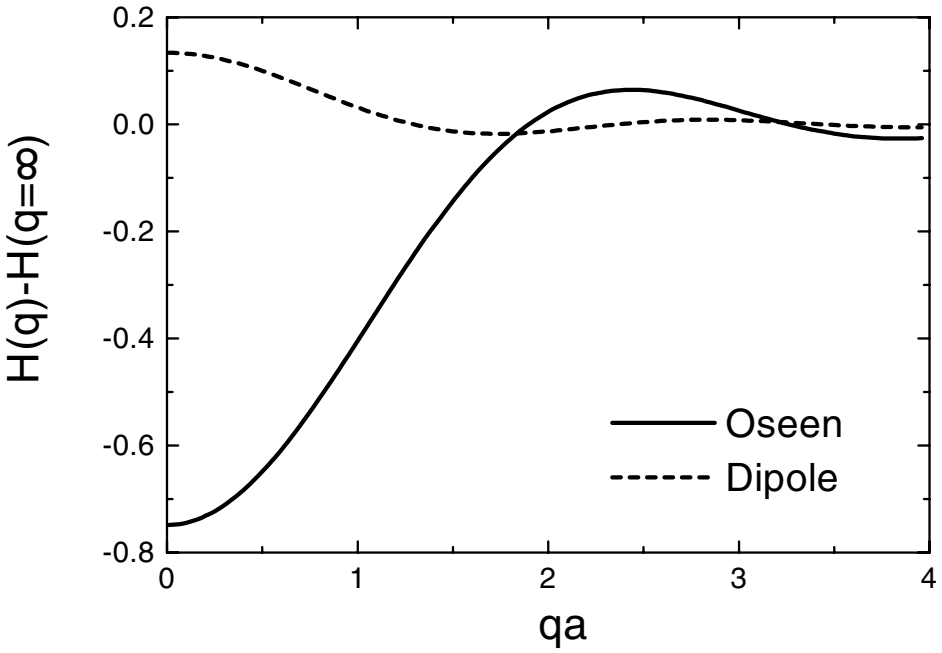

Figure 4.14: *Simplified calculation of the Oseen contribution (solid line) and dipole contribution (dashed line) to the hydrodynamic function.*

simplified calculation of the Oseen- and dipole contributions to the hydrodynamic function in fig. 4.14, according to the expressions given by Cichocki and Felderhof [46]. These authors crudely approximate the pair distribution function $g(r)$ by a unit step function, $g(r) = 1$ for $r \geq 2a_{eff}$ and zero otherwise, to perform the ensemble average. Here, a_{eff} is an effective particle radius, which is a rough measure for the range of the direct interaction. It is natural to choose $a_{eff} = \pi/q_m$. The calculations are done for the example $\phi = 0.089$ and $q_m = 0.0386$ nm^{-1}, corresponding to the sample shown in figs. 4.8(b) and 4.11(b). As is evident from fig. 4.14, the Oseen contribution exhibits a strong wave vector dependence, whereas the dipole contribution is almost flat. In particular, the Oseen contribution becomes dominant for small q, which is expected due to the long range of this term in real space.

The simplified consideration given above suggests a possible description of the observed flattening of the hydrodynamic function in terms of effective hydrodynamic screening [7, 54, 55, 56, 57, 58, 59, 60]. A reduction of the q dependence of the hydrodynamic function is achieved by screening the long-

range Oseen contribution, as will now be shown.

Combining eqs. 4.7 and 4.9, one obtains

$$H(q) = \mu^* 6\pi\eta a\Big(1 + \frac{1}{(2\pi)^3}\int d\mathbf{q}'\hat{\mathbf{q}}\cdot\mathbf{A}(\mathbf{q}')\cdot\hat{\mathbf{q}}[S(|\mathbf{q}-\mathbf{q}'|)-1]\Big), \qquad (4.13)$$

where $\hat{\mathbf{q}}$ is a unit vector. In the hard-sphere theory, $\mathbf{A}(\mathbf{q})$ is given by [47, 72]

$$\mathbf{A}(\mathbf{q}) = \frac{4}{3}\pi a^3\frac{9}{2}(1-\hat{\mathbf{q}}\hat{\mathbf{q}})[\frac{1}{(aq)^2} - \frac{1}{3} + O(q^2)]. \qquad (4.14)$$

The first term in the square brackets in eq. 4.14 is dominant for $q \to 0$ and represents the long-range Oseen term in real space. The following terms represent the dipole contribution ($\propto 1/R^3$). Eqs. 4.13 and 4.14 are the starting point for describing our data. In analogy to porous media [56] and stationary hard-sphere suspensions [59], we introduce screening into the model by substituting

$$\frac{1}{(aq)^2} \to \frac{1}{(aq)^2 + (a/l_{scr})^2} \qquad (4.15)$$

in eq. 4.14. This substitution leads to a sum of exponentially screened terms and a dipole-like interaction in real space (see below), with screening length l_{scr} [73]. In order to adjust the absolute value of $H(q)$, we take the $q = \infty$ limit of the effective mobility, μ^*, as a free parameter. The solid lines in figs. 4.10-4.13 represent numerical calculations according to eq. 4.13 with the screened form of $\mathbf{A}(\mathbf{q})$. Again, the measured structure factor has been used to perform the ensemble average. Screening clearly leads to a flattening of the hydrodynamic function, in good agreement with the experiment. For the non-deionized samples and the samples in ethanol/benzyl alcohol, hydrodynamic screening is weak (screening length $l_{scr} \approx 10a$). Furthermore, we find $\mu^* 6\pi\eta a \approx \eta/\eta(\phi)$ for these samples up to $\phi \approx 0.2$, where $\eta(\phi)$ is the viscosity of a hard-sphere suspension at volume fraction ϕ [66, 74] (see section 4.4.2.4). We conclude that the data for non-deionized samples are well described by particles interacting by a slightly screened effective hydrodynamic pair interaction in a fluid of viscosity $\eta(\phi)$, which is still close to the behavior of hard spheres. The essential difference to hard spheres and to previous results on slightly charged, non-deionized systems [51] is however the introduction of effective hydrodynamic screening. Strikingly, hydrodynamic screening is much more pronounced for the deionized samples, as is evident from figs. 4.10(b)-4.12(b). In order to describe the flattening of the data

as compared to the hard-sphere theory, a screening length of about 3 particle radii is needed [solid lines in figs. 4.10(b)-4.12(b)]. The hydrodynamic screening length has been chosen to fit the data at small q, where screening is expected to be important. Then, the agreement of the screened hydrodynamic function with the data appears to become worse for $q > q_m$, which seems quite reasonable: wave vectors $q > q_m$ correspond to distances smaller than the mean interparticle spacing, where screening cannot be effective.

Hydrodynamic screening length The hydrodynamic screening length l_{scr} is a phenomenological parameter that quantifies the deviation of the effective hydrodynamic function from the hard-sphere case. In fig. 4.15(a) we show the hydrodynamic screening length for both non-deionized and deionized samples as a function of volume fraction. At all volume fractions, the screening length becomes substantially shorter as the samples are deionized. This result indicates a strong dependence of hydrodynamic screening on the static structure, i.e., the pair distribution function. For the sake of comparison, the solid line in fig. 4.15(a) shows the hydrodynamic screening length found in simplistic effective-medium theories for porous media [56, 60]. The situation in a porous medium is comparable to a system where the particles remain fixed. If hydrodynamic forces act on a given particle in such a system, a counter-force is needed to keep the particle at its position. This mechanism leads to a force term in the equations of motion that is proportional to the velocity [55], giving rise to the screening properties [56]. The substitution 4.15 leads to an effective mobility given by

$$\begin{aligned}\mu^{eff} &= \mu^* \frac{3}{2}\Big(-\frac{a}{\xi^2 R^3}[\mathbf{1} - 3\frac{\mathbf{RR}}{R^2}] + \frac{ae^{-\xi R}}{R}[\mathbf{1} - \frac{\mathbf{RR}}{R^2}] \\ &\quad + \frac{ae^{-\xi R}}{\xi R^2}[\mathbf{1} - 3\frac{\mathbf{RR}}{R^2}] + \frac{ae^{-\xi R}}{\xi^2 R^3}[\mathbf{1} - 3\frac{\mathbf{RR}}{R^2}]\Big), \qquad (4.16)\end{aligned}$$

where $\xi = l_{scr}^{-1}$ [73, 56]. For $\xi = 0$, μ^{eff}/μ^* reduces to the unscreened Oseen tensor. In the case of porous media at low volume fractions, $l_{scr} = 1/\sqrt{4.5\phi}$ [solid line in fig. 4.15(a)]. It is seen from eq. 4.16 that in the presence of hydrodynamic screening, the leading far-field term in the mobility has a $1/R^3$ dependence instead of the $1/R$ behavior of the unscreened effective mobility [eq. 4.9]. As was shown quite recently, this result also holds for suspensions with regular arrangements of particles and remains qualitatively valid at all physically allowed volume fractions [60]. These calculations considered the

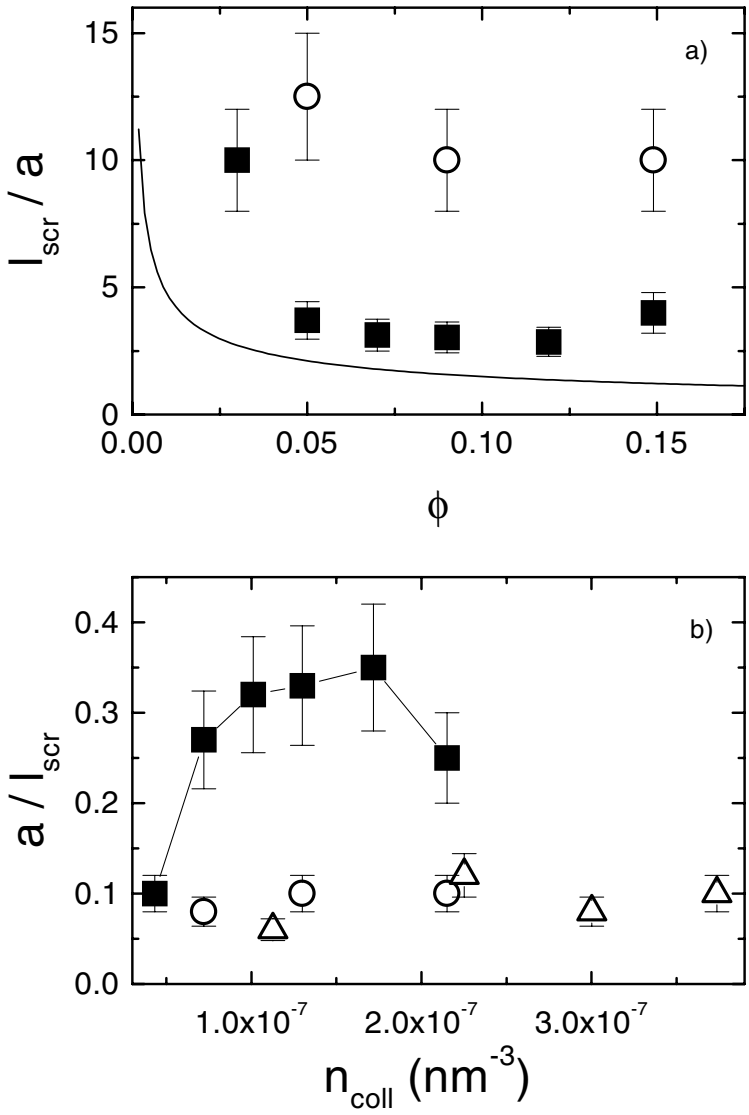

Figure 4.15: *(a): hydrodynamic screening length for suspensions of silica colloids in water/glycerol, non-deionized (circles) and deionized (squares). For comparison, the solid line represents the hydrodynamic screening length found in simplistic effective-medium calculations for porous media. (b): inverse of the hydrodynamic screening length for suspensions of silica colloids in water/glycerol, non-deionized (circles) and deionized (squares), and in ethanol/benzyl alcohol (triangles). The data are plotted against the number density of colloids.*

friction tensor, which is the inverse of the mobility. In the friction tensor, hydrodynamic interactions are via a suspension of fixed particles [56]. It appears that the hydrodynamic screening length found in our experiments approaches the porous-medium result as the samples are deionized and the direct interaction becomes more important, whereas screening vanishes in the hard-sphere limit.

As was pointed out already by Beenakker and Mazur [47], the effective pair mobility is unscreened only if the the particles can move freely. This suggests the following interpretation: the strong Coulomb interaction in the deionized systems prevents the particles from moving freely in response to the hydrodynamic field, leading to an effective screening similar to porous media. A microscopic theory for the hydrodynamic interactions in concentrated charge stabilized suspensions, which is not available at present, will have to capture these features.

Figure 4.15(b) shows the inverse of the hydrodynamic screening length for all samples as a function of the number density of colloids. For hard spheres, $1/l_{scr} = 0$. Again, it is seen that the non-deionized samples in water/glycerol and in ethanol/benzyl alcohol are rather close to the hard-sphere limit, with an average hydrodynamic screening length of 11 particle radii. In the previous experiment of Philipse and Vrij [51] on slightly charged silica, where no hydrodynamic screening was found, the number density was significantly smaller than in our experiment ($n_{coll} < 5 \cdot 10^{-8}$ nm^{-3}). Since hydrodynamic screening concerns the Oseen contribution to the hydrodynamic interaction, which describes the fluid velocity disturbance of a *point* particle, it is conceivable that the number density rather than the volume fraction is the decisive parameter for determining the screening length. However, the discrepancy between the two experiments is more likely due to differences in the direct interaction. In the Philipse and Vrij experiment, the samples were not deionized. We note that for their system, also the absolute value of $H(q)$ did not deviate from the theory of Beenakker and Mazur, suggesting that their samples behaved dynamically still hard-sphere like, similar to our non-deionized samples.

4.4.2.4 Dynamics at specific wave vectors

More insight into the physical effects governing the dynamical behavior may be gained by looking at the volume fraction dependence of the hydrodynamic function and the collective diffusion coefficient in specific limits. It is clear

that $H(q)$ and $D(q)$ are basically determined by their values at $q = 0$, $q = q_m$ and $q = \infty$. The $q = 0$ limit is associated with the effective hydrodynamic screening discussed above. The other limits will be considered in this section.

The $q = \infty$ limit of the effective mobility

The quantity μ^* in eqs. 4.9 and 4.13 is the $q = \infty$ limit of the effective mobility. Since $S(q \to \infty) = 1$, it follows from eq. 4.6 that $H(q = \infty) = D_s/D_0$, where $D_s = D(q = \infty)$ is the short-time self diffusion coefficient [9]. The short-time self diffusion coefficient describes the diffusive motion of a single particle (in the presence of other particles). As noted by Cohen and de Schepper [75], a generalized Stokes-Einstein relation of the form

$$D_s/D_0 \approx \eta/\eta(\phi) \tag{4.17}$$

holds approximately for the self diffusion coefficient of hard spheres. Equation 4.17 is a generalization of the Stokes-Einstein relation

$$D_0 = \frac{k_B T}{6\pi\eta a}, \tag{4.18}$$

valid at infinite dilution. The Stokes-Einstein relation expresses a coupling of mass transport (as characterized by the diffusion coefficient) to the transverse momentum transport (as characterized by the shear viscosity). The correspondence between D_s/D_0 and $\eta/\eta(\phi)$, though not exact, as pointed out by Weitz and Ladd [76] and discussed by Beenakker [77], has the advantage of being intuitively appealing: a particle diffuses through an effective medium of viscosity $\eta(\phi)$. Banchio *et al.* [66] recently examined the validity of generalized Stokes-Einstein relations in more detail and also found it to be approximately valid for the self-diffusion coefficient at not too high volume fractions; up to $\phi \approx 0.2$, the deviations from eq. 4.18 are rather small ($\leq 15\%$). Moreover, many attempts have been made to arrive at viral expansions for the short-time self diffusion coefficient of hard spheres [47, 50, 78, 79, 80], with slightly differing results. The accepted value for the first viral coefficient is that first obtained by Batchelor [50], 1.83.

In fig. 4.16(a) we show μ^*, multiplied by the Stokes friction coefficient $6\pi\eta a$, for the water/glycerol samples as a function of volume fraction. The solid line represents the viscosity ratio $\eta/\eta(\phi)$ for hard-sphere suspensions [66]. It is seen that within experimental error, the data for the non-deionized

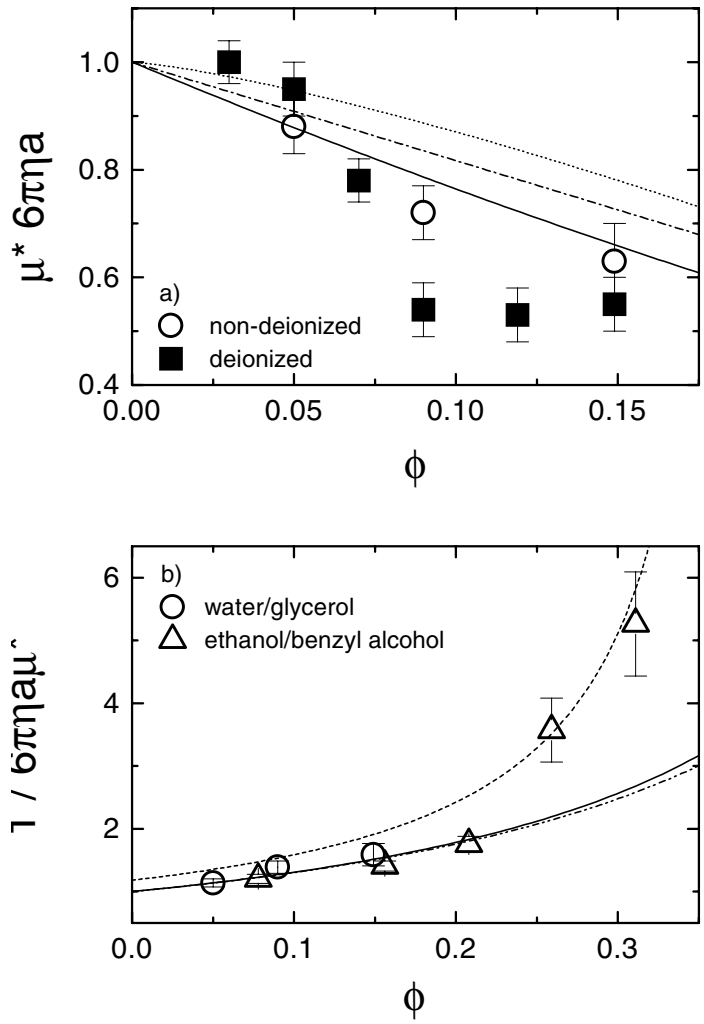

Figure 4.16: *(a): the $q = \infty$ limit of the hydrodynamic function for silica colloids in water/glycerol, non-deionized (circles) and deionized (squares). The solid line represents the inverse of the viscosity of hard-sphere suspensions. The dotted line represents the predicted behavior of charged colloids at low volume fraction. The dash-dotted line represents the viral expansion result, $1 - 1.83\phi$. (b): the inverse of $H(q = \infty)$ for non-deionized samples in water/glycerol (circles) and ethanol/benzyl alcohol (triangles). The solid line represents the viscosity of hard-sphere suspensions. The dash-double-dotted line represents the hard-sphere pair distribution function at contact. The dashed line represents the function $1.2/(1 - \phi/\phi_p)$, with $\phi_p = 0.39$.*

samples follow the hard-sphere viscosity ratio and lie only slightly below the viral expansion result for hard spheres (dash-dotted line). This confirms again that the hydrodynamic interaction in these samples behaves approximately hard-sphere-like. By contrast, μ^* clearly deviates from the hard-sphere behavior in the case of dionized samples. For $\phi \geq 0.089$, $\mu^* 6\pi\eta a$ falls substantially below the hard-sphere viscosity ratio and remains almost constant, i.e., it decouples from the volume fraction. This behavior indicates that the volume fraction alone is not the appropriate parameter for describing the self diffusion in these deionized systems (see below). For $\phi = 0.03$ and 0.05, the data for the deionized systems lie *above* the hard sphere values. This behavior has been predicted by Watzlawek and Nägele [81], who calculated numerically the self-diffusion coefficient of salt-free suspensions by taking into account hydrodynamic terms up to R^{-20} (where R is the interparticle distance). These authors predict

$$\frac{D_s}{D_0} = 1 - 2.59\phi^{1.3} \tag{4.19}$$

for $\phi \leq 0.05$. Equation 4.19 is represented by the dotted line in fig. 4.16(a); it is in agreement with the data on the deionized samples only at the lowest volume fractions.

Figure 4.16(b) shows $1/6\pi\eta a\mu^*$ for all non-deionized samples as a function of volume fraction (water/glycerol and ethanol/benzyl alcohol). The solid line represents $\eta(\phi)/\eta$ for hard spheres. It is evident that the ethanol/benzyl alcohol data follow the hard-sphere viscosity up to $\phi \approx 0.2$ and then rise steeply, which is probably due to the vicinity of the freezing transition. Brady [82] has inferred from computer simulation data that for hard-spheres, the short-time self diffusion coefficient behaves as

$$\frac{D_0}{D_s} \approx \frac{1.2}{1 - \phi/\phi_p} \tag{4.20}$$

in the vicinity of the random close packing volume fraction $\phi_p = 0.64$ [83]. The dashed line in fig. 4.16(b) represents eq. 4.20 with $\phi_p = 0.39$, which is consistent with our observation that the ethanol/benzyl alcohol systems solidify at about $\phi = 0.35 - 0.4$. The data are well described by eq. 4.20 at high volume fractions. We can again conclude that the dynamics of the samples in ethanol/benzyl alcohol and of the non-deionized samples in water/glycerol is qualitatively similar to that of hard spheres.

Hydrodynamics or direct interaction? At this point it should be noted that an alternative description for transport properties of colloidal suspensions has been proposed, that is entirely based on an analogy to atomic liquids and does thus not incorporate hydrodynamic interactions (in the sense in which this term is used in colloid science) [74, 84, 85]. In this theory, transfer of momentum and energy between the colloidal particles is due to direct interactions only. In this approach, the short-time self diffusion coefficient is given by

$$D_s = \frac{D_0}{\chi(\phi)}, \tag{4.21}$$

where $\chi(\phi)$ is the equilibrium radial distribution function of two hard spheres at contact. Expression 4.21 is analogous to the Enskog theory for dense molecular gases [86]. The factor $\chi(\phi)$ accounts for the increased collision frequency of molecules in a dense fluid as compared to a dilute gas. In the Carnahan-Starling approximation, $\chi(\phi)$ is given by

$$\chi_{CS} = \frac{1 - 0.5\phi}{(1-\phi)^3}. \tag{4.22}$$

The dash-double-dotted line in fig. 4.16(b) represents χ_{CS}, which is almost indistinguishable from the normalized hard-sphere viscosity $\eta(\phi)/\eta$ at small to moderate volume fractions. At high volume fractions, $\chi(\phi)$ has the form of eq. 4.20 [82], i.e., this alternative description remains valid. In view of this discussion, it should be recalled that the experimentally determined hydrodynamic function $H(q)$ must be seen as an *effective* hydrodynamic interaction, to which possible effects resulting from direct interactions, if not captured by the structure factor in eq. 4.6, will contribute as well.

In addition to the molecular-fluid analogy and the Beenakker and Mazur theory, there is a large body of other theoretical work on the dynamics of hard-sphere suspensions [78, 79, 80, 87]. The theory by Tokuyama and Oppenheim [87], for instance, who derive a generalized diffusion equation for the particle number density starting from the fluctuating Navier-Stokes equation, is valid at all volume fractions. However, most of these theories consider only the self diffusion coefficient or the q region around the structure factor peak. By contrast, the theory by Beenakker and Mazur is valid at all q and has been tested extensively, in the whole q range available, by computer simulations and experiments [61, 62, 88]. Therefore, we have compared our results

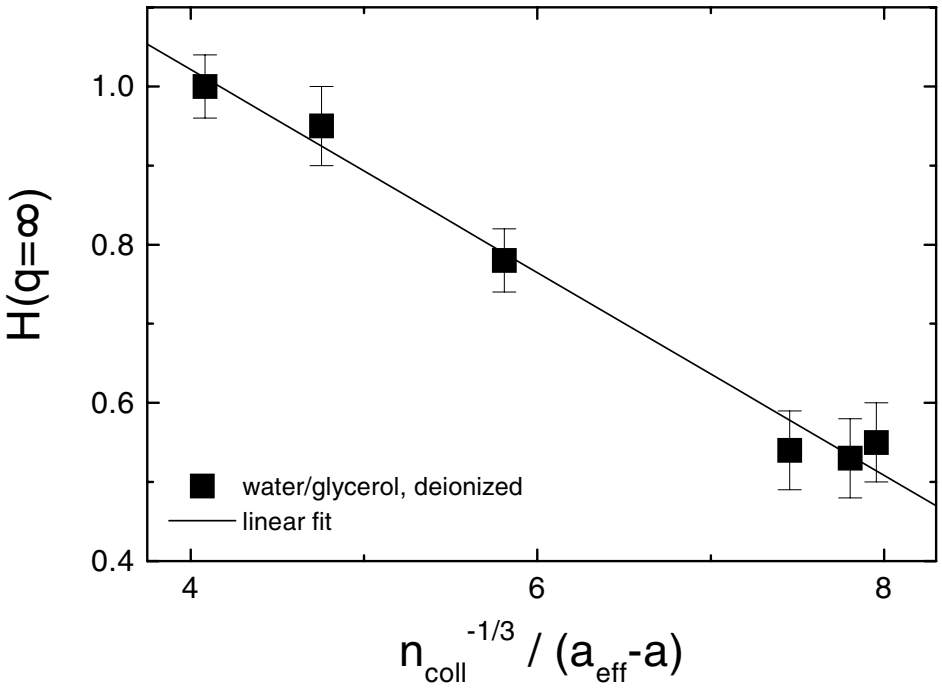

Figure 4.17: *The $q = \infty$ limit of the hydrodynamic function for deionized samples of silica colloids in water/glycerol as a function of the parameter $\psi = n_{coll}^{-1/3}/(a_{eff} - a)$. The straight line is a linear fit to the data.*

for $H(q)$ with the hydrodynamic theory of Beenakker and Mazur.

Deionized samples Here we report some interesting experimental observations on the deionized samples, which may help to interpret the data. Figure 4.17 shows the $q = \infty$ limit of the effective hydrodynamic function for the deionized samples as a function of the parameter $\psi = n_{coll}^{-1/3}/(a_{eff} - a)$. The reason for choosing this parameter is that we intuitively expect the potential energy of the system to be determined by the ratio of the average geometrical distance ($\propto n_{coll}^{-1/3}$) to the distance between the surfaces of two particles ($\propto a_{eff} - a$). Interestingly, $H(q = \infty)$ decreases linearly with increasing ψ for the deionized samples, as is evident from fig. 4.17, suggesting that ψ is the appropriate parameter for describing self diffusion in these systems. Since ψ is related to the *direct* interaction only, this discussion suggests that the

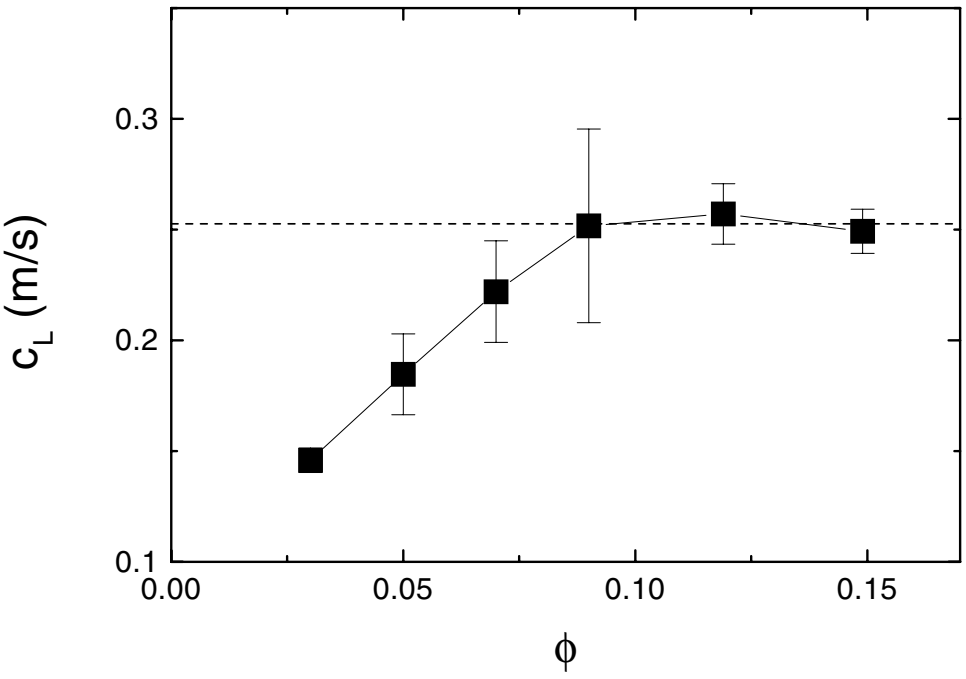

Figure 4.18: *Longitudinal sound velocity for deionized samples of silica colloids in water/glycerol as a function of volume fraction. The straight line represents the average sound velocity at large ϕ, where it levels off.*

direct interaction is of great importance for the motion of a single particle in the deionized suspensions. In this context, it is also instructive to report the following finding. Figure 4.18 shows the longitudinal sound velocity c_L of the deionized colloidal suspensions as a function of volume fraction. The sound velocity is given by

$$c_L = \sqrt{\frac{1}{n_{coll} M_{coll} \chi_T}}, \tag{4.23}$$

where M_{coll} is the mass of a colloidal particle [70]. As can be seen from fig. 4.18, the sound velocity initially increases linearly with ϕ and then levels off[2]. The leveling-off occurs at the same volume fraction at which the self-diffusion coefficient becomes constant (see fig. 4.16). Assuming that the self

[2]We note that Grüner and Lehmann [70] found that the longitudinal sound velocity of colloidal crystals is independent of particle concentration, whereas it increases with concentration in the fluid phase. However, at the liquid-solid phase transition a clear jump

diffusion of the deionized samples at higher volume fractions is predominantly determined by the direct interaction, we may speculate that self diffusion is coupled to the longitudinal sound mode of the suspensions via direct interactions. In other words, a single particle experiences the compressibility, or elastic response, of the surrounding suspension. It appears that at short times (or large frequencies) the deionized samples show at least in part already an elastic or solid-like behavior. This may be related to the fact that the effective hydrodynamic interaction at small wave vectors appears to be screened (see section 4.4.2.3), in analogy to porous media, where the particles remain *fixed*. It is well established theoretically that hydrodynamic interactions in a suspension are screened, in precisely the way introduced in section 4.4.2.3, under the condition that the velocity of each of the particles vanishes on average [59]. This condition is distinct from the Beenakker and Mazur theory, where the particles are allowed to move freely, but is obviously met in a solid. It seems likely, therefore, that the effective hydrodynamic screening observed in the deionized samples arises from the importance of the direct interaction that leads to a partially solid-like behavior at high frequencies (or short times).

Hydrodynamic function in the peak

The fact that the hydrodynamic interaction in charge stabilized colloidal suspensions can behave qualitatively differently from the hard-sphere case was first noticed in connection with $H(q_m)$, the hydrodynamic function at the location of the peak of the static structure factor. Obviously, q_m defines a characteristic structural length scale of the system. It was found in earlier studies that $H(q_m)$ could become larger than 1, in contrast to hard spheres [51, 52, 53]. From an effective-medium point of view, this result seems counter-intuitive, since the effective viscosity of a colloidal suspension is always larger than that of the suspending fluid and one naively expects $D \propto 1/\eta(\phi)$.

Numerical calculations [66] and experiments [53, 61] show that

$$H(q_m) = 1 - 1.35\phi \tag{4.24}$$

in the sound velocity occurs, which is not seen here. Furthermore, from the dynamical measurements we know that the intermediate scattering functions decay to zero for all samples, indicating that the "cages" of particles eventually break up, as in a colloidal liquid.

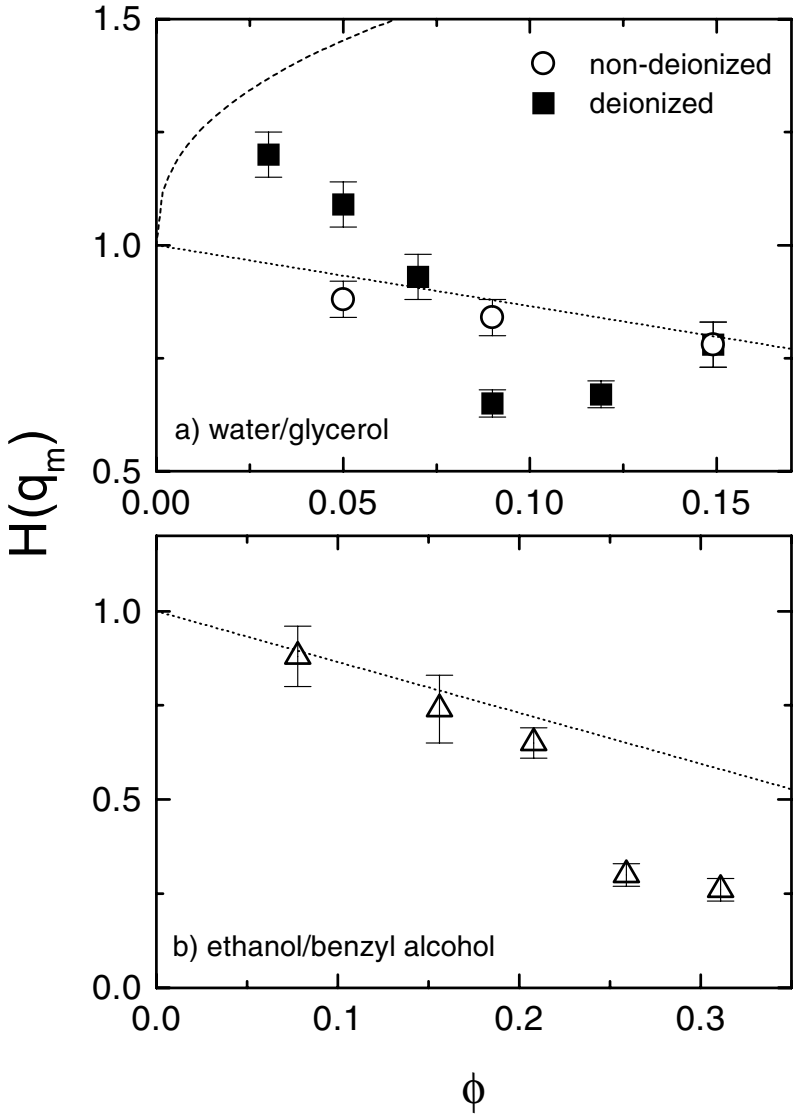

Figure 4.19: *Hydrodynamic function at the peak position of the static structure factor for suspensions of silica colloids in water-glycerol (a) and in ethanol-benzyl alcohol (b). The samples in water-glycerol are non-deionized (circles) and deionized (squares). The dotted line represents the hard-sphere behavior and the dashed line the behavior of highly charged colloids.*

for hard spheres up to the freezing transition, whereas

$$H(q_m) = 1 + 1.5\phi^{0.4} \tag{4.25}$$

for strongly charged systems at very low volume fractions. As a qualitative explanation for the different behavior of hard spheres and dilute strongly charged systems, Nägele *et al.* [43, 66] have suggested the following reasoning. The hydrodynamic hindrance of diffusion in the peak [$H(q_m) < 1$], that is characteristic of hard-sphere systems, can be understood in terms of near-field hydrodynamic interactions (lubrication forces). In hard-sphere systems these lubrication forces are of great importance, since configurations of nearly touching spheres are highly probable ($2\pi/q_m = d$). By contrast, near-field effects do not play a role in dilute highly charged systems, as the probability of finding particles closer together than the effective diameter $d_{eff} > d$ is practically zero. As a consequence, far-field effects become dominant. At a length scale $2\pi/q_m$, density fluctuations decay predominantly by the motion of neighboring particles in opposite directions [48]. This motion is supported by the far-field backflow effect of displaced fluid, leading to a hydrodynamic enhancement of diffusion at q_m [$H(q_m) > 1$].

Figure 4.19(a) shows $H(q_m)$ for the water/glycerol samples. The non-deionized systems follow the hard-sphere behavior (eq. 4.24, dotted line) rather closely, which is expected on the basis of the previous section. The deionized systems behave quite differently: $H(q_m)$ is larger than 1 at the smallest volume fraction of $\phi = 0.03$, then decreases with increasing volume fraction, falls below the hard-sphere line and eventually coincides with the hard-sphere value at the largest ϕ. This volume fraction dependence is qualitatively similar to that of $H(q = \infty)$ [see fig. 4.16(a)]. $H(q_m)$ for the deionized samples not only deviates from the hard-sphere case, but also from the behavior of dilute strongly charged systems (eq. 4.25, dashed line); however, it approaches this behavior at small volume fractions. In fig. 4.19(b) we show $H(q_m)$ for the samples in ethanol/benzyl alcohol as a function of volume fraction. For these systems $H(q_m)$ follows the hard-sphere behavior up to $\phi \approx 0.2$ and then falls substantially below the hard-sphere results. This volume fraction dependence is qualitatively similar to that of $H(q = \infty)$ [see fig. 4.16(b)], suggesting that it is largely determined by the self-diffusion coefficient.

Deionized samples Again we report an interesting experimental finding on

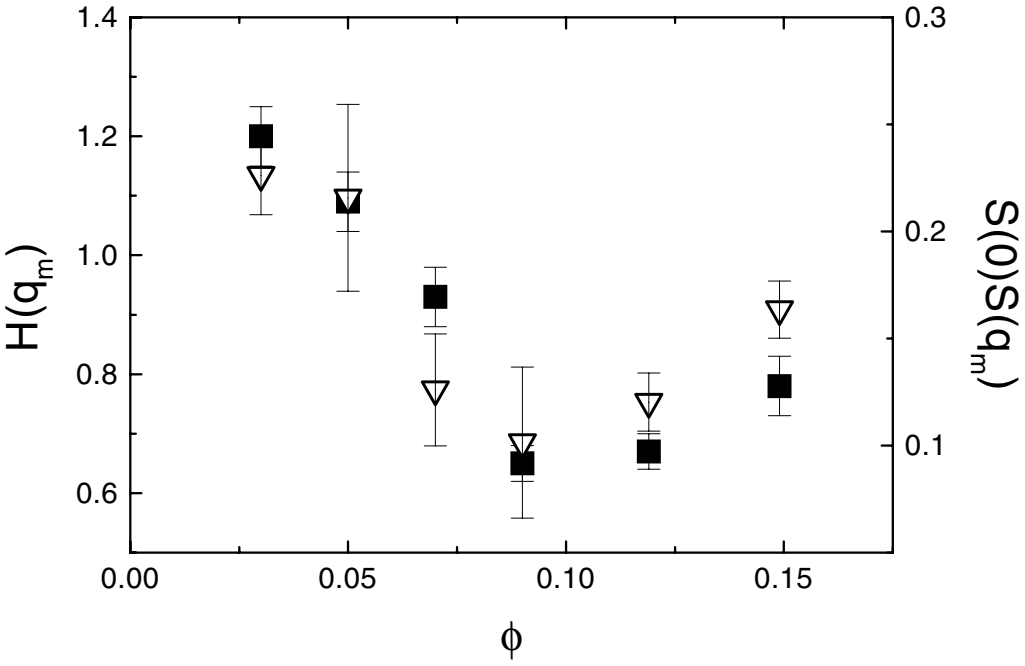

Figure 4.20: *Hydrodynamic function at the peak position of the static structure factor for suspensions of silica colloids in a deionized mixture of water and glycerol (squares) and the product $S(0)S(q_m)$ (triangles) for the same samples.*

the deionized samples. In section 4.4.2.4 we argued that the direct interaction plays an important role for self diffusion in these systems. We also conjectured that a given particle initially experiences the elastic response of its compressible environment. This means that the self-diffusion mode of the system couples to the longitudinal sound mode, as characterized by the compressibility. $H(q_m)$ shows a similar volume fraction dependence as the self-diffusion coefficient, suggesting that comparable arguments hold here. To elucidate this point, fig. 4.20 shows $H(q_m)$ for the deionized samples in water/glycerol along with the bilinear product $S(0)S(q_m)$. Strikingly, the volume fraction dependences of these two quantities are almost identical. The reason for comparing $H(q_m)$ and $S(0)S(q_m)$ is that the coupling of dynamical modes is described by bilinear products of slowly varying dynamical variables [89]; the slowly varying dynamical variables of interest here are the density fluctuations. Thus, $S(0)S(q_m)$ describes the coupling of the modes

represented by $S(0)$ and $S(q_m)$, and we therefore expect $H(q_m)$ to be linked to this product if the reasoning given above is correct. With this in mind, we see from fig. 4.20 that the (at first sight rather unusual) volume fraction dependence of $H(q_m)$ for the deionized samples might be explained by a mode-mode coupling argument.

Diffusion in the peak

In this section, we discuss $D(q_m)$, the short-time collective diffusion coefficient at the peak position of the structure factor. We discuss $D(q_m)$ here to highlight differences between charge stabilized and hard-sphere systems. Recently, Banchio, Nägele and Bergenholtz [66] showed theoretically that for hard spheres, a generalized Stokes-Einstein relation holds approximately for $D(q_m)$:

$$\frac{D(q_m)}{D_0} \approx \frac{\eta}{\eta(\phi)}. \tag{4.26}$$

This relation is correct to within 10 % up to $\phi \approx 0.4$. By contrast, eq. 4.26 was found to be violated by at least a factor 2 in the case of dilute strongly charged systems.

In fig. 4.21, we show $D(q_m)/D_0$ for all samples. The solid line represents a calculation for hard spheres according to $D(q_m)/D_0 = H(q_m)/S(q_m)$. Here, the hydrodynamic function in the peak was calculated according to eq. 4.24 [66], and $S(q_m)$ was determined using the Verlet-Weiss correction to the Percus-Yevick approximation [90]. The high frequency limiting viscosity for hard sphere suspensions is represented by the dotted line [66, 74, 84]. It is evident that the diffusion coefficient at q_m deviates from the hard sphere result for all samples, the deviation being largest for the deionized samples. In particular, $D(q_m)$ for the deionized samples is much smaller than in the hard-sphere case. This decrease of the diffusion coefficient with respect to hard spheres indicates that these systems are, similar to the static properties, dynamically effectively more dense than the nominal volume fraction suggests. For example, $D(q_m)/D_0 \approx 0.25$ for the deionized samples at $\phi = 0.149$. In a hard-sphere suspension, this value of $D(q_m)$ occurs at $\phi \approx 0.39$; interestingly, this equivalent hard-sphere volume fraction is almost identical to the one inferred from the osmotic compressibility (see section 4.4.1.1). The behavior of the deionized samples is qualitatively similar to that of strongly charged systems, where a comparable decrease of $D(q_m)$ with respect to the

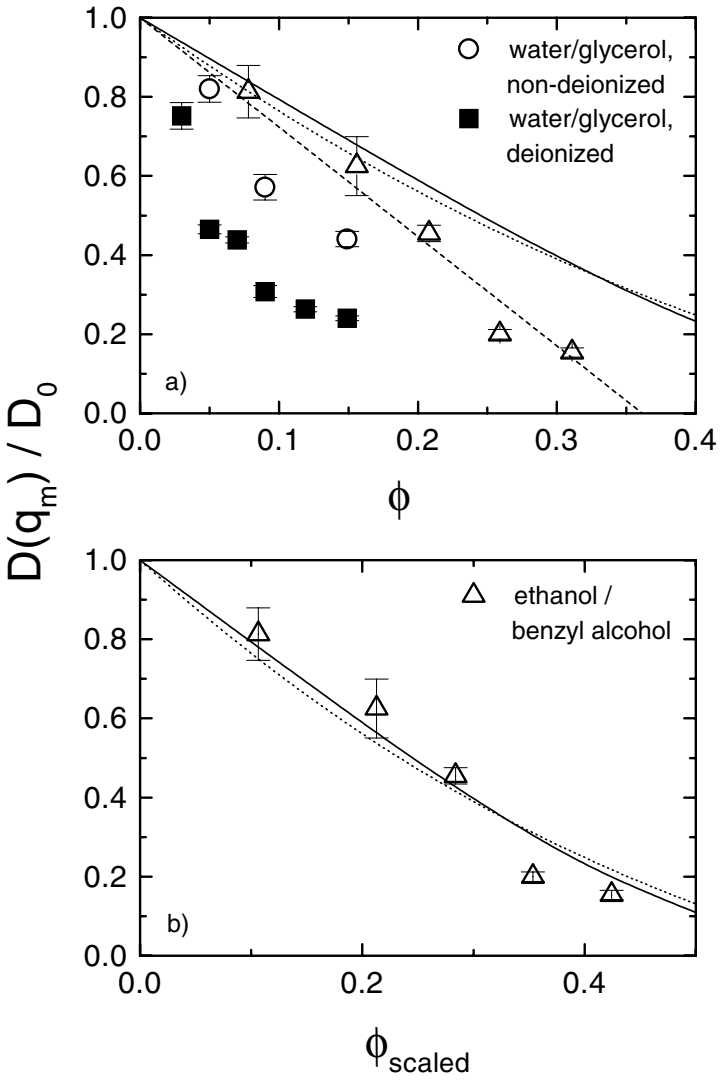

Figure 4.21: *Short-time collective diffusion coefficient in the peak of the static structure factor for silica colloids in ethanol/ benzyl alcohol (triangles) and water/glycerol, non-deionized (circles) and deionized (squares). The solid line represents the hard-sphere behavior. The dotted line represents the inverse of the viscosity of hard-sphere suspensions. The dashed line in (a) is a linear fit to the ethanol/benzyl alcohol data. Figure (b) shows the ethanol/benzyl alcohol data plotted against the scaled volume fraction* $\phi_{scaled} = \phi \cdot 0.495/0.36$.

hard sphere case is predicted [66]. Banchio *et al.* found $D(q_m)/D_0 \approx 0.35$ for strongly charged systems in the range $0.03 \leq \phi \leq 0.1$, which is rather close to our results on deionized suspensions at about $\phi = 0.1$. Considering the strong deviation of $H(q = \infty)$ and $H(q = q_m)$ from the results for highly charged systems [see figs. 4.16(a) and 4.19(a)], however, this correspondence of the absolute value of $D(q_m)$ with the calculations by Banchio *et al.* at larger volume fractions is probably coincidental.

For the samples in ethanol/benzyl alcohol, $D(q_m)$ shows an almost linear volume fraction dependence, whereas the ϕ dependence is clearly non-linear for the deionized samples. By fitting a straight line to the ethanol/benzyl alcohol data, we can obtain a volume fraction at which $D(q_m)$ formally becomes zero, which is the case at $\phi^* = 0.36 \pm 0.02$. As can be seen from fig. 4.21(a), $D(q_m)$ for hard spheres also decreases linearly, up to $\phi \approx 0.3$. Extrapolating the hard-sphere curve in the linear regime to $D(q_m) = 0$, analogous to the ethanol/benzyl alcohol data, we find $\phi = 0.495$. In fig. 4.21(b), the ethanol/benzyl alcohol data are plotted against the renormalized volume fraction $\phi_{scaled} = \phi 0.495/\phi^*$. It is seen that the data can roughly be scaled onto the hard-sphere calculation by this transformation, confirming that the ethanol-benzyl alcohol systems are qualitatively similar to hard-spheres.

4.4.2.5 Temperature dependent measurement

The hydrodynamic function $H(q)$, as defined in eq. 4.7, is expected to be independent of the viscosity of the suspending medium. $H(q)$ remains unchanged upon a change in the background viscosity, since all particles are affected in the same way. That $H(q)$ will be independent of η (within certain limits) can be seen as follows. A hydrodynamic disturbance diffuses through the suspending fluid with the kinematic viscosity $\nu = \eta/\rho_f$ as the diffusion constant, where ρ_f is the density of the fluid. Typically, $\nu \approx 1$ mPascm^3/1g $= 10^{-6}$ m^2/s. On the other hand, $D_0 \approx 10^{-12}$ m^2/s$\ll \nu$, which means that hydrodynamic interactions can be considered to act instantaneously on the time scale of colloidal diffusion, within all the physically reasonable range of ν. Only at time scales $t \ll a^2/\nu$, where hydrodynamic interactions build up, will the suspension viscosity play a role.

To check whether our results are indeed independent of the suspension viscosity, we prepared a sample of silica particles ($a = 54.9$ nm as before, $\phi = 0.312$) in a mixture of water and 70 wt% glycerol. The viscosity of this mixture depends strongly on temperature [91]. Figure 4.22 shows $D_0/D(q)$

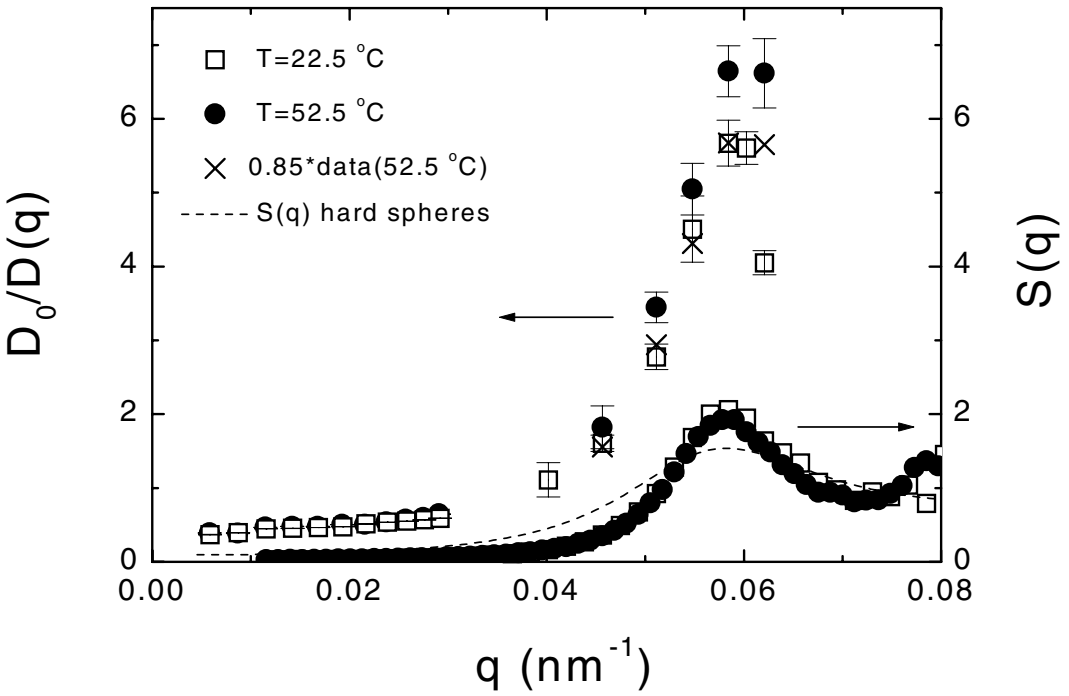

Figure 4.22: *Inverse of the short-time collective diffusion coefficient (squares) and static structure factor (circles) for silica colloids in water/ 70 wt% glycerol. The volume fraction* $\phi = 0.312$*. The diffusion coefficient is scaled by that of a dilute suspension,* D_0*. The open symbols are data at a temperature* $T = 22.5\ ^\circ C$*, the solid symbols at* $52.5^\circ C$*. The crosses are the x-ray data at the higher temperature multiplied by 0.85. The dashed lines represent Percus-Yevick hard-sphere calculations for the structure factor.*

and the static structure factor at two different temperatures, $T = 22.5$ °C and 52.5 °C. The shear viscosity of the suspending fluid at these temperatures is 20.1 mPas and 6.1 mPas, respectively. It is evident that the light scattering data (small q) are independent of T (to within about 5 %), whereas the x-ray scattering data at the higher temperature lie systematically about 15 % above the data at the lower temperature. This systematic difference is probably due to a deviation of the actual temperature of the sample from the nominal value, which translates into a corresponding deviation in the scaling factor D_0. In the x-ray setup, the sample is located in an evacuated chamber where the thermal contact to the sample holder is only provided by the

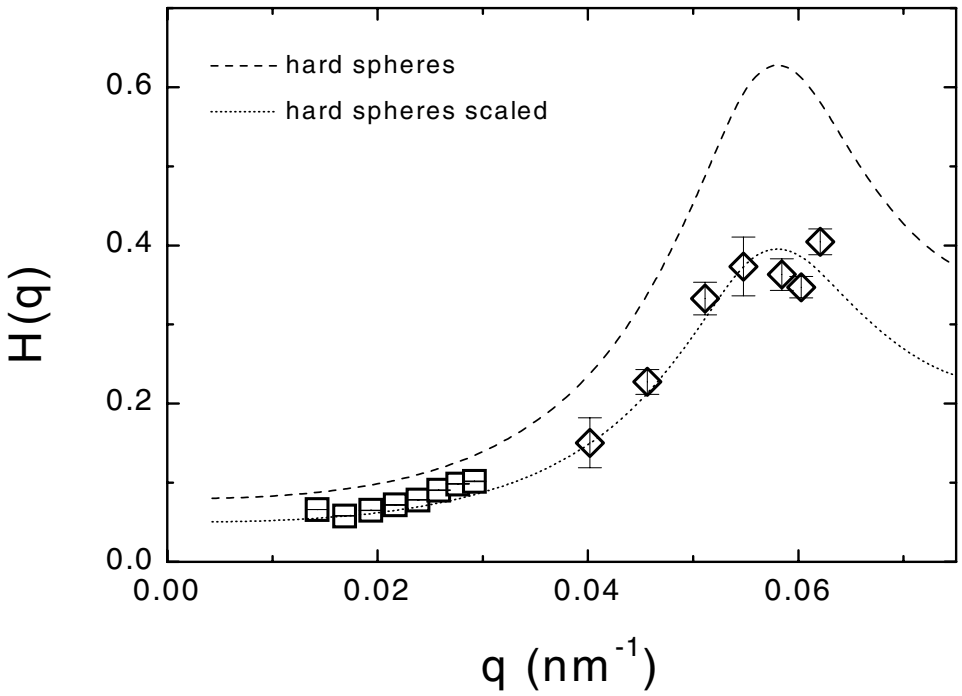

Figure 4.23: *Hydrodynamic function for silica colloids in a mixture of water and 70 wt% glycerol ($T = 22.5$ °C). The volume fraction $\phi = 0.312$. CCDLS (squares) and DXS (diamonds) results are shown. The dashed curve represents a calculation with the theory by Beenakker and Mazur, the dotted line represents the hard sphere calculation multiplied by a constant factor.*

(poor) thermal conductivity of the glass capillary and thermal radiation. The systematic difference between the x-ray data at different temperatures can be explained by assuming $T = 48$ °C instead of 52.5 °C for the higher temperature, which seems reasonable considering the setup. The static structure factors at different T are completely indistinguishable at small q. Around the peak $S(q)$ seems to be somewhat lower at the higher temperature, which might be due to reduced structural correlations as the thermal motion becomes stronger. The dashed line in fig. 4.22 represents the hard-sphere structure factor at $\phi = 0.312$. It is evident that the structure factor does not differ very strongly from the hard-sphere case for this sample. In particular, the peak position is within the experimental resolution unchanged with respect to the hard-sphere structure factor, indicating that the range

of the direct interaction is rather small. On the basis of the previous results (section 4.4.2.2), we therefore expect the dynamical behavior to be similar to that of hard spheres.

In fig. 4.23 we show the hydrodynamic function for the sample in water/70 wt% glycerol ($T = 22.5$ °C). The experimental curve is again compared to the fluctuation expansion theory of Beenakker and Mazur [47]. It is seen that the absolute value of $H(q)$ is significantly smaller than predicted by the fluctuation expansion, while the q dependence is well described. This behavior is indeed similar to the hard-sphere case at high volume fractions, as discussed in section 4.4.2.2. Since the behavior of the hydrodynamic function for this sample is entirely consistent with our previous results, we will not further elaborate on it here.

4.5 Summary

In this chapter, we have applied the novel combination of multiple-scattering free techniques described in chapter 3, cross-correlated dynamic light scattering, dynamic x-ray scattering and small-angle x-ray scattering, to charge stabilized colloidal suspensions. The techniques used allowed us to determine the hydrodynamic function $H(q)$ purely experimentally, without taking recourse to any theoretical model beforehand. For non-deionized silica suspensions, where the direct electrostatic repulsion between the colloidal particles was relatively weak and short ranged, the hydrodynamic function could be described reasonably well with an unscreened effective hydrodynamic pair interaction. In the case of deionized samples with strong interparticle structuring, we observed a flattening of the hydrodynamic function. We showed that this flattening could phenomenologically be described as hydrodynamic screening, similar to porous media. We interpreted the appearance of an effective hydrodynamic screening by a strong influence of the direct electrostatic interaction that prevents the particles from moving freely in response to the hydrodynamic field.

5

Sound propagation in suspensions of colloidal silica spheres

We measure attenuation and phase velocity of sound waves in suspensions of colloidal silica spheres by means of Brillouin spectroscopy. When the wavelength is comparable to the sphere size, the sound velocity decreases with increasing volume fraction and falls below that of the pure liquid. From the measurements of the sound velocity it is seen that the sound waves propagate predominantly in the suspending fluid. The attenuation is largely determined by scattering from the colloidal spheres. As the concentration of colloids increases, the dependence of the attenuation changes from linear to at least quadratic in volume fraction. This change is attributed to a viscous coupling of neighboring scatterers.

5.1 Introduction

In chapter 4, we have investigated the diffusion of charged colloidal silica spheres suspended in a molecular fluid. We have, in particular, been interested in the hydrodynamic interaction between the colloidal particles. One way of viewing the hydrodynamic interaction is the following: a moving colloidal sphere will excite a hydrodynamic disturbance in the suspending fluid, which diffuses through the suspension and is multiply scattered by the other particles. In fact, one can arrive at expression 4.15 for the screened hydrodynamic interaction by using multiple scattering techniques [59].

In the present chapter, we will be concerned with another aspect of the phenomenon of wave scattering in colloidal suspensions, namely the propagation of high-frequency longitudinal sound waves [92]. In theoretical treatments of colloidal dynamics, the suspending liquid is usually assumed to be incompressible. In reality, there will be thermally excited pressure waves present in the system, which contribute to the total spectrum of dynamical modes. The propagation of classical waves, such as sound and light, in inhomogeneous, strongly scattering media is a phenomenon that has received a lot of attention in the past two decades. In the case of strong multiple scattering, intriguing effects such as wave localization are expected to occur [93, 94, 95]. These exciting predictions have stimulated experimental research, largely focused on the electromagnetic case, for many years. Anderson localization of light has recently indeed been observed [96]. By contrast, to date only a few experiments on sound propagation in the strongly scattering regime have been performed [13, 97, 98, 99]. These experiments yielded astonishing results. Liu *et al.* [13], for example, studied phonon dispersion curves in colloidal suspensions and found, contrary to a pure liquid, two longitudinal propagating modes . These authors also report gaps in the dispersion relation.

5.1.1 Length scales

There are several important length scales in the system, whose ratios determine the characteristics of wave propagation. One of the parameters that play a decisive role is the ratio of the sound wavelength to the size of the scatterers, or the size parameter qa. In general, the scattering cross section depends strongly on this ratio [100]. The length scale associated with the scattering cross section is the scattering mean free path l_s. In the case of independent scattering, the scattering mean free path is given by

$$\frac{1}{l_s} = n_{coll}\sigma, \tag{5.1}$$

where n_{coll} denotes the number density of colloids and σ the scattering cross section. For a finite acoustic contrast, the scattering cross section becomes large, and thus the scattering mean free path short, if the size parameter is of order unity. Other important length scales are the average geometrical distance between the particles, $n_{coll}^{-1/3}$, and the mean distance between the

surfaces of the scatterers, l_{free}. The latter may roughly be estimated by

$$l_{free} = n_{coll}^{-1/3} - 2a, \tag{5.2}$$

at not too large volume fractions. Another essential length scale that can profoundly influence acoustic propagation is the viscous penetration depth

$$\delta = \sqrt{\frac{2\eta}{\rho_f \omega}}, \tag{5.3}$$

where η is the shear viscosity, ρ_f the mass density of the fluid, and ω the angular frequency. If transverse or vortex modes are excited in a liquid, their amplitude decays exponentially with decay length δ. For long wavelength sound propagation the viscous depth can be of great importance. In liquid saturated porous media, for instance, propagating modes can become diffusive and vice versa, depending on the ratio of the viscous length to the pore size [101, 102]. Recent acoustic band structure calculations predict comparable effects for suspensions of isolated spherical scatterers, where the interparticle separation plays a similar role as the pore size [103]. If δ is larger than the interparticle separation, scatterers are coupled by viscous forces. Despite the importance of δ, there are to date no experiments addressing possible effects of viscous coupling in the regime where the sound wavelength becomes comparable to the inhomogeneity length scales, such as the particle radius and the interparticle separation.

In this chapter, we report an investigation of acoustic wave propagation in strongly scattering media with viscously coupled scatterers. Brillouin spectroscopy is used to measure sound attenuation and velocity dispersion in suspensions of colloidal silica spheres. The viscous penetration depth is of the order of the sphere radius in the frequency range investigated. The separation between the surfaces of the spheres is varied by changing the solid volume fraction ϕ. We are thus able to perform measurements in the two regimes $\delta < l_{free}$ (no viscous coupling) and $\delta \geq l_{free}$ (viscous coupling). This is in contrast to previous studies [13, 97, 98, 99]. We find that in the absence of viscous coupling, the sound attenuation increases linearly with volume fraction, as expected. The attenuation increases at least quadratically with ϕ in the case $\delta \geq l_{free}$. However, the absolute values of the attenuation for $\delta \geq l_{free}$ are, at not too large volume fractions, smaller than expected from the low-ϕ results. The sound velocity c decreases with increasing volume fraction when the wavelength is comparable to the sphere size.

5.2 Brillouin scattering from "phononic" media

In a colloidal suspension, sound waves will be scattered from the colloidal particles if the acoustic impedance $c_s\rho_s$ of the particles is different from that of the suspending fluid, $c_f\rho_f$. Analogous to a photonic medium, were strong multiple scattering of light occurs, acoustically strongly scattering systems may be called "phononic" media. In this case, the intensity of a sound wave propagating in a specific direction, say the x-direction, will decay exponentially according to [25]

$$I(x) \propto e^{-\frac{x}{l_{ex}}}, \tag{5.4}$$

where l_{ex} is the extinction mean free path. The extinction mean free path is given by [100]

$$\frac{1}{l_{ex}} = \frac{1}{l_{abs}} + \frac{1}{l_s}, \tag{5.5}$$

where l_{abs} is the absorption length. The absorption length is related to the sound absorption coefficient (eq. 2.24):

$$\Gamma_B = \frac{c}{l_{abs}q^2}. \tag{5.6}$$

The Brillouin linewidth in the presence of scattering and absorption will be given by

$$\Delta\omega = (\Gamma_B + \Gamma_s)q^2 = \Gamma_{tot}q^2, \tag{5.7}$$

where the contribution due to scattering may be written, analogous to eq. 5.6 , as

$$\Gamma_s = \frac{c}{l_s q^2}. \tag{5.8}$$

For independent scattering, the scattering mean free path is given by eq. 5.1. Now, the number density n_{coll} is related to the volume fraction of colloids ϕ by

$$n_{coll} = \frac{3}{4\pi a^3}\phi, \tag{5.9}$$

and the scattering cross section σ may be written in terms of the geometrical cross section:

$$\sigma = Q\pi a^2. \tag{5.10}$$

Here, Q is the efficiency factor [18]. In terms of the efficiency factor and the volume fraction, the scattering mean free path (in the independent scattering limit) reads

$$\frac{a}{l_s} = \frac{3}{4} Q\phi, \tag{5.11}$$

i.e., Q is related to the ratio of the scattering mean free path to the particle radius. By combining eqs. 5.8 and 5.11 we finally arrive at

$$\Gamma_s = \frac{3}{4} c \frac{1}{a} \frac{Q}{q^2} \phi. \tag{5.12}$$

The physical quantities obtained from Brillouin spectroscopy on a colloidal suspension are the sound phase velocity c and the attenuation coefficient Γ_{tot}. We see from the above equations that in the presence of *independent* scattering, we expect the attenuation to comprise a scattering contribution that depends approximately linearly on volume fraction (Γ_s) [1].

5.3 Experimental

The most severe experimental difficulty for the experiments described here is the fact that the central Rayleigh peak in a colloidal suspension completely dominates the weak Brillouin peaks. To overcome this problem, the silica particles were suspended in an index matching mixture of ethanol and benzyl alcohol, and a triple-pass Fabry-Perot interferometer was used, as described in chapter 2. For a detailed description of the sample preparation, we refer to section 2.4. The setup to perform Brillouin spectroscopy is described in detail in section 2.3.2.

Brillouin spectra (see fig. 5.1) were obtained by averaging typically 10^3 sweeps over one free spectral range, of 1 s duration each. The Fabry-Perot interferometer was actively stabilized, using the strong Rayleigh peak as a reference. The laser power was typically 400 mW; it was checked that the spectra were independent of laser power by also measuring at lower output powers down to 100 mW. Despite the fact that the refractive index of the solvent approximately matches that of the colloidal particles, the Rayleigh peak is still about four orders of magnitude stronger in amplitude than the Brillouin peaks; this necessitates the use of a triple-pass interferometer. The

[1] This statement is true if the sound velocity c depends only weakly on ϕ.

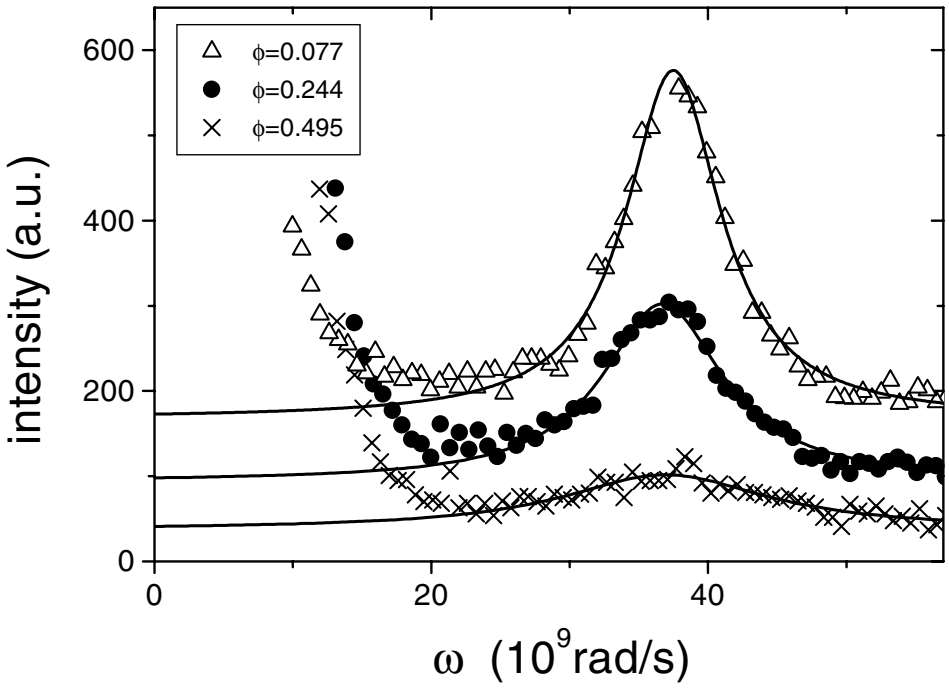

Figure 5.1: *Rayleigh-Brillouin spectra at $\theta = 90°$ for silica colloids in an optically index matching mixture of ethanol and benzyl alcohol. The volume fractions are 0.077 (triangles), 0.244 (bullets) and 0.495 (crosses). The solid lines are Lorentzian fits to the data. The spectra have been offset vertically for clarity.*

position and raw width of the peaks were obtained from Lorentzian fits to the data. To correct for the instrumental width, we assumed a triple Lorentzian for the instrumental profile, taking the width of the Rayleigh peak as input. While the instrumental profile is not represented perfectly by a triple Lorentzian curve, as seen from fig. 2.7(b), this approach has the advantage that the convolution of the expected Brillouin profile (a simple Lorentzian) with the instrumental profile can then be done analytically [26]. The true linewidth is obtained by taking an initial guess, convoluting with the instrumental function, and iterating this procedure until the width of the convoluted function equals the measured width.

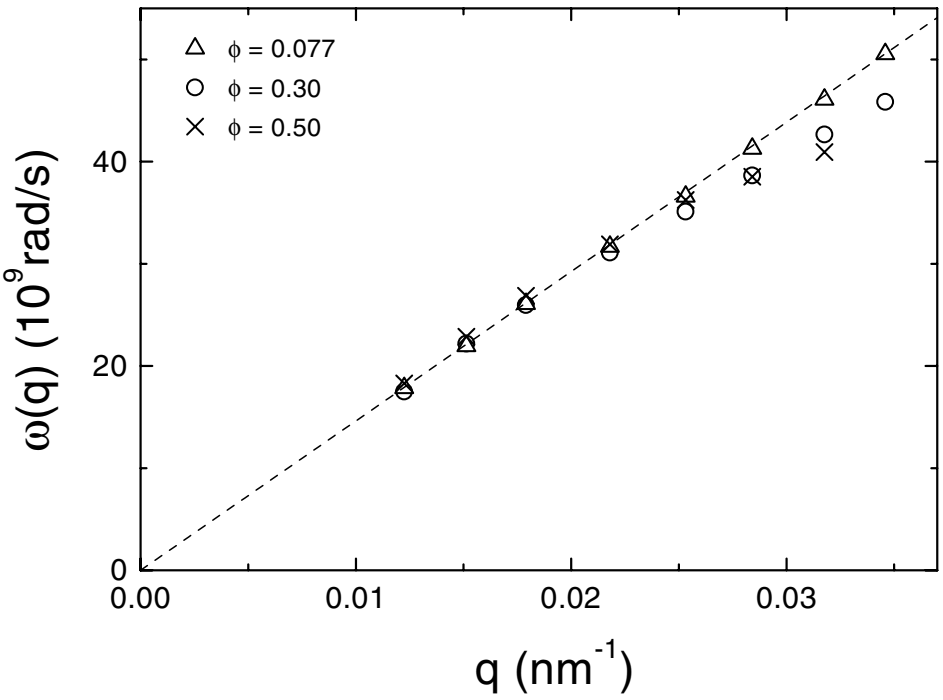

Figure 5.2: *Sound dispersion relation for suspensions of silica colloids in ethanol/benzyl alcohol. The volume fractions are 0.077 (triangles), 0.301 (circles) and 0.495 (crosses). No Brillouin spectrum could be obtained for the largest volume fraction at large wave vectors due to overdamping of the sound mode. The dotted line represents the behavior of the pure fluid.*

5.4 Results

We will now turn to the results for the sound velocity and attenuation in suspensions of colloidal silica spheres. Figure 5.1 shows typical Brillouin spectra for three representative volume fractions at an scattering angle of 90°. The spectra in fig. 5.1 are shifted in the vertical direction for clarity. At the lowest volume fraction of $\phi = 0.077$, the Brillouin peak is well pronounced and its width is small compared to the shift; this indicates the presence of a well defined longitudinal sound mode that propagates with relatively low attenuation through the system. As the volume fraction is increased, however, the amplitude of the Brillouin peak decreases and its width is found to increase

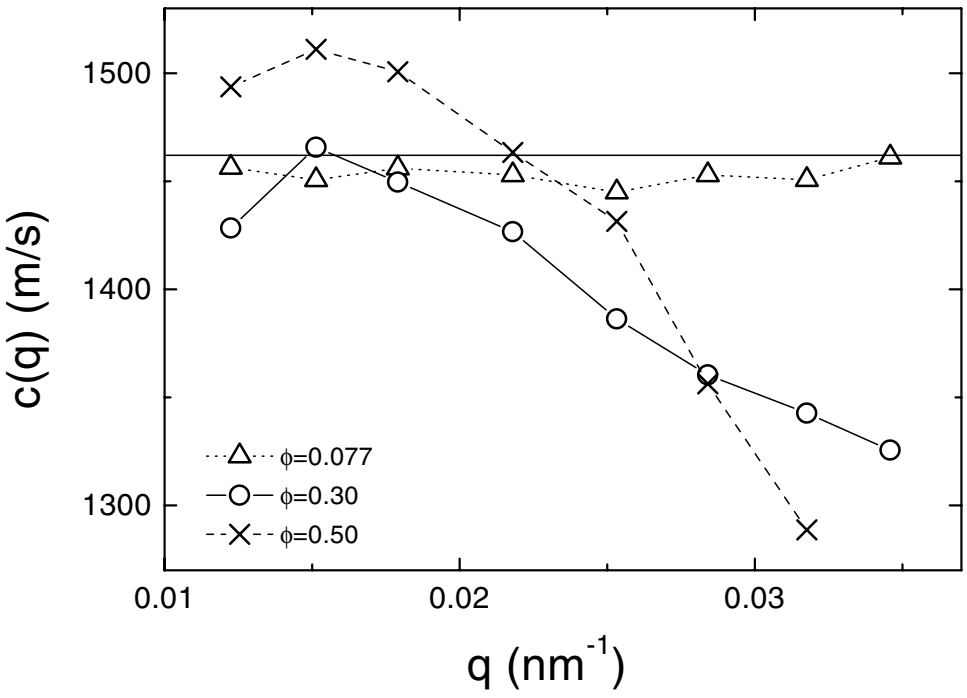

Figure 5.3: *Phase velocity $c(q) = \omega(q)/q$ for silica colloids in ethanol/benzyl alcohol. The volume fractions are 0.077 (triangles), 0.301 (circles) and 0.495 (crosses). The horizontal line represents the sound velocity of the pure fluid.*

strongly. In fact, at high volume fractions and large q no Brillouin peak is observed anymore, indicating that the sound mode has become overdamped. The peak position shifts slightly to lower frequencies with increasing volume fraction at this particular wave vector.

5.4.1 Sound velocity

The sound dispersion relation $\omega(q)$, obtained from the position of the Brillouin peaks, is displayed in fig. 5.2, again for three representative volume fractions of colloids. At the lowest volume fraction we observe a straight line, as in the pure fluid (see fig. 2.9); the dotted line in fig. 5.2 represents the dispersion relation of the pure solvent. At larger volume fractions the sound velocity becomes dependent on wave vector, thus depressing the dis-

persion relation at large q. This depression becomes continuously larger as the volume fraction is increased.

The depression of the dispersion relation is illustrated in fig. 5.3, which shows the sound phase velocity, $c(q) = \omega(q)/q$, as a function of wave vector. The volume fractions are the same as in the previous figure. It is seen that for $\phi = 0.077$, the sound velocity is independent of q and is close to that of the pure fluid; it lies however systematically below the value for the pure solvent measured before (fig. 2.9). This could be due to a difference in temperature or a slight difference in the composition of the fluid. At higher volume fractions of colloids, the sound velocity becomes clearly wave vector dependent: at small q, it increases above that of the pure fluid, while at large q, it falls below that of the solvent. An important observation is that as the volume fraction is increased, the q dependence of the sound velocity gradually becomes more pronounced, the difference to the pure fluid remaining however small. Even at the largest volume fractions, the sound velocity does not differ from that of the pure fluid by more than about 15 % at the maximum. This behavior indicates that the sound mode remains propagating predominantly in the fluid phase as the concentration of colloids increases, that is, we basically observe the fluid sound mode at all ϕ.

5.4.1.1 Discussion

Figure 5.4 shows the phase velocity at two representative wave vectors as a function of volume fraction. As already noted above, the deviations from the sound velocity of the pure fluid remain rather small at all volume fractions. To interpret this behavior, one has to realize that the sound velocity and the density of the solid phase (in this case silica) are much larger than in the fluid, i.e., the acoustic contrast is large. The velocity contrast for longitudinal waves, for instance, is $c_s/c_f = 4$, and the contrast in acoustic impedance is $\rho_s c_s/\rho_f c_f = 8.4$. As a consequence of the large acoustic contrast, the wave energy is mostly concentrated in the fluid phase. This point has been investigated by Cowan *et al.* in more detail [104]. They calculated the acoustic energy density as a function of wave vector for a liquid-coated silica sphere in an effective medium, using multiple scattering techniques. This approach is due to P. Sheng and coworkers [105]. It is found that in the region of qa investigated in our experiments, the energy density in the liquid phase is by a factor 3.5 to 5 larger than in the solid [104], that is, the sound wave propagates predominantly in the fluid phase in between the solid spheres.

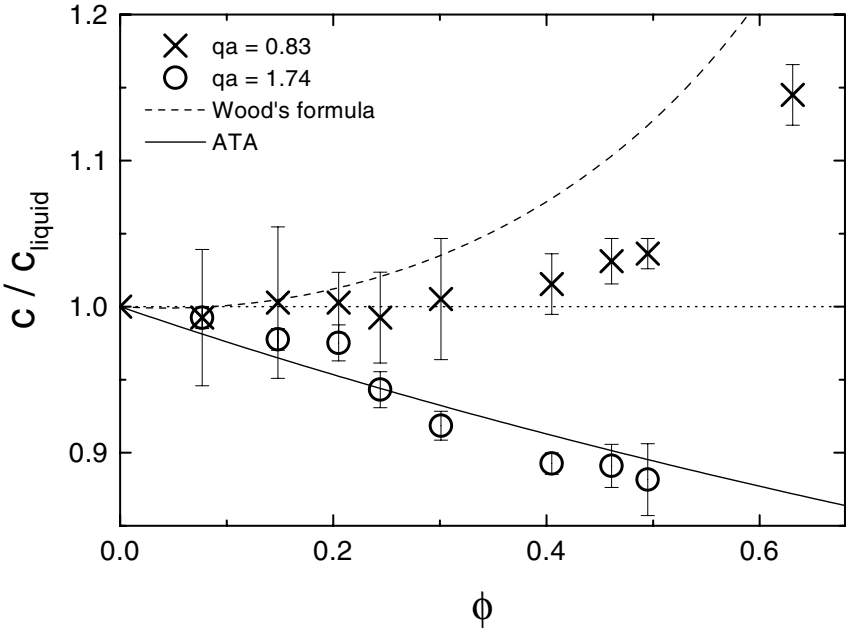

Figure 5.4: *Phase velocity of the high frequency sound mode in suspensions of silica colloids as a function of colloid volume fraction. The velocity is shown for two representative wave vectors:* $qa = 0.83$ *(crosses) and 1.74 (circles). The data are normalized by the sound velocity in the pure liquid. The dashed line represents the long wavelength limit. The solid line represents the average t-matrix approximation result for infinitely dense and stiff spheres. No spectrum could be obtained for the largest volume fraction at* $qa = 1.74$ *due to overdamping of the sound mode.*

Long wavelengths In the limit where the sound wavelength is much larger than any of the inhomogeneity length scales in the system, such as particle radius and interparticle separation, the suspension will behave as an effectively homogeneous medium with some average sound velocity. The sound velocity in this limit will thus be given by [106]

$$c^* = \sqrt{\frac{K^*}{\rho^*}}, \tag{5.13}$$

where K^* is an effective elastic modulus and ρ^* an effective mass density. In the low-frequency limit, the effective acoustic parameters are simply given

by

$$\frac{1}{K^*} = \frac{\phi}{K_s} + \frac{1-\phi}{K_f} \tag{5.14}$$

$$\rho^* = \phi\rho_s + (1-\phi)\rho_f. \tag{5.15}$$

Here, the subscripts f and s refer to the pure fluid and pure solid phases, respectively. Equation 5.13, with the effective parameters given by eq. 5.14 and 5.15, is known as Wood's formula [107]. The dashed line in fig. 5.4 represents a calculation for the long wavelength limit according to the above equations [2]. It is seen that the effective medium theory reproduces the qualitative behavior of the data at small q, but the measured sound velocity is still substantially below the one expected for the long wavelength limit, i.e., closer to the pure fluid.

Short wavelengths At smaller wavelengths (large q), the sound velocity falls slightly below that of the pure fluid. Such slow propagation velocities have also been observed in ultrasonic experiments on macroscopic glass spheres in water [97] and water/glycerol mixtures [104]. The decrease of the sound velocity with respect to the pure fluid is due to the so-called tortuosity effect: since the wave is confined mostly to the fluid in between the solid spheres, it has to follow a tortuous path through the system.

The solid line in fig. 5.4 shows the result of a particular multiple scattering theory, the average t-matrix approximation (ATA) [101, 108]. The calculation is shown for the limiting case of an infinitely dense and stiff solid phase [101, 108], that is, the solid spheres are impenetrable for the sound wave. It is seen that the sound velocity at large wave vectors, where the confinement of the wave to the fluid space in between the scatterers is more effective than at small q, corresponds well with this multiple scattering result. It should be kept in mind, however, that all the theories invoked here are effective medium theories that are strictly speaking only valid if the sound wavelength is much larger than any of the inhomogeneity length scales in the system, which is not the case here. The correspondence of our data with the effective medium results shows, however, that the physics of the problem is essentially the same.

[2] Since the sound velocity of the silica colloids is not known, we take the value for fused silica for an estimate (5968 m/s [27]).

Porous media In this section, we discuss similarities of our results to sound propagation in porous media. An effective medium theory for porous media, which includes the special case of suspensions, has for instance been devised by Biot [101, 102]. In this phenomenological hydrodynamic theory, the viscous length δ plays an important role [101]. The results of the theory that are of interest here may be summarized as follows.

In the case were both the solid frame and the fluid form interconnected phases, and the viscous penetration depth is much smaller than the pore size, the Biot theory predicts the existence of two propagating longitudinal modes. One of the two modes propagates predominantly in the fluid, its velocity being smaller than that of the pure fluid due to the tortuosity effect. If the porous frame is infinitely stiff ($K_{frame} \to \infty$), the velocity of the slow mode is given by

$$c = \frac{c_f}{\sqrt{\alpha}}, \tag{5.16}$$

where α is called the tortuosity. In the case of a suspension, where the solid phase is not interconnected, only one propagating longitudinal mode remains. However, if the solid particles are infinitely dense ($\rho_s \to \infty$) and stiff ($K_s \to \infty$), the velocity of this mode is also determined by the tortuosity effect, and eq. 5.16 applies.

The viscous length is crucial for the behavior of the "Biot slow mode": if the viscous length becomes of the order of the pore size, fluid and solid motion are strongly coupled by viscous forces. As a consequence of this viscous coupling, the slow mode becomes diffusive.

As is evident from eq. 5.16, $\sqrt{\alpha}$ may be viewed as an acoustic index of refraction. It can be shown that the problem of calculating the acoustic index of refraction of a porous medium is equivalent to determining the electrical conductivity of an insulating porous medium filled with a conducting fluid. The equivalence of the two problems arises from the close similarity of the electrodynamic and hydrodynamic equations. In the case of a dilute suspension of spherical, impenetrable spheres, one finds [109]

$$\alpha = \frac{2+\phi}{2}. \tag{5.17}$$

The Biot result for the velocity of the slow sound mode (eq. 5.16) is identical to the ATA result shown in fig. 5.4, provided one takes α to be given by eq. 5.17. We can conclude that the observed sound mode behaves analogous to the "Biot slow mode" in porous media.

5.4.1.2 Summary

Summarizing the above considerations, the following picture for interpreting our data on the phase velocity emerges. At low volume fractions, the sound mode observed in our experiments is obviously the longitudinal sound mode in the continuous fluid phase. *As the volume fraction of colloids is increased, the sound mode remains propagating predominantly in the suspending fluid.* The phase velocity is decreased with respect to the long wavelength limit, and at large q also with respect to the pure fluid, mainly as a result of the tortuosity effect. The sound mode we observe is in this respect analogous to the "Biot slow mode" in a porous medium. We note at this point the importance of the viscous penetration depth for the properties if this slow mode [101]: if the viscous penetration depth becomes of the order of the pore size the slow sound mode becomes diffusive. The comparison to the behavior of the Biot slow mode serves to illustrate that the coupling of fluid and solid motion by viscous forces can be strong and play a decisive role for acoustic wave propagation.

5.4.2 Sound attenuation

5.4.2.1 Wave vector dependence

In fig. 5.5 we show the width of the Brillouin peaks as a function of the square of the wave vector, again for three representative volume fractions. We have seen in the preceding section that the sound mode propagates through the tortuous fluid space in between the solid particles, and we therefore expect two main contributions to the attenuation: absorption by the pure fluid and scattering (see eq. 5.7).

As is evident from fig. 5.5, the width exhibits approximately a q^2 dependence. The slope of the curves increases strongly with increasing volume fraction. At the highest volume fraction, the sound mode appears to have become overdamped[3] at large wave vectors, such that no Brillouin peak could be observed anymore ; the q range is therefore more restricted at large volume fractions.

[3]By "overdamping" we mean that the imaginary part of the wave vector becomes larger than the real part. Then, the wave is spatially damped out after less than one wavelength. The frequency shift is related to the real part of q, the width to the imaginary part. At the largest q at which a Brillouin spectrum could still be measured with reasonable statistical accuracy, we have $\omega/\Delta\omega = 1.3$.

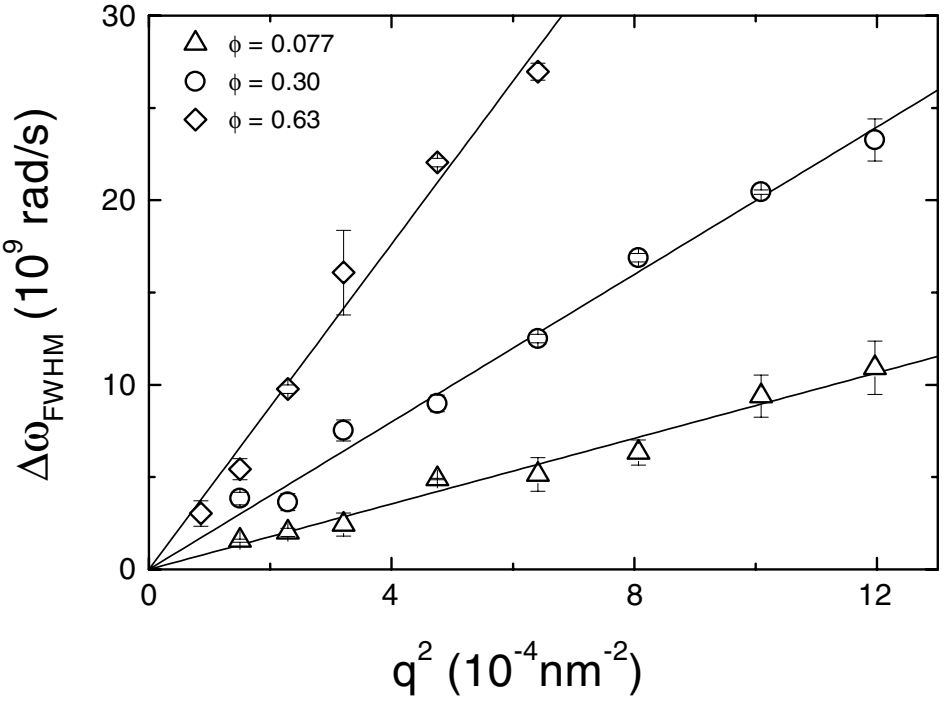

Figure 5.5: *Full width at half maximum of Brillouin peaks versus squared wave vector. Data for three volume fractions of silica colloids are shown:* $\phi = 0.077$ *(triangles), 0.301 (circles) and 0.631 (diamonds). The straight lines are fits to the data.*

The damping due to dissipation in the pure fluid is expected to have a q^2 dependence (see eq. 2.24). The q dependence of the contribution from scattering is determined by the q dependence of the scattering cross section (see eq. 5.12). The fact that we observe a q^2 dependence of the sound attenuation at all volume fractions implies that the scattering cross section has also a q^2 dependence [4].

5.4.2.2 Volume fraction dependence

We will now discuss the volume fraction dependence of the slope of the straight lines shown in fig. 5.5. The fact that the sound attenuation exhibits

[4]This is true since the sound velocity depends only weakly on wave vector.

a smooth and simple, well defined q dependence allows us to separate the volume fraction dependence from the q dependence in a simple manner. To this end, straight lines are fitted to the attenuation data according to $\Delta\omega = \Gamma_{tot}(\phi)q^2$ (solid lines in fig. 5.5). The attenuation coefficient Γ_{tot} is then independent of wave vector; it has the dimension of a diffusion coefficient, or of a kinematic viscosity.

Figure 5.6 depicts Γ_{tot} as a function of colloid volume fraction ϕ. For a proper treatment of the volume fraction dependence, we have to recall that the silica suspensions in ethanol/benzyl alcohol solidify at a volume fraction of about 35 % (see chapter 4). In fact, we observed also during the Brillouin measurements that the speckle pattern of light scattered from the samples was static for $\phi \geq 0.4$, whereas it changed in time for $\phi \leq 0.3$, in accordance with the results of chapter 4. We are thus dealing with a liquid colloidal phase at low volume fractions and a solid colloidal phase at large volume fractions, and we have to treat these two thermodynamic phases independently. The points taken in the liquid colloidal phase are represented by squares in fig. 5.6, those taken in the solid colloidal phase by triangles.

There are several important features apparent from fig. 5.6. First of all, the attenuation coefficient increases strongly with increasing volume fraction; at the largest volume fraction Γ_{tot} exceeds the value of the pure fluid by about one order of magnitude. Secondly, the points in the liquid colloidal phase lie approximately on a straight line through the point for the pure fluid, whereas the points taken in the colloidal solid do not; linearly extrapolating the data for the solid phase to $\phi = 0$ yields an unphysical, large negative value for the attenuation coefficient. Since for $\phi \to 0$ the colloidal solid should approach the pure fluid, we must conclude that the volume fraction dependence of Γ_{tot} in the solid phase includes terms at least proportional to ϕ^2. Thirdly, the absolute value of the attenuation coefficient in the solid phase is, for not too large volume fractions, smaller than expected from a linear extrapolation of the data in the fluid phase to higher volume fractions (dashed line). These are rather surprising results that will now be discussed in more detail.

5.4.2.3 Discussion

Scattering cross section Kafesaki and Economou [110] have calculated the scattering cross section for a glass sphere in water, which is comparable to the situation considered here as far as the acoustic contrast is concerned

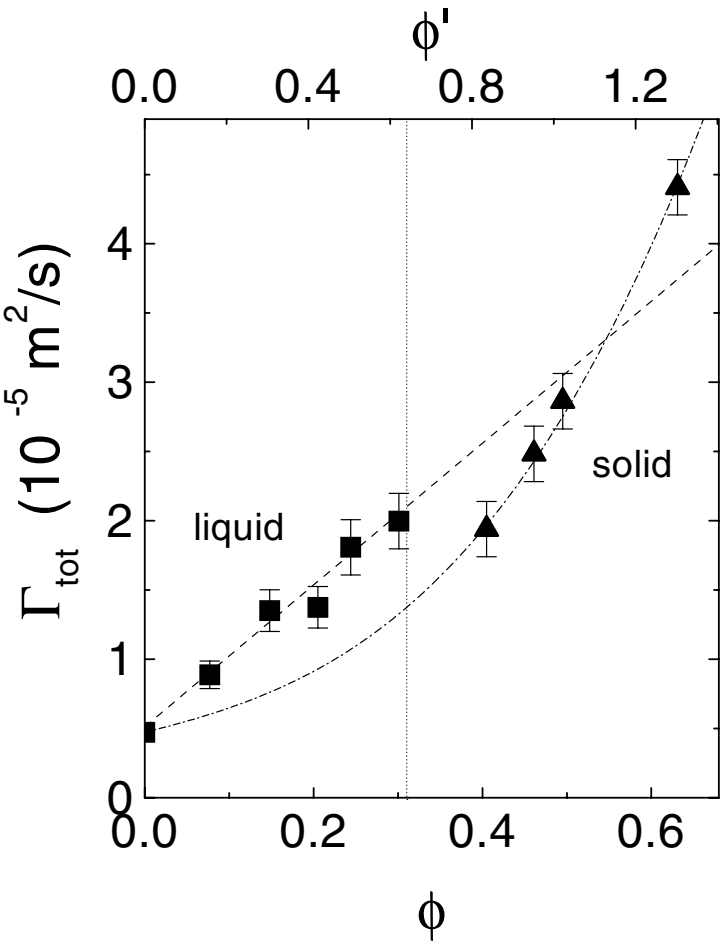

Figure 5.6: *Sound attenuation coefficient* $\Gamma_{tot} = \Delta\omega_{FWHM}/q^2$ *for the sound mode in suspensions of colloidal silica spheres versus colloid volume fraction. The dashed line is a fit to the points for* $0.077 \leq \phi \leq 0.301$*. The dash-dotted line is a guide to the eye. The suspensions are in a fluid phase at* $\phi \leq 30$ *vol%, whereas the colloid diffusion is frozen in at the larger volume fractions; the corresponding branches are treated separately. It is seen that the points at low volume fractions lie on a straight line through* $\Gamma_{tot}(\phi = 0)$*, whereas the points at high volume fractions do not.* ϕ' *is obtained from* ϕ *by replacing the particle radius* a *with* $a + \langle\delta\rangle$*. The dotted line represents* $\phi' = 0.64$*.*

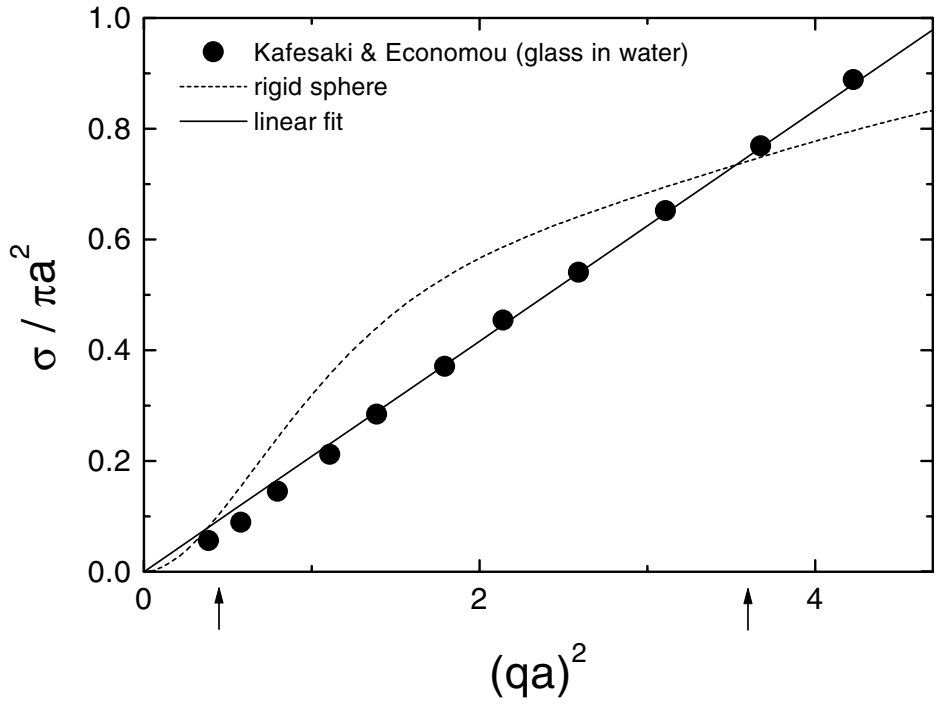

Figure 5.7: *Theoretical calculations of the scattering cross section of a glass sphere in water. The straight line is a fit to the calculated values. The dashed line represents the scattering cross section of an infinitely rigid sphere.*

[5]. In fig. 5.7 we show the result of the calculation in the relevant q range, taken from reference [110]. The arrows in the figure indicate the q range of our experiment. The values for the efficiency factor are plotted against q^2, non-dimensionalized with the particle radius. It is seen that in the q range of our experiments, the cross section shows to a very good approximation a q^2 behavior. Small deviations from this behavior become noticeable only at small wave vectors, since in the $q = 0$ limit the q^4 dependence for Rayleigh scattering is approached [25]. It should be noted that there are no strong resonances in the scattering cross section in the q range considered here. In fact, the cross section is rather smooth, without sharp peaks, over the whole q range [110]. The reason is that, as a result of the large acoustic contrast,

[5]The sound velocity in water is 1497 m/s and the density is 0.998 g/cm^3 [27], which is almost identical to the parameters of our alcohol mixture (1462 m/s and 0.938 g/cm^3).

the scattering cross section is dominated largely by that of an infinitely rigid sphere, which does not exhibit any resonances. To demonstrate this, we have also included a calculation of the scattering cross section for a very large acoustic contrast ($c_s = 2 \cdot 10^5$ m/s, $\rho_s = 200$ g/cm^3), according to the expressions given by Condat and Kirkpatrick [12] (dash-dotted line in fig. 5.7). It is evident that the efficiency factor is rather close to the rigid sphere result.

The solid line in fig. 5.7 is a linear fit to the result of Kafesaki and Economou. It is found that the theoretical efficiency factor can be represented approximately by the relation

$$Q_{th} = (0.208 \pm 0.002)(qa)^2 \tag{5.18}$$

in the q range of interest. We can conclude from these considerations that our observation of a q^2 behavior of the sound attenuation is qualitatively compatible with the assumption that the attenuation is composed of two contributions, absorption in the pure liquid and scattering from the silica spheres.

The absence of any strong resonances in the scattering cross section means that we do not expect any pronounced effects from resonant scattering in our system. This is in contrast to suspensions of PMMA particles [13]. The PMMA particles are acoustically much softer than silica particles and the cross section exhibits strong resonances in this case [105]. In PMMA suspensions, two propagating longitudinal sound modes were observed, which was attributed to a resonant coupling of neighboring spheres [105]: an excitation can "hop" from one sphere to another by "making use" of the strong resonances. The fact that we observe only one propagating longitudinal mode in silica suspensions, where strong resonances are absent, is consistent with this picture.

Volume fraction dependence in the colloidal liquid The fact that the attenuation coefficient increases linearly with volume fraction in the liquid colloidal phase can be explained by assuming that the scattering contribution to the attenuation originates from *independent* scattering. As mentioned in section 2.3, we expect the scattering mean free path to be inversely proportional to the volume fraction in this case (eq. 5.1) and, therefore, the attenuation coefficient to be proportional to ϕ (eq. 5.12) [6]. The straight line

[6] This is true since the sound velocity depends only weakly on volume fraction.

in fig. 5.6 represents a linear fit to the data in the liquid colloidal phase. From the slope of this line, we can obviously deduce an (effective) efficiency factor, according to eq. 5.12. This yields

$$Q_{eff} = \frac{\sigma_{eff}}{\pi a^2} = (0.8 \pm 0.1)(qa)^2. \tag{5.19}$$

Whereas the q dependence as well as the volume fraction dependence of the sound attenuation are qualitatively consistent with the assumption of independent scattering by isolated silica particles, as shown above, the effective efficiency factor deduced from the measurements is quantitatively in disagreement with the theoretical expectation (see eq. 5.18): it is larger than the calculated value by a factor 3.8. On first sight, this may not be surprising, since the simple relation $1/l_s = n_{coll}\sigma$ only holds in the dilute limit. However, it was shown by Cowan *et al.* [104] and by Kafesaki and Economou [110] that for glass spheres in water, the dilute limit result describes the scattering mean free path surprisingly well at all volume fractions, even up to $\phi = 0.63$. The deviations found from eq. 5.1 for these glass/water systems are only of the order of 30-50 % in the range $0.2 \leq \phi \leq 0.6$, which cannot explain the discrepancy found in our experiments.

The efficiency factor can easily be transformed into the scattering mean free path (see eq. 5.11). In fig. 5.8 we show all the important length scales in the system, at a representative size parameter of $qa = 1$, as a function of volume fraction. All length scales are given in units of the particle radius. The contribution from absorption in the pure fluid, which is associated with the absorption length, has been subtracted. The dotted line represents the dilute, non-viscous case, based on the calculations by Kafesaki and Economou (fig. 5.7). It is evident that the measured effective scattering mean free path is much smaller than expected from the dilute, non-viscous calculation.

To interpret the fact that the scattering mean free path is much smaller than expected from the simple dilute calculation, we have to realize that there is one decisive difference between the colloidal silica suspensions considered here and the glass/water systems investigated previously: the ratio of the viscous length to the particle radius is much larger. In the frequency range of our experiments we have, according to eq. 5.3, $11.2 \leq \delta \leq 18.8$ nm, which gives an average viscous length of $\langle\delta\rangle = 15$ nm [7]. We see that the

[7] To calculate the viscous length, we have taken a viscosity of $\eta = 2.96$ mPas, which we know from measurements of the colloid diffusion coefficient in the dilute limit (see chapter 4).

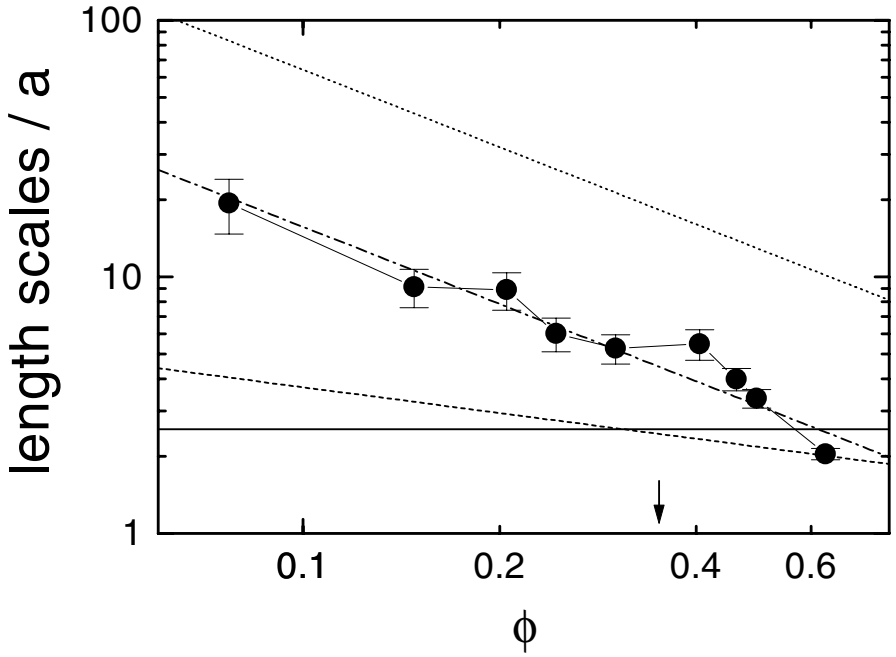

Figure 5.8: *Scattering mean free path at $qa = 1$ for silica colloids in ethanol / benzyl alcohol mixtures. The dotted line represents the calculated scattering mean free path in the dilute, non-viscous limit. The dash-dotted line is a linear fit to the data in the liquid colloidal phase. The dashed line represents a constant times the mean interparticle separation, $1.069n^{-1/3}$. The solid line represents the particle diameter renormalized by the viscous length, $d' = d + 2\langle\delta\rangle$. The arrow indicates the approximate location of the liquid-solid phase transition.*

viscous length is quite appreciable with respect to the particle radius in our system, and we can therefore expect viscous effects to play an important role. By contrast, under the conditions of the ultrasonic experiments reported on glass/water systems, the viscous length is always negligible with respect to the particle size, $\delta/a < 10^{-2}$.

We noted already in section 5.4.1.1 that the sound mode observed here is in some sense analogous to the "Biot slow wave", i.e., it propagates predominantly through the fluid space in between the solid particles and is slowed down mainly by the tortuosity effect. We also emphasized the importance of the ratio of the viscous length to the inhomogeneity length scales in the

system for this slow sound mode. The behavior of the slow mode in a porous medium clearly shows that viscous forces play a decisive role for acoustic wave propagation in a fluid-solid composite. Likewise, calculations on ordered silica suspensions indicate that the viscous length is of great importance [103]. It seems likely, therefore, that the strongly enhanced sound attenuation we observe is due to viscous effects. In fact, even for an isolated, infinitely rigid sphere in the long wavelength limit, the scattering cross section depends strongly on the ratio of the viscous length to the sphere radius, as was shown by e.g. Landau and Lifshitz [25]; if the viscous length is of the order of the sphere radius, the scattering cross section is strongly enhanced.

The fact that we observe a linear dependence of the sound attenuation coefficient Γ_{tot} on volume fraction in the liquid colloidal phase allows for a phenomenological description in terms of independent scattering by scattering "units" with an effective radius a'. Since viscous effects are important and the viscous penetration depth δ is the decisive length scale governing these effects, we attempt to renormalize the particle radius with the viscous length. Thus, we make the transformation

$$a \rightarrow a' = a + \langle \delta \rangle. \tag{5.20}$$

Doing so, we find that

$$\sigma_{eff} = (0.31 \pm 0.04)\pi a'^2 (qa')^2, \tag{5.21}$$

or equivalently

$$\frac{Q_{eff}/(qa')^2}{Q_{th}/(qa)^2} = 1.5 \pm 0.2. \tag{5.22}$$

The latter agrees within the error with the results found for glass spheres in water, when the viscous length is much smaller than the particle radius. In other words, we can map our data onto the non-viscous case by rescaling the radius in the way given in eq. 5.20. We take this observation as an additional indication that viscous effects indeed play a decisive role in the colloidal suspensions considered here.

Obviously, the phenomenological description in terms of independent scattering by spheres with an effective radius a' can only be valid as long as the renormalized spheres do not overlap, i.e., as long as the renormalized volume fraction $\phi' = \phi(a'^3/a^3)$ does not exceed the close packed limit. The scale on the upper axis in fig. 5.6 shows the renormalized volume fraction and the dotted vertical line indicates the point where $\phi' = 0.64$. It is seen

that ϕ' reaches the random close packed limit at a volume fraction $\phi = 0.31$, which is just above the largest volume fraction in the liquid colloidal state.

Volume fraction dependence in the colloidal solid In the solid colloidal phase, the attenuation coefficient Γ_{tot} does obviously not lie on a straight line through the point for the pure fluid, in contrast to the liquid colloidal phase. Instead, at least a quadratic term in the volume fraction is needed to describe the data. The dash-dotted line in fig. 5.6 is a guide to the eye to elucidate this point. The non-linear ϕ dependence is confirmed by fitting a straight line to the mean free path on a log-log scale (fig. 5.8), which yields a slope of 0.93 ± 0.11 in the liquid colloidal phase and of 2.2 ± 0.1 in the solid colloidal phase.

The fact that the renormalized volume fraction ϕ' is larger than the close packed limit in the solid colloidal phase means that the viscous length becomes comparable to the separation between the sphere surfaces, l_{free}, in the solid phase. This is illustrated in fig. 5.8. The dashed line represents $1.069 \cdot n_{coll}^{-1/3}$, where the prefactor 1.069 has been chosen such that the product equals the particle diameter at $\phi = 0.64$[8]. The solid line represents the effective, rescaled particle diameter $d' = d + 2\langle\delta\rangle$. It is seen that both length scales cross at about $\phi = 0.3$.

Estimating l_{free} according to eq. 5.2, one finds that $l_{free} = 22$ nm for $\phi = 0.301$, which is the last point in the liquid colloidal phase, but $l_{free} = 9.8$ nm for $\phi = 0.405$, the first point in the solid colloidal phase. Although eq. 5.2 is not exact and its accuracy gets worse at large volume fractions, this estimate again indicates that at high volume fractions, the average viscous length $\langle\delta\rangle = 15$ nm is of the order of the separation between the sphere surfaces. By contrast, for the lowest volume fraction of $\phi = 0.077$, $\langle\delta\rangle / l_{free} \approx 0.1$. Thus, it is clear that as the volume fraction is increased, the situation changes from $\delta < l_{free}$ to $\delta > l_{free}$, and that the transition between the two cases occurs at around the freezing transition of the colloidal suspension. We believe, therefore, that the non-linear sound attenuation in the colloidal solid phase is due to a viscous coupling of neighboring spheres. In the language of scattering, the scattering "units" do not scatter the sound wave independently anymore at high volume fractions, but are connected by viscous forces. If this argument holds true, the linear dependence of the sound attenuation coefficient,

[8]The length $n_{coll}^{-1/3}$ becomes smaller than the particle diameter for $\phi > 0.52$, the close packing volume fraction for a simple cubic symmetry, which is unphysical.

that is characteristic of independent scattering and that is observed at low volume fractions, should break down at large ϕ. These results are also in accordance with the calculations of Sprik and Wegdam [103], who investigated sound propagation in ordered structures of colloidal silica-water composites theoretically and predicted viscous coupling to play an important role.

A point that has not been addressed so far is the fact that the sound attenuation in the solid colloidal phase is at first *smaller* than expected from an extrapolation of the low-ϕ results. This surprising result is in fact consistent with our rescaling argument, since for $\phi' > 0.64$ the rescaled scattering units do overlap. As a consequence, the total geometrical cross section of neighboring (renormalized) scatterers is smaller than the sum of the individual geometrical cross sections, and thus the total cross section is expected to be smaller than the simple sum as well. A similar effect has been observed in the case of low-frequency sound propagation, in suspensions with a high acoustic contrast, in the viscous regime [111]. In the experiments described in reference [111], the frequencies were low enough for the particles to follow the oscillation of the fluid. The movement of the particles excites viscous shear waves in the fluid, leading to strong viscous losses. In a dilute system, the maximum in attenuation occurs if the viscous length is equal to the particle radius. If the volume fraction increases, however, the attenuation *decreases* at low frequencies due to the fact that the viscous length becomes larger than l_{free}, and thus the viscous shear wave cannot fully penetrate into the fluid anymore.

We see from the above arguments that a consistent phenomenological interpretation of our results in terms of viscous effects is possible. However, we have so far neglected possible influences of the differences in the detailed microstructure of the suspensions in the liquid and solid phase, or of the diffusion of the colloids (which is "frozen in" in the solid phase). The reason for this neglect is that we do not expect the particular suspensions used here to be strongly ordered in the solid phase due to the effort made to resuspend and homogenize the dispersions. We also do not expect a strong influence of colloidal diffusion, since the time scales associated with D_0 and the high-frequency sound mode considered here are separated by 6 orders of magnitude. In particular, we do not expect the qualitative form of the volume fraction dependence of the sound attenuation coefficient Γ_{tot} to be sensitive to any of these effects. We believe, therefore, that viscous effects play by far the most important role here. However, on the basis of our experiments possible consequences of the microstructure and/or a coupling of colloidal

diffusion and sound propagation cannot be quantified; it might be that these effects have an influence on the absolute value of the sound attenuation in the liquid and solid colloidal phases.

5.5 Hydrodynamic screening and wave scattering

We conclude this chapter by pointing out the analogy between the hydrodynamic screening effect considered in chapter 4 and the scattering of sound waves described here. In a homogeneous fluid, the velocity field created by a single colloidal sphere can diffuse freely into the fluid, leading to the $1/r$ dependence of the Oseen tensor. In the presence of other, fixed particles however, the velocity field scatters from these obstacles, resulting in a reduction of its range. This effect can be described by means of an effective Greens function in which the wave vector dependence $1/q^2$ for a homogeneous medium is replaced by $1/(q^2 + 1/l_{scr}^2)$. More generally, the effective Greens function reads $1/[q^2 - \Sigma(q)]$, where Σ is the self-energy. The $q = 0$ value of the self-energy gives the hydrodynamic screening length [59]. Similarly, a sound wave in a homogeneous, non-absorbing medium propagates with infinite range. In the presence of scattering, the wave intensity in a given direction will decrease exponentially with length l_s. Formally this effect is described analogous to the screening of hydrodynamic interactions. In this case, the Greens function has the dependence $1/[(\omega/c)^2 - q^2 - \Sigma]$ [94]. The self-energy is related to the scattering mean free path l_s. It is seen that the scattering mean free path plays a similar role for sound propagation as the hydrodynamic screening length does for hydrodynamic interactions. Thus, while the time- and frequency scales associated with the phenomena investigated in chapters 4 and 5 are widely separated, the underlying physics may qualitatively be interpreted in terms of a unifying picture.

5.6 Summary

In this chapter, we have presented measurements of the phase velocity and attenuation of sound waves in colloidal suspensions of silica spheres. The phase velocity was found to exhibit a continuous volume fraction dependence, remaining however close to that of the pure suspending fluid at all volume

fractions. From this behavior we concluded that the sound wave propagated predominantly in the fluid phase in between the solid particles. The attenuation coefficient showed qualitatively different behavior in the liquid colloidal phase at low volume fractions and in the solid colloidal phase at high ϕ: it increased linearly with ϕ in the liquid colloidal phase, but non-linearly in the solid phase. In addition, the attenuation in the liquid colloidal phase was found to be much larger than in comparable glass/water systems. We demonstrated that the enhancement of the sound attenuation in the liquid colloidal phase and the non-linear volume fraction dependence in the solid colloidal phase could consistently be described phenomenologically in terms of scattering by renormalized scatterers with radius $a' = a + \langle\delta\rangle$. Thus, the non-linear volume fraction dependence of the attenuation in the solid colloidal phase was attributed to a viscous coupling of neighboring scatterers.

A

HMSA closure

The structure factor is essentially the Fourier transform of the radial distribution function $g(r)$, which gives the relative conditional probability of finding a particle at a distance r apart from another particle [9]. The pair distribution function is related to the direct correlation function $c(r)$ by the Ornstein-Zernike equation [69]:

$$h(r) = c(r) + nh(r) * c(r), \tag{A.1}$$

where $h(r) = g(r) - 1$ is the total correlation function, n the particle number density, and the symbol $*$ denotes a convolution product. To calculate $g(r)$ [and therefore $S(q)$] for a given potential, eq. A.1 has to be closed by an additional relation. We will employ the so-called HMSA closure here, proposed by Zerah and Hansen [112]. This closure relation reads

$$g(r) = \exp\{-u_1(r)/k_BT\}\Big(1 + \frac{\exp\{f(r)[h(r) - c(r) - u_2(r)/k_BT]\} - 1}{f(r)}\Big), \tag{A.2}$$

where $u_1(r)$ is the repulsive part of the interparticle potential and $u_2(r)$ the attractive part. The "switching function" $f(r)$ is parameterized by

$$f(r) = 1 - \exp\{-\zeta r\}. \tag{A.3}$$

For a given potential, the parameter ζ is varied until thermodynamic consistency is achieved, that is, until the isothermal compressibility obtained from the Ornstein-Zernike equation is equal to the one obtained from the virial

equation[1]. The closure A.2 interpolates between the hypernetted-chain closure [$f(r) = 1$] and the soft mean spherical approximation [$f(r) = 0$], which are both thermodynamically inconsistent [112]. For a purely repulsive potential [$u_2(r) = 0$], the soft mean spherical approximation reduces to the well-known Percus-Yevick closure and, consequently, the HMSA scheme to the thermodynamically consistent Rogers-Young (RY) closure [9]. Since the DLVO potential is purely repulsive, the closure A.2 is identical to the RY-closure. The accuracy of the RY closure in conjunction with the DLVO potential has been demonstrated by D'Aguanno and Klein by comparison with computer simulation results [113]. The particular numerical scheme we use has successfully been applied to Lennard-Jones systems [112, 114]. We tested the scheme for the case of a DLVO potential by comparison with published computer simulation data [113, 115] and found agreement to better than 5 %.

[1] $\chi_T^{-1} = n(\partial P/\partial n)_T$, where P is the pressure.

Bibliography

[1] R. J. Hunter, *Foundations of Colloid Science* (Oxford University Press, Oxford, 1993).

[2] *Modern Aspects of Colloidal Dispersions*, edited by R. H. Ottewill and A. R. Rennie (Kluwer, Dordrecht, 1998).

[3] P. N. Pusey, in *Liquids, Freezing and the Glass Transition*, edited by J. P. Hansen, D. Levesque, and J. Zinn-Justin (Elsevier, Amsterdam, 1991).

[4] F. J. Arriagada and K. Osseo-Asare, in *The Colloid Chemistry of Silica*, edited by H. E. Bergna (Am. Chem. Soc., Washington DC, 1994).

[5] D. J. Pine, D. A. Weitz, G. Maret, P. E. Wolf, E. Herbolzheimer, and P. M. Chaikin, in *Scattering and Localization of Classical Waves in Random Media*, edited by P. Sheng (World Scientific, Singapore, 1990).

[6] G. Grübel and D. L. Abernathy, in *Coherent Electron- Beam X-Ray Sources: Techniques and Applications*, edited by A. K. Freund, H. P. Freund, and M. R. Howells, Proc. SPIE **3154**, 103 (1997).

[7] A. J. C. Ladd, Phys. Rev. Lett. **76**, 1392 (1996); P. N. Segrè, E. Herbolzheimer, and P. M. Chaikin, Phys. Rev. Lett. **79**, 2574 (1997).

[8] H. Tanaka and T. Araki, Phys. Rev. Lett. **85**, 1338 (2000).

[9] G. Nägele, Phys. Rep. **272**, 215 (1996).

[10] M. Megens, *Structure and fluorecence of photonic colloidal crystals*, Ph.D. thesis, Universiteit van Amsterdam (1999).

[11] F. J. P. Schuurmans, *Light in complex dielectrics*, Ph.D. thesis, Universiteit van Amsterdam (1999).

[12] C. A. Condat and T. R. Kirkpatrick, in *Scattering and Localization of Classical Waves in Random Media*, edited by P. Sheng (World Scientific, Singapore, 1990).

[13] J. Liu, L. Ye, D. A. Weitz, and P. Sheng, Phys. Rev. Lett. **65**, 2602 (1990); L. Ye, J. Liu, P. Sheng, and D. A. Weitz, Phys. Rev. E **48**, 2805 (1993).

[14] B. J. Berne and R. Pecora, *Dynamic Light Scattering* (Wiley, New York, 1976).

[15] D. O. Riese, W. L. Vos, G. H. Wegdam, F. J. Poelwijk, D. L. Abernathy, and G. Grübel, Phys. Rev. E **61**, 1676 (2000).

[16] D. L. Abernathy, G. Grübel, S. Brauer, I. McNulty, G. B. Stephenson, S. G. J. Mochrie, A. R. Sandy, N. Mulders, and M. Sutton, J. Synchrotron Rad. **5**, 37 (1997).

[17] G. Grübel, D. L. Abernathy, D. O. Riese, W. L. Vos, and G. H. Wegdam, J. Appl. Christallogr. **33**, 424 (2000).

[18] H. C. van de Hulst, *Light Scattering by Small Particles* (Dover, New York, 1981).

[19] M. V. Meyer, D. S. Cannell, A. E. Smart, T. W. Taylor, and P. Tin, Appl. Opt. **36**, 7551 (1997).

[20] J. A. Lock, Appl. Opt. **36**, 7559 (1997).

[21] M. Drewel, J. Ahrens, and U. Podschus, J. Opt. Soc. Am. A **7**, 206 (1990).

[22] K. Schätzel, M. Drewel, and J. Ahrens, J. Phys.: Condens. Matter **2**, SA393 (1990).

[23] A. Moussaid and P. N. Pusey, Phys. Rev. E **60**, 5670 (1999).

[24] M. Kroon, *Structure and formation of a gel of colloidal discs*, Ph.D. thesis, Universiteit van Amsterdam (1998).

[25] L. D. Landau and E. M. Lifshitz, *Fluid Mechanics* (Pergamon, London, 1959).

[26] S. M. Lindsay, S. Burgess, and I. W. Shepherd, Appl. Opt. **16**, 1404 (1977).

[27] *Handbook of Chemistry and Physics*, 73^{rd} edition, edited by D. R. Lide (CRC Press, Boca Raton, 1992).

[28] L. Bergmann, *Der Ultraschall* (S. Hirzel Verlag, Zürich, 1954).

[29] F. J. Poelwijk, *Correlatiespectroscopie aan colloidale suspensies*, Verslag Eigen Werk 3, Universiteit van Amsterdam (1998).

[30] J. Ballato, J. Dimaio, A. James, and E. Gulliver, Appl. Phys. Lett. **75**, 1497 (1999).

[31] M. Megens, C. M. van Kats, P. Bösecke, and W. L. Vos, Langmuir **13**, 6120 (1997); J. Appl. Cryst. **30**, 637 (1997).

[32] *Laser Speckle and Related Phenomena*, edited by J. C. Dainty (Springer, New York, 1989).

[33] B. Chu, *Laser Light Scattering* (Academic, San Diego, 1991).

[34] S. B. Dierker, R. Pindak, R. M. Fleming, I. K. Robinson, and L. Berman, Phys. Rev. Lett. **75**, 449 (1995).

[35] T. Thurn-Albrecht, W. Steffen, A. Patkowski, G. Meier, E. W. Fischer, G. Grübel and D. L. Abernathy, Phys. Rev. Lett. **77**, 5437 (1996).

[36] S. G. J. Mochrie, A. M. Mayers, A. R. Sandy, M. Sutton, S. Brauer, G. B. Stephenson, D. L. Abernathy, and G. Grübel, Phys. Rev. Lett. **78**, 1275 (1996).

[37] O. K. C. Tsui and S. G. J. Mochrie, Phys. Rev. E **57**, 2030 (1997).

[38] T. Thurn-Albrecht, G. Meier, P. Müller-Buschbaum, A. Patkowski, W. Steffen, G. Grübel, D. L. Abernathy, O. Diat, M. Winter, M. G. Koch, and M. T. Reetz, Phys. Rev. E **59**, 642 (1998).

[39] G. D. J. Philies, J. Chem. Phys. **74**, 260 (1981); Phys. Rev. A **24**, 1939 (1981).

[40] J. K. G. Dhont and C. G. de Kruif, J. Chem. Phys. **79**, 1658 (1983); H. J. Mos, C. Pathmamanoharan, J. K. G. Dhont, and C. G. de Kruif, J. Chem. Phys. **84**, 45 (1985).

[41] U. Nobbmann, S. W. Jones, and B. J. Ackerson, Appl. Opt. **36**, 7571 (1997).

[42] G. Grübel, A. Robert, and D. L. Abernathy, in *Slow Dynamics in Complex Systems*, 8th Tohwa University International Symposium, edited by M. Tokuyama and I. Oppenheim (1999).

[43] G. Nägele, P. Baur, Physica A **245**, 297 (1996).

[44] J. K. G. Dhont, Physica A **120**, 238 (1983); Physica A **129**, 374 (1985).

[45] P. Stepanek, J. Chem. Phys. **99**, 6384 (1993).

[46] B. Cichocki and B. U. Felderhof, J. Chem. Phys. **94**, 556 (1991); J. Chem. Phys. **94**, 563 (1991).

[47] C. W. J. Beenakker and P. Mazur, Physica A **120**, 388 (1983); Physica A **126**, 349 (1984).

[48] W. B. Russel and A. B. Glendinning, J. Chem. Phys. **74**, 948 (1981).

[49] M. Watzlawek and G. Nägele, J. Colloid Interface Sci. **214**, 170 (1999).

[50] G. K. Batchelor, J. Fluid Mech. **74**, 1 (1976).

[51] A. P. Philipse and A. Vrij, J. Chem. Phys. **88**, 6459 (1988).

[52] J. K. Phalakornkul, A. P. Gast, R. Pecora, G. Nägele, A. Ferrante, B. Mandl-Steininger, and R. Klein, Phys. Rev. E **54**, 661 (1996).

[53] W. Härtl, Ch. Beck, and R. Hempelmann, J. Chem. Phys. **110**, 7070 (1999).

[54] I. Snook, W. van Megen, R. J. A. Tough, J. Chem. Phys. **78**, 5825 (1983).

[55] D. L. Koch and E. S. G. Shaqfeh, J. Fluid Mech. **224**, 275 (1991); M. P. Brenner, Phys. Fluids **11**, 754 (1999).

[56] L. Durlofsky and J. F. Brady, Phys. Fluids **30**, 3329 (1987).

[57] K. F. Freed and S. F. Edwards, J. Chem. Phys. **61**, 3626 (1974).

[58] M. Muthukumar, J. Chem. Phys. **107**, 2619 (1997).

[59] K. F. Freed and M. Muthukumar, J. Chem. Phys. **68**, 2088 (1978); M. Muthukumar and K. F. Freed, J. Chem. Phys. **70**, 5875 (1979); M. Muthukumar, J. Chem. Phys. **77**, 959 (1982).

[60] P. J. Mucha, I. Goldhirsch, S. A. Orszag, and M. Vergassola, Phys. Rev. Lett. **83**, 3414 (1999).

[61] P. N. Segrè, O. P. Behrend, and P. N. Pusey, Phys. Rev. E **52**, 5070 (1995).

[62] A. J. C. Ladd, H. Gang, J. X. Zhu, and D. A. Weitz, Phys. Rev. E **52**, 6550 (1995).

[63] L. B. Lurio, D. Lumma, A. R. Sandy, M. A. Borthwick, P. Falus, S. G. J. Mochrie, J. F. Pelletier, M. Sutton, L. Regan, A. Malik, and G. B. Stephenson, Phys. Rev. Lett. **84**, 785 (2000).

[64] U. Genz and R. Klein, Physica A **171**, 26 (1991).

[65] G. Nägele, O. Kellerbauer, R. Krause, and R. Klein, Phys. Rev. E **47**, 2562 (1993).

[66] A. J. Banchio, G. Nägele, and J. Bergenholtz, J. Chem. Phys. **111**, 8721 (1999).

[67] M. Kroon, G. H. Wegdam, and R. Sprik, Phys. Rev. E **54**, 6541 (1996).

[68] W. L. Vos, M. Megens, C. M. van Kats, and P. Bösecke, Langmuir **13**, 6004 (1997).

[69] J. P. Hansen and I. R. McDonald, *Theory of Simple Liquids* (Academic, London, 1986).

[70] F. Grüner and W. P. Lehmann, J. Phys. A: Math. Gen. **15**, 2847 (1982).

[71] J. P. Hansen and L. Verlet, Phys. Rev. **184**, 151 (1969).

[72] P. Mazur and W. van Saarloos, Physica A **115**, 21 (1982).

[73] B. Dünweg, J. Chem. Phys. **99**, 6977 (1993).

[74] E. G. D. Cohen, R. Verberg, and I. M. de Schepper, Physica A **251**, 251 (1998).

[75] E. G. D. Cohen and I. M. de Schepper, Phys. Rev. Lett. **75**, 2252 (1995).

[76] D. A. Weitz and J. C. Ladd, Phys. Rev. Lett. **75**, 2253 (1995).

[77] C. W. J. Beenakker, Physica A **128**, 48 (1984).

[78] B. Cichocki and B. U. Felderhof, J. Chem. Phys. **89**, 3705 (1988).

[79] D. M. Jones, M. Muthukumar. and S. M. Cohen, J. Chem. Phys. **90**, 7542 (1989).

[80] H. J. H. Clercx and P. P. J. M. Schram, Physica A **174**, 293 (1991).

[81] M. Watzlawek and G. Nägele, Phys. Rev. E **56**, 1258 (1997).

[82] J. F. Brady, J. Chem. Phys. **99**, 567 (1993).

[83] W. G. Hoover and F. H. Ree, J. Chem. Phys. **49**, 3609 (1968).

[84] R. Verberg, I. M. de Schepper, and E. G. D. Cohen, Phys. Rev. E **55**, 3143 (1996).

[85] I. M. de Schepper, E. G. D. Cohen, P. N. Pusey, and H. N. W. Lekkerkerker, J. Phys.: Condens. Matter **1**, 6503 (1989); P. N. Pusey, H. N. W. Lekkerkerker, E. G. D. Cohen, and I. M. de Schepper, Physica A **164**, 12 (1990); R. Verberg, *Transport Properties in Concentrated Colloidal Suspensions*, Ph.D. thesis, Delft University of Technology (1998).

[86] For a review see J. R. Dorfman and H. van Beijeren, in *Modern Theoretical Chemistry*, Vol. 5, Part B, edited by B. J. Berne (Plenum Press, New York, 1977).

[87] M. Tokuyama and I. Oppenheim, Phy. Rev. E **50**, R16 (1994); Physica A **216**, 85 (1995).

[88] A. J. C. Ladd, J. Chem. Phys. **93**, 3484 (1990).

[89] K. Kawasaki, Ann. Phys. (NY) **61**, 1 (1970); for a review see T. Keyes, in *Modern Theoretical Chemistry*, Vol. 5, Part B, edited by B. J. Berne (Plenum Press, New York, 1977).

[90] L. Verlet and J. J. Weiss, Phys. Rev. A **5**, 939 (1971).

[91] *Landolt-Börnstein, Zahlenwerte und Funktionen*, Band II, Teil 5a (Springer Verlag, Berlin, 1969).

[92] D. O. Riese and G. H. Wegdam, Phys. Rev. Lett. **82**, 1676 (1999).

[93] *Scattering and Localization of Classical Waves in Random Media*, edited by P. Sheng (World Scientific, Singapore, 1990).

[94] P. Sheng, *Introduction to Wave Scattering, Localization, and Mesoscopic Phenomena* (Academic, San Diego, 1995).

[95] *Photonic Band Gaps and Localization*, edited by C. M. Soukoulis (Plenum, New York, 1993).

[96] D. S. Wiersma, P. Bartolini, A. Lagendijk and R. Righini, Nature **390**, 671 (1997).

[97] J. H. Page, P. Sheng, H. P. Schriemer, I. Jones, X. Jing, and D. A. Weitz, Science **271**, 634 (1996); J. H. Page, H. P. Schriemer, A. E. Bailey, and D. A. Weitz, Phys. Rev. E **52**, 3106 (1995); J. H. Page, H. P. Schriemer, I. P. Jones, P. Sheng, and D. A. Weitz, Physica A **241**, 64 (1997).

[98] H. P. Schriemer, M. L. Cowan, J. H. Page, P. Sheng, Z. Liu, and D. A. Weitz, Phys. Rev. Lett. **79**, 3166 (1997).

[99] L. Schwartz and T. J. Plona, J. Appl. Phys. **55**, 3971 (1984).

[100] A. Lagendijk and B. A. van Tiggelen, Phys. Rep. **270**, 143 (1996).

[101] For a review see D. L. Johnson, in *Proceedings of the International School of Physics "Enrico Fermi"*, Course XCIII "Frontiers in Physical Acoustics", edited by D. Setter (North Holland, Amsterdam, 1986).

[102] M. A. Biot, J. Appl. Phys. **33**, 1482 (1962).

[103] R. Sprik and G. H. Wegdam, Solid State Commun. **106**, 77 (1998).

[104] M. L. Cowan, K. Beaty, J. H. Page, Z. Liu, and P. Sheng, Phys. Rev. E **58**, 6626 (1998).

[105] X. Jing, P. Sheng, and M. Zhou, Phys. Rev. Lett. **66**, 1240 (1990); Phys. Rev. A **46**, 6513 (1992); P. Sheng, X. Jing, M. Zhou, Physica A **207**, 37 (1994).

[106] L. D. Landau and E. M. Lifshitz, *Theory of Elasticity* (Pergamon, London, 1959).

[107] A. B. Wood, *A Textbook of Sound* (G. Bell and Sons, London, 1930).

[108] P. N. Sen and D. L. Johnson, Phys. Rev. B **27**, 3133 (1983).

[109] D. L. Johnson and P. N. Sen, Phys. Rev. B **24**, 2486 (1981).

[110] M. Kafesaki and E. N. Economou, Europhys. Lett. **37**, 7 (1997). (1995).

[111] A. S. Dukhin and P. J. Goetz, Langmuir **12**, 4987 (1996).

[112] G. Zerah and J.-P. Hansen, J. Chem. Phys. **84**, 2336 (1986).

[113] B. D'Aguanno and R. Klein, J. Chem. Soc. Faraday Trans. **87**, 379 (1991).

[114] W. L. Vos, *Phase equilibria in simple systems at high pressure*, Ph.D. thesis, Universiteit van Amsterdam (1991).

[115] V. Vlachy, C. Pohar, and A. D. J. Haymet, J. Chem. Phys. **88**, 2066 (1988).

Summary

In this thesis, we investigate the interaction of hydrodynamic modes of a molecular fluid with charged colloidal particles dispersed in it. To this end, we employ light- and x-ray scattering techniques to measure the static and dynamic structure factors of dense colloidal silica suspensions.

Dynamic light scattering experiments on charged colloidal suspensions at high densities have been hampered by the problem of multiple scattering in the past. Dynamic light scattering, or photon correlation spectroscopy, measures the temporal decay of the intensity correlation function of light that is scattered by the sample. From the decay rate of the intensity correlation function, the wave-vector dependent diffusion coefficient of the colloids can be obtained. Multiple light scattering occurs if the mean distance between two scattering events, the scattering mean free path, is substantially smaller than the sample size. In the case of multiple scattering, no wave-vector dependent information can be extracted from dynamic light scattering anymore. In chapter 2, we describe two new experimental techniques with which to overcome this limitation of traditional photon correlation spectroscopy: dynamic x-ray scattering (DXS) and cross- correlated dynamic light scattering with a single laser beam (CCDLS). Since the feasibility of these techniques has been demonstrated only on dilute systems or systems with slow dynamics, it is essential to assess their potential in the case of dense interacting suspensions. In chapter 3, we first compare dynamic x-ray scattering with the well- established technique of dynamic light scattering for an optically index matched sample, where multiple light scattering is absent. We show in this way that DXS yields accurate and reliable results on systems comparable to those conventionally studied with visible light. Then, having established the reliability of DXS, we use this multiple-scattering free technique as a reference to examine the performance of CCDLS. We demonstrate that CCDLS

is capable of efficiently suppressing the detection of multiply scattered light in the case of concentrated dispersions. However, there are practical limits to CCDLS, as becomes clear from a comparison with DXS for strongly multiply scattering samples.

In chapter 4, we apply a new combination of multiple-scattering free techniques, dynamic x-ray scattering, cross-correlated dynamic light scattering, and small-angle x-ray scattering, to dense suspensions of charged colloidal silica spheres. In this way, the wave-vector dependent diffusion coefficient as well as the static structure factor of the suspensions are determined purely experimentally, without taking recourse to any theoretical model beforehand. From the diffusion coefficient and the structure factor the ensemble averaged (effective) hydrodynamic interaction between the colloids, or hydrodynamic function, is obtained. We increase the range and strength of the direct electrostatic repulsion between the silica particles for a series of samples by deionizing the suspensions. The results on the hydrodynamic interaction are compared to the so-called fluctuation expansion theory, that successfully describes the behavior of hard spheres. For non-deionized systems, where the strength and range of the direct interaction is relatively small, we find reasonable agreement with the hard-sphere theory. As the range and strength of the direct interaction increases, a flattening of the wave-vector dependence of the hydrodynamic function with respect to the fluctuation expansion theory is observed. We model this flattening by an effective hydrodynamic interaction that is partially screened, in analogy to porous media and suspensions with (on average) fixed particles. The dominant term in the screened hydrodynamic interaction falls off with the inverse of the interparticle distance cubed; by contrast, it decays with the inverse of the interparticle distance in a hard-sphere system. We conclude that the apparent hydrodynamic screening is due to the strong direct interaction that prevents the particles from moving freely in response to the hydrodynamic field.

In chapter 5, we investigate another hydrodynamic mode of colloidal silica suspensions, namely high-frequency longitudinal sound waves in the suspending fluid. The attenuation and phase velocity of these sound waves is measured by means of Brillouin spectroscopy. The sound wavelength is comparable to the radius of the silica spheres, such that strong scattering occurs. The volume fraction of colloids is varied. The sound velocity at large scattering vectors is found to fall below that of the pure fluid, whereas it is larger than the velocity of the pure solvent at small wave vectors. The difference to the velocity of the pure solvent remains however small at all volume frac-

tions up to the random close packing limit. From the measurements of the sound velocity we conclude that the sound wave propagates predominantly in the fluid space in between the solid spheres, analogous to the slow sound mode in a porous medium. This behavior is attributed to the large acoustic contrast between the colloids and the suspending fluid. The sound attenuation increases linearly with volume fraction at relatively low concentrations of colloids, where the system is in a colloidal liquid state, but non-linearly at large volume fractions, where a colloidal solid is present. The attenuation is much larger in the linear regime than in comparable systems of glass spheres in water. We attribute this enhancement of the attenuation to viscous effects, since the viscous penetration depth is comparable to the sphere radius. Consequently, the non-linear dependence of the sound attenuation on volume fraction at high concentrations, where the viscous penetration depth becomes comparable to the separation between the sphere surfaces, is interpreted in terms of a viscous coupling of neighboring scatterers.

Samenvatting

Het onderwerp van dit proefschrift is de dynamica van ladings gestabiliseerde colloidale suspensies. Een colloidale suspensie bestaat uit een moleculaire vloeistof, zoals bijvoorbeeld water, waarin grootere deeltjes zijn opgelost. De grootere deeltjes, ofwel colloiden, zijn ongeveer 1000 keer grooter dan de moleculen van de vloeistof. Voorbeelden van colloidale suspensies zijn verf, bloed, en mayonaise. In dit proefschrift bestuderen wij echter suspensies van kleine glazen bolletjes, met een straal van slechts 55 nm (1 nm is eenmiljardste meter). Glas bestaat uit silicon dioxide, ofwel silica. Als silica colloiden in een polaire vloeistof worden opgelost, ontstaat er een elektrische lading op hun oppervlak. Dit komt omdat moleculen aan het oppervlak splitsen in een positief en een negatief geladen deel (ofwel "ion"), waarvan een deel in de vloistof oplost. Het gevolg van deze processen is dat de silica colloiden elkaar afstoten. De sterkte een reikwijdte van deze afstotende kracht hangt af van de concentratie van ionen in de vloistof, omdat deze ionen de lading van de colloiden "afschermen". Afgezien van de al eerder genoemde ionen die afkomstig zijn van het oppervlak van de colloidale deeltjes, dragen ook zout ionen tot de afscherming bij. Zout is bijna altijd aanwezig in een moleculaire vloistof, tenzij de vloistof special wordt behandeld om zout te verwijderen.

Bij kamertemperatuur staan de colloiden niet stil op een vaste positie, maar bewegen als gevolg van permanente botsingen met de vloeistofmoleculen. Bij lage dichtheiden kan zo'n colloidale suspensie zelf weer als vloeistof worden beschreven, dus hij "vloeid"; dat betekent dat een bepaald colloidaal deeltje door het hele system kan bewegen. Bij hoge dichtheiden ontstaat er echter een colloidale vaste stof; in dit geval blijven de colloiden gemiddeld op een vaste positie, maar ze bewegen wel vanwege de warmtebeweging rond hun plaats. Door de beweging van de colloiden in de vloeistof onstaat er en zogenaamde hydrodynamische wisselwerking tussen de colloidale

deeltjes: een bewegend deeltje sleept als het ware vloeistof mee, waardoor een snelheidsveld in de omgeving van dit deeltje ontstaat. De beweging van de andere colloiden wordt beinvloed door het snelheidsveld.

De structuur en dynamica van colloidale suspensies kan worden bestudeerd met behulp van lichtverstrooiing. Colloidale deeltjes verstrooien licht, net als bijvoorbeeld water drupeltjes in lucht (wolken) of vet drupeltjes in water (melk), omdat hun brekingsindex in het algemeen verschilt van die van de moleculaire vloeistof eromheen. De brekingsindex van een materiaal is de verhouding van de lichtsnelheid in vacuum en de lichtsnelheid in het materiaal. Lichtgolven die op verschillende plaatsen in een colloidale suspensie zijn verstrooid interfereren. Interferentie is een karakteristieke eigenschap van golven: golven kunnen elkaar versterken (constructieve interferentie) of juist uitdoven (destructieve interferentie). Als gevolg van de interferentie vertoont de intensiteit van het van een colloidale suspensie verstrooide licht een bepaald patroon, tenminste als men een laser of een andere coherente lichtbron gebruikt. Dit interferentiepatroon wordt een specklepatroon genoemd. Een bepaald specklepatroon is karakteristiek voor een bepaalde configuratie van de colloiden. Als de configuratie in verband met de beweging van de colloiden veranderd, veranderd ook het specklepatroon. Door aan het specklepatroon tijdsopgeloste meetingen te verrichten kan men dus informatie verkrijgen over de snelheid waarmee de colloiden bewegen. De hoofdstucken 3 en 4 van dit proefschrift gaan over dit soort tijdsopgeloste meetingen aan suspensies van silica bolletjes. Bij deze meetingen wordt gekeken hoe de intensiteit op een bepaalde plaats in het specklepatroon op een bepaalde tijdstip gecorreleerd is met de intensiteit op dezelfde plaats, maar op een andere tijdstip. Dit soort meetingen noemt men “photonen correlatie spectroscopie”, of “dynamische lichtverstroiing” (DLS).

Een probleem bij de DLS methode is dat zij alleen (voor ons) nuttige informatie opleverd wanneer het licht enkelvoudig wordt verstrooid binnen de colloidale suspensie. In dat geval is het mogelijk, in combinatie met statische (tijdsonafhankelijke) lichtverstrooiings meetingen, de hydrodynamische wisselwerking tussen de colloiden te bepalen. De hydrodynamische wisselwerking vertraagd of versneld namelijk de beweging (“diffusie”) van de colloiden, en dat zie je terug in de intensiteitscorrelatie. Het doel van dit proefschrift is dit soort dynamische processen te onderzoeken voor ladings gestabiliseerde suspensies bij relatief hooge concentraties. Bij meervoudige verstrooiing wordt de relatie tussen de intensiteitscorrelatie en de dynamica van de colloiden echter verstoord, en DLS is dan geen geschikte methode meer.

Meervoudige verstrooiing betekent dat een bepaalde lichtgolf aan meer dan een deeltje binnen de suspensie wordt verstrooid. In hoofdstuk 3 worden twee nieuwe methodes onderzocht waarmee meervoudige verstrooiing kan worden onderdrukt: dynamische röntgen verstrooiing (DXS) en kruis-gecorreleerde dynamische lichtverstrooiing (CCDLS). DXS werkt op dezelfde manier als DLS, alleen met röntgen licht in plaats van zichtbaar licht. Röntgenstraling wordt veel minder verstrooid dan zichtbaar licht, waardoor meervoudige verstrooiing veel minder waarschijnlijk is. Bij CCDLS wordt de intensiteit op verschillende tijdstippen niet gecorreleerd met de intensiteit op dezelfde plaats, maar met de intensiteit op een andere (dichtbije) plaats. Men kan theoretisch laaten zien dat enkelvoudig verstrooid licht veel meer bijdraagd an zo'n kruiscorrelaat dan meervoudig verstrooid licht. In hoofdstuck 3 gebruiken wij DXS, waarvan bekend is dat meervoudige verstrooiing geen rol speeld, om te laaten zien dat CCDLS in der daad werkt. Als de meervoudige verstrooiing te belangrijk wordt ten opzichte van de enkelvoudige verstrooiing gaat CCDLS echer mis een het is dan noodzaakelijk om alleen DXS te gebruiken.

In hoofdstuk 4 gebruiken wij een combinatie van CCDLS, DXS en statische röntgen meetingen, om de hydrodynamische wisselwerking tussen silica colloiden te bepalen. De sterkte en reikwijdte van de directe, elektrostatische afstoting tussen de colloiden wordt gevarieerd door de zout concentratie in de vloeistof te veranderen. Op die manier is het mogelijk om de koppeling van de directe en hydrodynamische wisselwerking te bestuderen. De meetingen worden vergleeken met een bekende theorie die het gedrag van ongeladen colloiden goed beschrijft. De meetresultaten komen goed met deze theorie overeen voor systemen met een relatief hoge zout concentratie, waar de directe wisselwerking meer op ongeladen bollen lijkt. Bij lage zout concentratie wijken de meetresultaaten echter sterk af van de theorie. De afwijkingen wijzen op een verminderde invloed van hydrodynamische wisselwerkingen op groote afstanden, ofwel een effectieve afscherming van de hydrodynamische wisselwerking. Dit gedrag kan worden geinterpreteerd door een sterke invloed van de directe wisselwerking, welke voorkomt dat de colloiden zich vrij kunnen bewegen in het hydrodynamische snelheidsveld. Een soortgelijk effect is bekend van poreuse materialen.

In hoofdstuk 5 bestuderen wij een ander aspect van de vloeistof dynamica in colloidale suspensies, namelijk de voortplanting van geluidsgolven. Door de warmtebeweging van de moleculen is de dichtheid van een vloeistof op een bepaald tijdstip in het algemeen niet helemaal plaatsonafhankelijk, maar

er zijn berijken met een iets hogere en met een iets lagere dichtheid dan gemiddeld. De evenwichtssituatie is echter een homogene dichtheid. Het system streeft de evenwichtsituatie toe, wat betekent dat het probeerd de dichtheidsverschillen te verminderen, en dat gebeurt vaak via geluidsgolven. Een geluidsgolf is een opeenvolging van gebieden met lage en hoge dichtheid die door de vloeistof bewegt. Het is mogelijk om deze beweging met lichtverstrooiing te bestuderen, omdat de brekingsindex van een vloeistof van de dichtheid afhangt. Een geluidsgolf verstrooid dus licht, maar de verstrooiing is in dit geval veel zwakker dan de verstrooing aan de colloidale deeltjes. Ook is het zo dat de kleur, ofwel frequentie, van het van de geluidsgolven verstrooide licht verschilt van de oorspronkelijke kleur. Dit effect is bekend als "Doppler-effect" en komt door de speciale manier waarop de geluidsgolven bewegen. Door naar de frequentie-componenten van het verstrooide licht te kijken kan men informatie verkrijgen over de geluidssnelheid in de vloeistof en de geluidsdemping. Deze methode heet "Brillouin spectroscopie". In hoofdstuk 5 wordt Brillouin spectroscopie toegepast op colloidale silica suspensies. Als de golflengte van de geluidsgolven verglijkbaar is met de straal van de colloidale deeltjes, wordt de geluidssnelheid lager dan in de puure vloeistof. Dit komt omdat de gluidsgolf als het ware om de colloidale deeltjes omheen moet bewegen. De oorzaak van dit effect is het feit dat de dichtheid van de colloiden en hun geluidssnelheid veel grooter zijn dan in de vloeistof eromheen, wat lijdt tot een concentratie van de geluidsenergie in de vloeistof. Dit verschijnsel is verglijkbaar met de reflectie van een geluidsgolf aan bijvoorbeeld een wand. De oppervlaken van de colloiden vormen als het ware een heel gecompliceerde wand voor de geluidsgolven. De geluidsdemping neemt sterk toe als de concentratie van colloiden toeneemt, omdat de voortplanting van de geluidsgolven steets meer wordt verstoord. De geluidsgolven verstrooien aan de colloiden, net als licht, omdat niet alleen de optische eigenschappen van de colloiden verschillen van die van de vloeistof, maar ook de akoestische eigenschapen, zoals al eerder genoemd. Een analyse van de concentratieafhankelijkheid van de geluidsdemping laat zien dat waarschijnlijk de viscositeit van de vloeistof een heel belangrijke rol speeld.

Dankwoord

In de afgelopen vier jaar heb ik deel uitgemaakt van de Nederlandse samenleving in het algemeen en van de onderzoeksgroep van mijn promotor Ad Lagendijk in het bijzonder. Het was voor mij een heel interessante en leerzame ervaring. In dit dankwoord wil ik iedereen bedanken die in die tijd heeft bijgedragen aan dit boekje.

Allereerst dank ik mijn promotor Ad Lagendijk voor het vertrouwen dat hij mij heeft gschonken en voor de leerzame inzichten in de wetenschap - ook de sociale kant daarvan. Mijn co-promotor Gerard Wegdam ben ik bijzonder dankbaar voor alle hulp, voor alles wat ik van hem geleerd heb, voor zijn vertrouwen in mij, voor het begeleiden van mijn dagelijks werk, voor zijn enthousiasme en optimisme en zijn "inlichtingen in de Nederlandse ziel". Willem Vos dank ik voor het idee om dynamische Röntgenverstrooiing te gaan gebruiken, de HMSA-code, discussies, experimentele hulp, hulp bij de formulering van artikelen en de klimlessen. Rudolf Sprik dank ik voor discussies, praktische hulp en de mogelijkheid om bij zijn experimenten aan "photoactive yellow protein" mee te doen.

Gerard, Willem en Rudolf wil ik nog bijzonder bedanken voor de prettige samenwerking tijdens de ontelbare ESRF-runs, evenals Denis Fenistein, Frank Poelwijk, Jeroen Bongaerts en Jeroen Goedkoop. I thank Gerhard Grübel and Douglas Abernathy for the good cooperation during our measurements in Grenoble, their interest in my work and fruitful discussions.

Judith Wijnhoven wil ik bedanken voor het maken van de colloïden en de hulp met het deïoniseren daarvan.

De groep van H. B. van Linden van den Heuvell, in het bijzonder Bas Wolschrijn, bedank ik voor het lenen van veiligheidsbrillen: anders hadden wij onze lichtverstrooiings experimenten in Grenoble niet mogen doen.

Ignatz de Schepper en Rolf Verberg bedank ik voor de discussie over mijn resultaten tijdens een bezoek in Delft.

Friso van der Veen, Michel Zwanenburg en Jeroen Bongaerts bedank ik voor hun belangstelling voor mijn werk, de mogelijkheid om bij hun golfgeleider-experimenten mee te doen, en voor de prettige week in Grenoble.

De technici van zowel de mechanische als de electronische werkplaats dank ik voor hun ondersteuning, in het bijzonder Joost Overtoom, Harry Beukers, Jan Dekker en Flip de Leeuw. Flip bedank ik ook voor het "even snel" maken van een signaal splitser: anders was het promotiefeestje van Frank misgegaan! Bert Zwart en Eddy Inoeng bedank ik voor hun hulp in de glasblazerij.

Michiel Groeneveld van de afdeling scheikunde bedank ik voor het polijsten van een meetcel.

Wim Koops dank ik voor zijn technische hulp, zijn ironische kijk op de dingen en zijn humor.

Frank Poelwijk wil ik bedanken voor zijn hulp bij het voorbereiden van de eerste ESRF-run en natuurlijk voor zijn steun bij het promoten van de mensa.

Mariet Bos, Ina Zwart en Ineke Baay wil ik graag bedanken voor hulp bij administratieve zaken.

Alle groepsleden, plus de waterstof-boys, wil ik bedanken voor hulp, steun, klim- schaats- en zeillessen, en vooral voor de goede sfeer. Dank dus aan Femius, Frank I, Gijs, Jaime, Mark, Martijn, Michiel, Mischa, Rik, Arnout, Denis, Henry, Lydia, Pedro, Anouk, Frank II, Dennis, Duong, Allard, Pepijn, Peter, Bert, Matthias, Meritt, Tom.

Mijn mede-acteurs dank ik voor de afleiding en de gezelligheid.

Tenslotte wil ik graag mijn ouders bedanken voor hun steun en aanmoediging.

Dirk